ANALYSIS AND MODELING OF UNDERFILL FLOW DRIVEN BY CAPILLARY ACTION IN FLIP-CHIP PACKAGING

A thesis Submitted to the College of

Graduate Studies and Research

in Partial Fulfillment of the requirements

for the Degree of Doctor of Philosophy

in the Department of Mechanical Engineering

University of Saskatchewan

Saskatoon

By

Jianwu Wan

PERMISSION TO USE

In presenting this thesis in partial fulfillment of the requirements for a Postgraduate degree from the University of Saskatchewan, I agree that the Libraries of this University may make it freely available for inspection. I further agree that permission for copying this thesis in any manner, in whole or in part, for scholarly purposes may be granted by the professors who supervised my thesis work or, in their absence, by the Head of the Department or the Dean of the College in which my thesis work was done. It is understood that any copying or publication or use of this thesis or parts thereof for financial gain shall not be allowed without my written permission. It is also understood that due recognition shall be given to me and to the University of Saskatchewan in any scholarly use which may be made of any material in my thesis.

Requests for permission to copy or to make other use of material in this thesis in whole or part should be addressed to:

Head of the Department of Mechanical Engineering

University of Saskatchewan

Saskatoon, Saskatchewan, S7N 5A9

ABSTRACT

Flip-chip underfilling is a technology by which silica-filled epoxy resin is used to fill the micro-cavity between a silicon chip and a substrate, by dispensing the liquid encapsulant at elevated temperatures along the periphery of one or two sides of the chip and then allowing capillary action to draw the material into the gap. Since the chip, underfill material, and substrate solidify together as one unit, thermal stresses on solder joints during the temperature cycling (which are caused by a mismatch in the coefficients of thermal expansion between the silicon chip and the organic substrate) can be redistributed and transferred away from the fragile bump zone to a more strain-tolerant region. Modeling of the flow behaviour of a fluid in the underfill process is the key to this technology. One of the most important drawbacks in the existing models is inadequate treatment of non-Newtonian fluids in the underfill process in the development of both analytical models and numerical models. Another important drawback is the neglect of the presence of solder bumps in the existing analytical models.

This thesis describes a study in which a proper viscosity constitutive equation, power-law model, is employed for describing the non-Newtonian fluid behaviour in flip-chip package. Based on this constitutive equation, two analytical models with closed-form solutions for predicting the fluid filling time and fluid flow front position with respect to time were derived. One model is for a setting with two parallel plates as an approximate

to flip-chip package, while the other model is for a setting with two parallel plates within which an array of solder bumps are present. Furthermore, a numerical model using a general-purpose finite element package ANSYS was developed to predict the fluid flow map in two dimensions. The superiority of these models to the existing models (primarily those developed at Cornell University in 1997) is confirmed based on the results of the experiments conducted in this study.

This thesis also presents a finding of the notion of critical clearance in the design of a flip-chip package through a careful simulation study using the models developed. The flip-chip package design should make the clearance between solder bumps larger than the critical clearance.

ACKNOWLEDGEMENTS

I wish to express my profound gratitude to my supervisors: Professor W. J. (Chris) Zhang and Professor D. J. Bergstrom. Throughout the completion of the present study, they have given me the invaluable guidance, criticism, suggestions, and continuous encouragement. Their enthusiasm and expertise were immersed into any little progress on my research work. For all of this, I will always greatly appreciate.

I would like to extend my appreciation to other members of my Advisory Committee: Professor L. Tabil Jr., Professor D. Torvi, and Professor I. Oguocha for their examination and pieces of advice in the whole process. Also, I would like to my external examiner, Dr. C.P. Wong for his critical and constructive assessment of the thesis.

Special thanks to ASM Assembly Automated Ltd., Hong Kong, for providing both the experimental and working conditions involved in this study. In particular, the helpful discussion and support extended by Dr. Peter Liu (Technical Director of ASM, Hong Kong) is highly appreciated.

I would also like to acknowledge my colleagues and friends for their friendship, discussion and help to make the hard life a student easy.

Finally, I would like to acknowledge the partial financial support for this research by the Department of Mechanical Engineering, University of Saskatchewan, through the university graduate scholarship.

DEDICATION

This thesis is dedicated to

my dear wife Feng Yang and lovely daughter Yi-fang Wan

for

their love, encouragement, and devoted support.

TABLE OF CONTENTS

LIST OF TABLES

LIST OF FIGURES

NOMENCLATURE

B	Width of a micro-channel, m
d	Solder bump diameter, m
D	The rate of deformation tensor
D_l	External characteristic length, m
g	Gyration radius of fluid molecules, m
h	Gap height of the micro cavity, m
h^*	Dimensionless gap height
L	Length of the micro cavity, m
L^*	Dimensionless chip length
m	Consistency index, $Pa \cdot s^n$
n	Flow behaviour index, dimensionless
p	Pressure, Pa
p_{atm}	Atmosphere pressure, Pa
P_t	Solder bump pitch, m
Q	Volume flow rate, m^3/s
r	The radius of the cone, m
Re	Reynolds number, dimensionless
S	Area, m^2
t	Time, s

t_f Filling time, s

t_f^* Dimensionless filling time

T Temperature, °C, or Torque, N·m

T_g Glass transition temperature, °C

u Fluid velocity in x direction, m/s

V_n Velocity on the normal direction of the solid wall or symmetric boundary

W Clearance between two adjacent solder joints, or the width of channel, m

W^* Dimensionless clearance

$W^*_{critical}$ Dimensionless critical clearance

x_f The position of the flow-front at time t, m

y The distance of fluid to stationary surface, m

$\dot{\gamma}$ Shear rate, s^{-1}

Δp Pressure loss, Pa

Δp_σ Surface tension, Pa

Δp_j Pressure loss due to cross-section variation, Pa

η Viscosity of non-Newtonian fluid, Pa·s

η_0 Constant viscosity as shear rate becomes small, Pa·s

η_∞ Constant viscosity as shear rate gets large, Pa·s

θ Contact angle, degree

θ_0 Initial contact angle, degree

θ_e Contact angle at an equilibrium state, degree

λ Time constant for the fluid

ν Kinematic viscosity, m^2/s

μ Viscosity of Newtonian fluid, Pa·s

ξ Non-dimensional constant

σ Surface tension coefficient, N/m

σ_{SG} Solid-gas interfacial tension, N/m

σ_{SL} Solid-liquid interfacial tension, N/m

σ_{LG} Liquid-gas interfacial tension, N/m

τ Shear stress, N/m^2

τ_y Yield stress, N/m^2

η_b Bulk viscosity, Pa·s

ω Angular velocity, rad/s

LIST OF ABBREVIATIONS

CABGA	Chip Array Ball Grid Array
CFD	Computational Fluid Dynamics
CLEAR	Computational Lagrangian-Eulerian Advection Remap
CTE	Coefficient of Thermal Expansion
FCOB	Flip-chip On Board
FEM	Finite Element Method
FR4	Flame Retardant 4 (It is a fiberglass material used in the manufacture of printed circuit boards)
IC	Integrate Circuit
I/O	Input and Output
PC	Personal Computer
VFRC	Volume Fraction
VOF	Volume of Fluid

1 INTRODUCTION

This chapter aims to give an introduction to the research that was carried out and is presented in this thesis. It starts with the general picture of a promising technology, called the flip-chip technology in electronics packaging (section 1.1), highlighting its advantages and disadvantages as well as scientific issues with this technology. Solutions to these issues have resulted in the development of an important process in this technology, called the underfill process. The research presented in this thesis is focused on understanding and modeling of this process. Section 1.2 therefore presents a description of this process in detail, followed by the discussion of the current state of the art of the research on this process (section 1.3). Section 1.4 presents the research objectives as well as the scope of thesis. Finally, section 1.5 gives a brief introduction to the organization of the remainder of this thesis.

1.1 Flip-Chip Package Technology

Faster, smaller, and cheaper components have been regarded as the future trend in electronic appliances, e.g., laptop personal computers, cell phones, etc (Wong and Wong, 1999). This trend has set more stringent requirements on packaging in the

electronics industry. One of the more promising packaging methods is flip-chip technology.

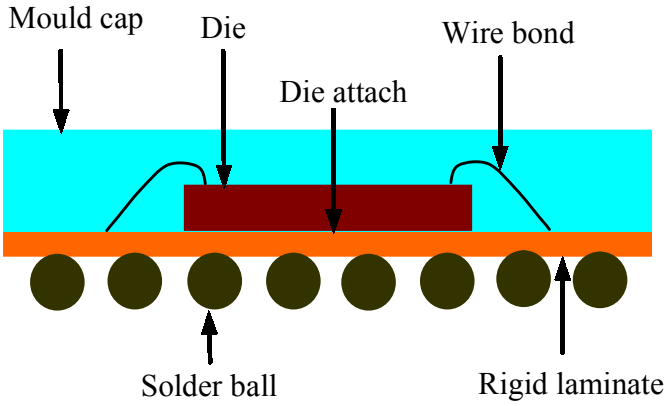

Figure 1.1 Wire bond CABGA cross section.

Until recently, the most widely used packaging technology was wire bonding technology, as shown in Figure 1.1. In wire bonding technology, the interconnection between the die and the substrate is made using a wire. The die is attached to the substrate with the active face up. A wire is bonded first to the active surface of the die, then looped and bonded to the substrate. The process is performed by high-speed machines that can bond several wires per second. But as the industry calls for smaller and higher input/output capacity integrated circuit (IC), more wires are needed. As chip size decreases and the number of input/output (I/O) increases, pads and wires are moved more closely together, making it more difficult and expensive to build the equipment needed to produce ICs. The closer together the wires at the periphery of the die, the more technical issues arise because the wires have to be bonded along the die's periphery. Additionally, when wires are bonded more closely together, electromagnetic interference caused by them becomes a significant problem. Therefore, it becomes

difficult for the wire bonding technology to further increase input/output capacity and to reduce the packaging size.

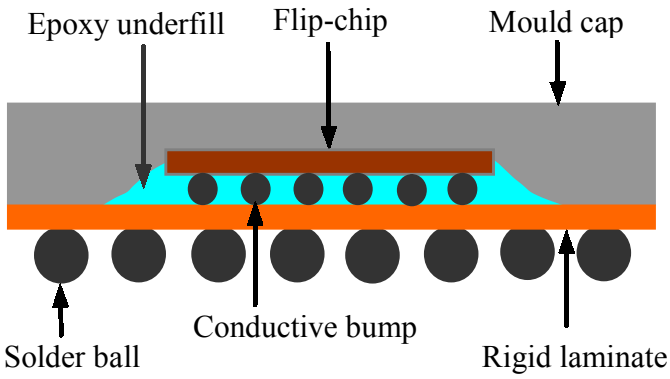

Figure 1.2 Flip-chip CABGA cross section.

The flip-chip technology solves this problem by having the die connect to the substrate via a conductive "bump" (Lau, 1995). In particular, the active face of the die is attached to the bump which is then attached to the substrate. The bumped die is therefore "flipped over" the substrate (Figure 1.2). The flip-chip package has the following advantages:

1. High input/output density capability: The entire surface of the die can be used for interconnections, not just the edges as in the wire bonding technology. Therefore, it can support a vastly larger number of interconnections with the same die size.
2. Improved electrical performance: Low capacitance and inductance due to the short interconnect from chip to substrate. As the interconnect is much shorter in length (0.1 mm bump diameter in flip-chip packaging vs. 1-5 mm wire length in wire bonding), the inductance of the signal path is greatly reduced. This is a key factor in high-speed communication and switching devices.

3. Reduced size and weight: The interconnect is "direct die attached" with no bond wires. For the pad-limited die (where the chip size is determined by the edge space required for the bond pads), the size of the die can be reduced by 1/6 to 1/10 (which reduces the cost of silicon).
4. Low cost: Bumping and flipping can be made in batches.
5. Improved thermal performance: The top surface of the chip can be used for an efficient cooling component to deal with the increasing power density required by the trend toward the devices using higher packaging densities.

Figure 1.3 illustrates the Flip-chip On Board (FCOB) assembly process, which refers to the interconnection of unpackaged integrated circuit (IC) chips directly to an organic substrate (often FR4 printed circuit board, where FR4 stands for Flame Retardant 4, a fiberglass material used in the manufacture of printed circuit boards) (O'Malley et al., 1994). The I/O bond pads on the bare IC are solder bumps with 97Pb/3Sn solder alloy. In the FCOB technology, the corresponding IC site on the organic substrate is finished with eutectic tin/lead solder (65Sn/35Pb), which allows reflow at approximately 220°C. The solder on the substrate must be flattened prior to the assembly process in order to provide a planar receiving site for the high-lead chip bump (see Figure 1.3). After the flip-chip has been aligned and placed on the substrate with the active face of the die down, the assembly is then reflow-soldered together with the substrate. When the low-temperature solder alloy on the board reflows, it flows around the high-temperature solder bumps on the IC as shown in Figure 1.4. After the reflowed low-temperature solder alloy solidifies, it forms the interconnection between the chip and the board. The

high-temperature solder (97Pb/3Sn) on the chip does not reflow. The presence of that bump also helps maintain the gap height (or stand-off) between the chip and the board.

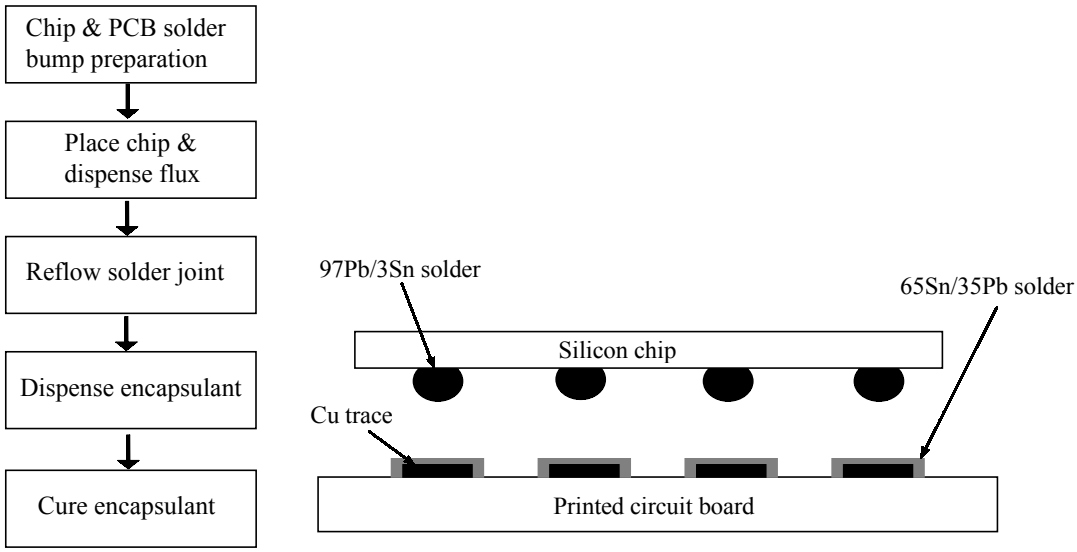

Figure 1.3 (a) FCOB assembly process; (b) Flip-chip placement operation.

Despite the many advantages of flip-chip packaging technology over other packaging technologies, it also has some problems. A major problem with flip-chip packaging technology originates from thermal stresses caused by the mismatch of the coefficients of thermal expansion between the silicon chip and the organic substrate.

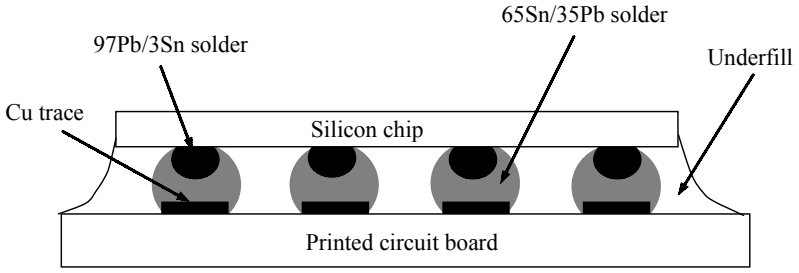

Figure 1.4 Schematic of FCOB structure.

All materials undergo some dimensional change when their temperatures change. Most materials expand when heated because increased thermal energy causes atomic or molecular distances to increase (Wong et al., 1998). The parameter used to quantify the dimensional-temperature relationship is the coefficient of thermal expansion (CTE). It is commonly expressed as the change in length per unit length per degree change in temperature. Since the thermal expansion of common materials is only a few millionths of a meter per linear meter of material when the temperature increases by a single degree, it is convenient to express this coefficient in dimensionless units, i.e., parts per million per degree (ppm/°C, or μm/m·°C). Table 1.1 lists the CTE values for some common materials.

Table 1.1 Coefficient of thermal expansion (CTE).

Material	CTE (ppm/°C)
aluminum	23.0
copper	17.5
solder	25-26
FR4	18-25
ceramic	~ 6
silicon	2.3
underfills	19-35

Two observations can be made from Table 1.1. First, silicon has a very low CTE. Second, ceramic has an expansion value that is fairly close to that of silicon, while the CTE of FR4 is nearly an order of magnitude higher. The original flip-chip used the

expensive ceramic substrates with low CTE value. Because of the similarity in thermal expansion coefficients between the chip and the ceramic substrate, thermal stresses generated during thermal excursions are not a serious problem. However, the desire for further cost reduction and increase in production volume has resulted in the use of cost-effective organic materials. The switch from the ceramic substrate to the organic substrate is clearly a non-trivial substitution because of the large difference in thermal expansion coefficients between the silicon chip and the organic substrate, which can cause significant thermal stresses on the interconnects during temperature cycling and ultimately may result in fatigue cracking and electrical failure.

Figure 1.5 shows a thermo-mechanical induced fracture of a eutectic Sn/Pb solder joint (Frear et al., 2001). This is a major reliability concern because cracks increase thermal and electrical resistance and lead to component failure. To solve this CTE mismatch problem resulting from assembling the flip-chip with a polymer-based substrate, the simplest and most cost-effective approach is to fill the gap between the chip and the organic circuit substrate with an appropriate composite to transfer the stress away from the fragile bump zone to a more strain-tolerant region (Lau and Chang, 2002; Lau and Chang, 1999; Gertach et al. 1999; Gamota and Melton, 1996; Gielser et al., 1994; Suryanarayana et al., 1993, 1991; Machuga, 1992). The underfill serves at least two purposes: (1) performance enhancement, and (2) chip/joint protection. The underfill is an encapsulant, which is coated over the active area of the die and the interconnect structure.

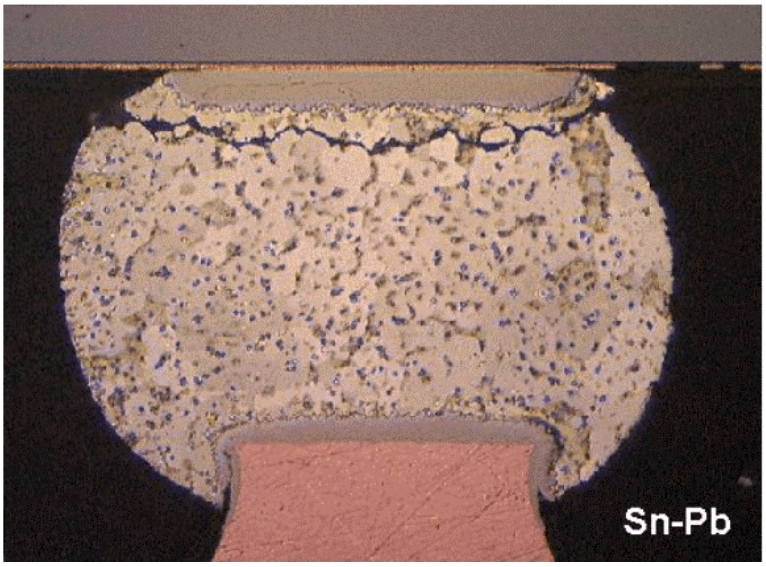

Figure 1.5 Optical micrograph of solder joint cross section on copper UBM (under bump metallurgy)/Cu pads on organic substrate after thermal cycling at 0–100ºC (Frear et al., 2001, reprinted with permission).

1.2 Flip-Chip Encapsulation Filling Method

The filling methods can be classified into three categories: conventional underfill, no-flow underfill, and injection fill.

1.2.1 Conventional Underfill

Conventional underfill technology has been developed and practiced for more than ten years. At present, more than 90 percent of the underfill processes employed in industry

are realized by dispensing liquid encapsulants at elevated temperatures along the periphery of one or two sides of the chip and allowing capillary action to draw the encapsulants into the micro-cavity (Gordon et al., 1999). During the underfill processes, the capillary action (i.e., surface tension) draws the encapsulant into the cavity between the chip and the substrate. After the filling is completed, the chip and substrate assembly is taken to an oven where the underfill is cured. Since the filling process is based on capillary action, the filling process is slow. This situation becomes significant with an increase of chip size and fine bump pitch. When the underfill material is not uniformly distributed or there are voids in the underfill region, there will be a reliability issue in the function of the packaged chip.

1.2.2 No-flow Underfill

When the underfill fluid is dispensed and cured separately from the reflow process in the conventional underfill process, the process is expensive since it generally requires separate flux dispensing, flux cleaning, solder bump reflow, and underfill cure steps. According to the semiconductor and packaging roadmap (Tadsyon, 2000), the trend for larger chip size and higher packaging densities will continue. This will inhibit the cost-effectiveness and high throughput production in the conventional underfill process. In order to meet these requirements, one possible solution is to shorten the underfill process, which calls for the development of fast-flow, fast-cure underfill materials. Another solution would be to apply the “no-flow underfill process.”

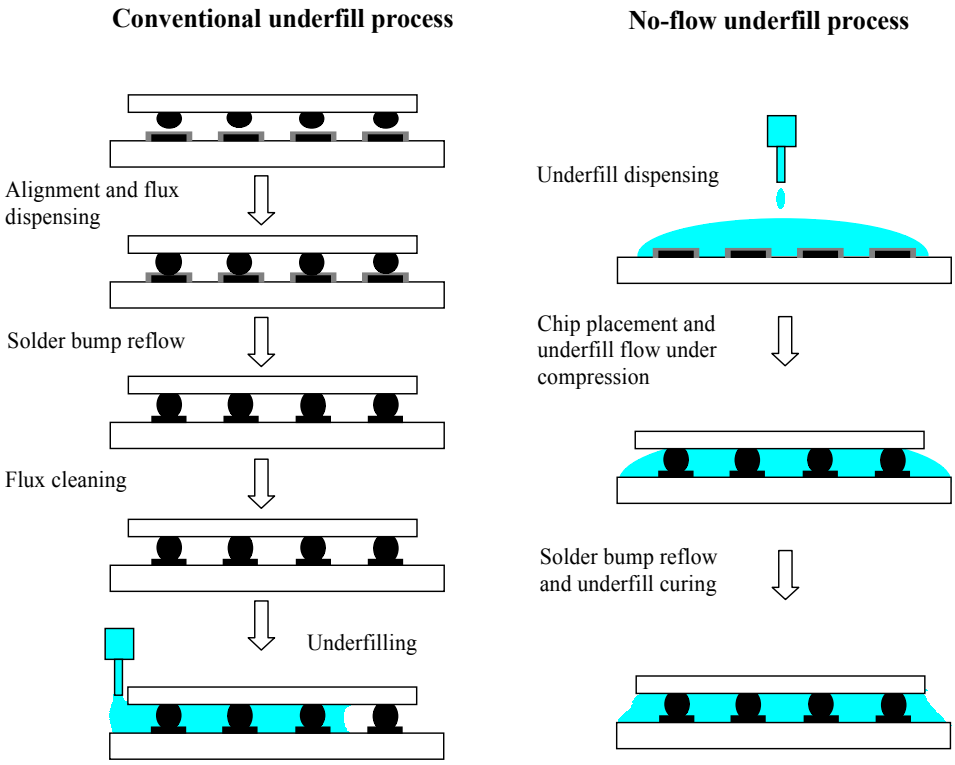

Figure 1.6 Conventional underfill processes versus no-flow underfill process.

The no-flow underfill process was reported by Wong et al. (1997, 1998) and Wong and Wong (1999). Compared with the conventional underfill process (see Figure 1.6), the no-flow underfill process has potential advantages over the conventional underfill process due to its simplicity. Because the no-flow underfill process eliminates the strict limits on the viscosity of underfill encapsulants and the package size, and simplifies the conventional underfill process by combining solder reflow and underfill cure into one step, it can improve the production efficiency. However, since the predeposited underfill cannot contain high levels of silica filler due to the interference of the filler with solder joint formation, the high CTE of the underfill results in the poor reliability of the package (Zhang and Wong, 2004). Also, the placement of the chip requires more accuracy. Since it is difficult to control during the compression flow of the underfill,

void formation is often observed in many flip-chip no-flow underfill packages (Zhang and Wong, 2004). Voids in the underfill, especially voids near the solder bumps, may cause early failure due to stress concentration, underfill delamination, and solder extrusion. Currently, no-flow underfill mainly is applied for the low input/output and small-size products for which reliability is less of a concern.

1.2.3 Injection Fill

As discussed above, the filling method based on capillary action has the disadvantage that the filling process is slow since the encapsulant is driven by surface tension at the flow-front. Therefore, the encapsulant has to be a material with a slow curing property. In order to speed up the filling process, injection filling was employed (Shen et al., 2001; Han and Wang, 1997b; Isayev and Hieber, 1980). Chai and Wu (2001), and Chai et al. (2002) introduced the use of a vacuum to increase the driving force. The vacuum method enables shorter filling times than those required by the dispensing process, but the maximum driving force is limited to the atmospheric pressure. The major concerns on the vacuum molded underfill technology are the compound flush in the air vent area and the uncompleted fill. An insufficient mold vacuum (90%-95%) will also cause the uncompleted fill issue within the chip area (Chai et al., 2002).

Han and Wang (1997b) reported a pressurized underfill encapsulation method. Their method injects the encapsulant under high pressure into the mold which surrounds and seals the chip. In this case, the flow is generated by the pressure exerted from the inlet rather than by the surface tension at the flow-front. The underfill process can be done at

either constant pressure or constant flow rate. This method can significantly reduce filling time compared to that required by the dispensing process, since the fast-curing encapsulant materials can be used and the filling can be done at room temperature. The main problem existing in the injection filling method is the unreliability caused by the air void that accompanies in the injection process and the complexity generated in the injection mold application.

It should be noted that the dispensing method still prevails in industrial practice due to its high reliability. Especially with the development of fast-flow, fast-cure underfill materials, the underfill materials used no longer exhibit the "flow-like-molasses, cures-in-half-a-day" behavior. Currently, it takes less than 40 seconds to underfill a common-size chip (6 mm x 6 mm) and a few minutes for curing in a typical industry setting. This thesis focuses on the dispensing method for flip-chip packaging technology with the goal of understanding and optimizing the process design to further improve the performance of this process based on two performance indices: (1) the fluid filling time, and (2) the fluid distribution.

1.3 Modeling the Underfill Flow Process

1.3.1 Underfill Flow Process

Figure 1.7 is a schematic diagram of underfill flow process. The encapsulant is dispensed along the periphery of one side of the chip and drawn by capillary action through the micro-cavity between the chip and the substrate. The typical gap height is

around 50 μm, and solder pitch is 200 μm to 500 μm. In order to reduce the viscosity and to make the fluid flow more quickly, the liquid encapsulant is usually heated up to 80 - 90°C.

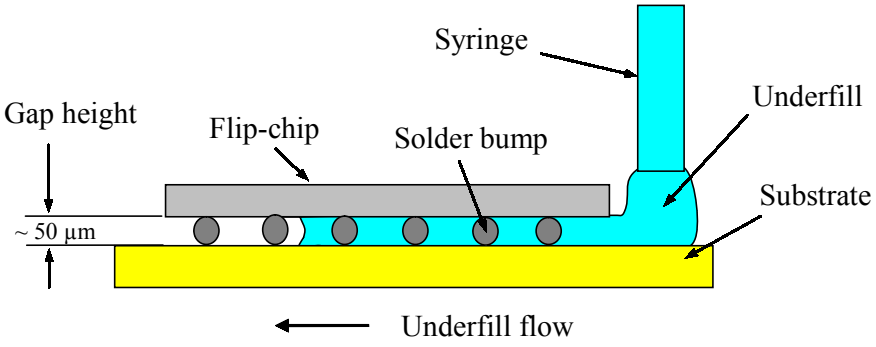

Figure 1.7 Dispensing underfill flow process.

1.3.2 Modeling Underfill Flow Process with the Washburn Model

As stated previously, the underfill flow process is evaluated by two performance indices: (1) the fluid filling time, and (2) the fluid distribution. For the purpose of simplification, the fluid distribution is also indicated by flow front, see Figure 1.8. A model describing these two indices is needed for process design optimization and control. Most studies reported in the literature (Wang, 2002; Huang, 2002; Madou, 2002; Han and Wang, 1997a; Guo et al., 1999; Pascarella and Baldin, 1998; Schwiebert and Leong, 1996) applied the Washburn model (Washburn, 1921) to the underfill flow analysis in the case of two parallel plates. In the Washburn model, it was assumed that the flow is laminar, one-dimensional, incompressible, and fully developed flow of a Newtonian fluid. This results in the following expression for the location of the flow front:

$$x_f^2 = \frac{\sigma h \cos\theta}{3\mu} t \tag{1-1}$$

where σ is the surface tension coefficient, x_f is the position of the flow-front at time t, θ is the contact angle, μ is the viscosity of the Newtonian fluid, and h is the thickness of the cavity (see Figure 1.8). From equation (1-1), the fluid filling time t_f for a cavity is

$$t_f = \frac{3\mu L^2}{\sigma h \cos\theta} \tag{1-2}$$

where L is the length of the cavity.

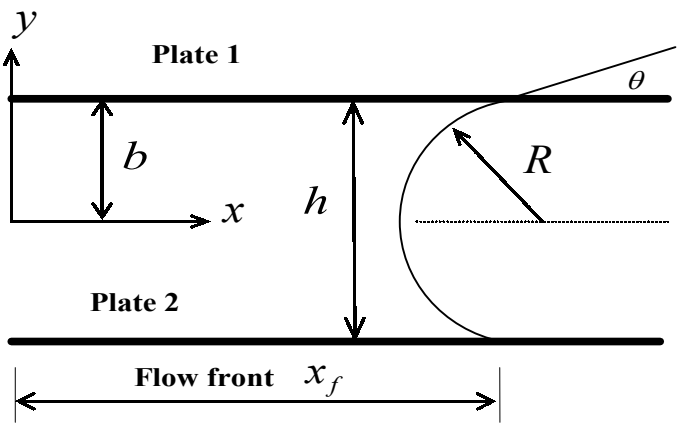

Figure 1.8 Underfill flow between two parallel plates.

Although the Washburn model has been widely used in the underfill flow analysis in flip-chip packaging, unfortunately, the filling time calculated with this model does not agree well with the observation measured in the underfill flow of a flip-chip package (Fine et at., 2000; Han and Wang, 1997a; Nguyen et al., 1999; Lehmann, 1998). One reason for this is that the Washburn model was developed for a Newtonian fluid, while underfill materials for flip-chip packaging typically exhibit non-Newtonian behavior (Nguyen et al., 1999; Han and Wang, 1997a). Another reason is that the Washburn model was originally developed for the capillary flow in a cylindrical tube and did not consider the influence of the solder bump resistance on the underfill flow in flip-chip packaging.

1.3.3 Improvement of the Washburn Model

Han and Wang (1997a) developed a method based on the Washburn model that incorporates the concept of a "dynamic contact angle." The dynamic contact angle concept proposed by Schonhorn et al. (1966) describes the change of the contact angle with time for an open-flow process of polymer melts from the initial state to an equilibrium state. Newman (1968) first employed this concept for the capillary flow in a circular tube and used the following equation to describe the contact angle:

$$\cos\theta = \cos\theta_e\left(1 - ae^{-ct}\right) \tag{1-3}$$

where a and c are coefficients, determined by

$$a = 1 - \frac{\cos\theta_0}{\cos\theta_e} \tag{1-4}$$

and

$$c = \frac{\sigma}{\eta M} \tag{1-5}$$

where θ_0 is the initial contact angle, θ_e is the contact angle at an equilibrium state, M is a constant which depends on the surface in contact with the encapsulant, and η is the viscosity of non-Newtonian fluid.

Employing equations (1-3) to (1-5) and the Washburn model, Han and Wang obtained the following equation, which is similar to an equation developed by Newman (1968) for a capillary flow in tube:

$$t_f = \frac{3\eta L^2}{\sigma h \cos\theta_e} + \frac{a}{c}\left(1 - e^{-ct_f}\right) \tag{1-6}$$

where t_f is the filling time, η is the viscosity of the non-Newtonian fluid, L is the length of a cavity, σ is the surface tension coefficient, h is the thickness of the cavity, θ_e is the contact angle at an equilibrium state. Note that equation (1-6) is a nonlinear function of filling time t_f, which would need to be solved using an iterative method. Therefore this model cannot give a closed-form solution.

Han and Wang (1997a) experimentally tested this model for a flip-chip underfill flow. The comparison between the experimental and predicted results is given in Table 1.2.

The experimental conditions for the results in Table 1.2 were: the length of the chip was 7 mm, the thickness of the cavity was 100 μm, the solder pitch was 250 μm, the clearance between adjacent solder joints was 90 μm, the initial contact angle $\theta_0 = 84.8^o$, and $M = 17.1$.

Table 1.2 Measured and calculated filing time (Han and Wang, 1997a).

Temperature (°C)	80	50	23	23	23
Fraction of volume filled (%)	0.926	0.676	0.25	0.402	0.646
Measured filling time (s)	60	180	180	600	2700
Filling time calculated with Washburn model (s) (Equation 1-2)	8.58	17.6	9.84	27.35	77.47
Filling time calculated with improved Washburn model (s) (Equation 1-6)	46.6	133.6	121.4	330.0	835.1

From Table 1.2, it is noted that the improved Washburn model is superior to the original Washburn model for predicting the underfill process in a flip-chip package. However, the predicted filling times with the improved Washburn model still did not match the experimental results. There are two possible reasons for this discrepancy. First, the viscosity in this model is for a Newtonian fluid. However, the underfill material itself is a non-Newtonian fluid. Han and Wang (1997a) attempted to resolve this contradiction by introducing the dynamic contact angle proposed by Newman (1968), which describes the change in the contact angle for an open-flow process from the initial state to an equilibrium state. Since the measurement conditions for this equation for an open-flow process are different from the capillary flow process between two parallel plates, it may not be applicable to the underfill flow in flip-chip packaging, in which the equilibrium

state should be considered for the time scales of the capillary flow process to be modeled. Second, this model was developed for the underfill flow between two parallel plates. Therefore, it did not include the effect of the solder bump on the underfill flow.

1.3.4 Numerical Modeling of Underfill Flow in Flip-Chip Packaging

Since the analytical models available could not meet the requirement for predicting the underfill flow process in flip-chip packaging, i.e., they are not able to simulate the distribution of fluid in the gap, numerical simulation methods were developed for more accurate underfill flow analysis (Han and Wang, 1997a; Nguyen et al., 1999; Gordon et al., 1999).

In the numerical study reported by Nguyen et al. (1999), the PLICE-CAD (plastic integrated circuit encapsulation computer aided design) simulation code was developed for calculating the filling time and flow front distribution in flip-chip packaging. Their simulation was based on the following condition: a 25 x 25 full array pattern of solder bumps, with a die dimensions of 6.7 mm x 6.7 mm, and an average gap height between the chip and the substrate of 56 μm. The bump diameter was 168 μm and the bump pitch was 262 μm. In their numerical simulation study, the predicted motion of the flow front was less than that of the observed front. They did not account for this discrepancy.

In the numerical simulation study reported by Han and Wang (1997a), the Hele-Shaw approximation (Chiang, 1991; Hieber and Shen, 1980; Schlichting, 1979) was used to describe the underfill flow characteristics for the encapsulant material FP4510. The

Hershel-Bulkey viscosity constitutive equation was used to describe the non-Newtonian behavior of the underfill material in their numerical simulation. It was seen from their study that the discrepancy between measured and calculated results was less than that reported by Nguyen et al. (1999). However, the flow front calculated with their model was faster than the measured value. No clear explanation was given for this discrepancy. Nguyen et al. (1999) suspected that the discrepancy might be related to the ratio of the spacing between the solder bump over the gap height.

1.4 Research Objectives

The goal of the study presented in this thesis is to advance the modeling and simulation techniques for underfill flow process in flip-chip packaging. Two streams of studies were pursued: one towards an analytical model, and the other towards a numerical model. The analytical model will be useful for process design optimization (essentially parameters variation) and real-time process control. The analytical model, however, cannot provide information regarding underfill fluid distribution; this called for the numerical model. For the development of both analytical and numerical models, the basic idea underlying this thesis study is such that the constitutive equation for the non-Newtonian fluid may be used as opposed to those existing studies that applied the constitutive equation for Newtonian fluid (Nguyen et al., 1999; Gordon et al., 1999; Han and Wang, 1997a; Schwiebert and Leong, 1996). In this case, the power-law constitutive equation for a non-Newtonian fluid was considered. Specific objectives of the thesis study are as follows:

- To develop a lumped parameter analytical model, indicated as Model I in this thesis, for the underfill process of non-Newtonian fluids in a micro-cavity between two parallel plates.

- To develop a lumped parameter analytical model, indicated as Model II in this thesis, for the underfill process of non-Newtonian fluids in the flip-chip package setting with consideration of solder bump resistance.

- To develop a numerical model and general-purpose package for simulating the underfill fluid distribution in two dimensions for the flip-chip package setting.

- To conduct experimental trials for verifying the flow characteristics of the Washburn model used in flip-chip flow analysis and for verifying analytical Model I and Model II, respectively, and the numerical model; and

- To study the design parameter variations and how they affects the performance in terms of the fluid filling time in the flip-chip package setting.

1.5 Organization of the Thesis

This thesis contains eight chapters, including the introduction. The remaining chapters are briefly described as follows.

Chapter 2 discusses the characterization of the non-Newtonian behaviour of encapsulant fluid for flip-chip packaging. Several viscosity models reported in the current literature are reviewed. The power-law model is specifically discussed. The non-Newtonian behaviour of underfill FP4530, a typical encapsulant material used in flip-chip packaging, is experimentally investigated.

Chapter 3 presents a study with the objective of understanding how a possible transient behaviour could affect the underfill flow process in the micro-cavity. Newtonian fluids are chosen for the study. Furthermore, a lumped analytical model for the fluid filling time is developed with consideration of the resistance due to the solder bump and the dynamic contact angle. This is seen as an extension of the model developed by Han and Wang (1997a) without consideration of the solder bump.

Chapter 4 presents the development of the lumped parameter analytical model, Model I, for the underfill of non-Newtonian fluids between two parallel plates, and the lumped parameter analytical model, Model II, for the underfill of non-Newtonian fluids in the flip-chip package setting (i.e., two parallel plates with solder bumps).

In chapter 5, an experimental study will be presented with the objective of testing the Washburn model, Model I, and Model II.

Chapter 6 presents a two-dimensional numerical model for the underfill flow of non-Newtonian fluid for two situations: between two parallel plates and flip-chip package. The simulation based on the model is realized with the ANSYS finite element analysis package (Version 7.0). A technique called volume of fluid (VOF) available in ANSYS is employed to track the flow front for detailed information about fluid distribution in the flip-chip micro-cavity. The numerical simulation result is also compared with the measurement result.

In Chapter 7, a design parameter sensitivity study based on Model II is presented. The package design parameters (bump pitch, solder bump diameter, and gap height) and the package process parameters (operation temperature, operation pressure) are examined for their influence on the fluid filling time. The purpose of the study is to optimize package design and the underfill process.

The conclusions drawn from the research presented in this thesis are given in Chapter 8, and a few suggestions for future research are identified.

2 RHEOLOGICAL CHARACTERIZATION OF ENCAPSULANT MATERIAL

The first step in modeling the underfill flow behavior is to understand the properties of underfill materials. These properties are closely related to the first principles upon which a model is derived. In this chapter, section 2.1 discusses the basic concept of Newtonian and non-Newtonian fluids. It is known that the underfill materials in flip-chip packaging are non-Newtonian fluids. Therefore, section 2.2 provides an overview of constitutive equations applicable to non-Newtonian fluids. Section 2.3 reviews the concept and theory corresponding to surface tension because it plays a role as a driving factor for the capillary flow in flip-chip packaging. The power-law (constitutive) model is employed in this study for the underfill fluid due to its relatively wide applicability and simplicity. The viscosity needs to be determined in order to formulate a concrete power-law model. Also, two other properties (surface tension and contact angle) need to be known in order to calculate a capillary flow. Section 2.4 gives an experimental approach to determine these properties for a typical underfill material called FP4530, which is used in this study.

2.1 Rheological Fluid Preliminaries

A conventional understanding of fluids generally classifies them into Newtonian and non-Newtonian fluids. The characteristic that distinguishes non-Newtonian fluids from Newtonian fluids is that non-Newtonian fluids have a nonlinear relationship between shear stress and shear rate (Larson, 1999; Barnes et al., 1989; Astarita and Marrucci, 1974). Newtonian fluids are the simplest of fluids, and they are characterized by the property that the velocity gradient at a position point is proportional to the shear stress at that point, thus

$$\frac{du}{dy} \propto \tau \tag{2-1}$$

where u is the velocity of the fluid, y is a position coordinate, du/dy is the velocity gradient called the shear rate, and τ is shear stress. Fluids that do not show the above behaviour are called non-Newtonian fluids (Levenspiel, 1998). Examples of substances which exhibit non-Newtonian behaviour include polymer melts, emulsions, blood, and materials possessing both viscous and elastic properties.

Non-Newtonian fluids can be divided into three broad classes of materials (Skelland, 1967):

- Viscous time-independent non-Newtonian fluids

For these kinds of non-Newtonian fluids, their shear rate and shear stress relationship can be expressed as:

$$\frac{du}{dy} = f(\tau) \tag{2-2}$$

where f is a non-linear function. Figure 2.1 shows several types of such fluids. In this figure, the shear stress of pseudoplastic liquids decreases with an increase of shear rate and the viscosity of pseudoplastic liquids have a shear thinning behaviour. The shear stress of dilatant liquids increases with an increase of shear rate and such liquids display increasing viscosity with increasing shear.

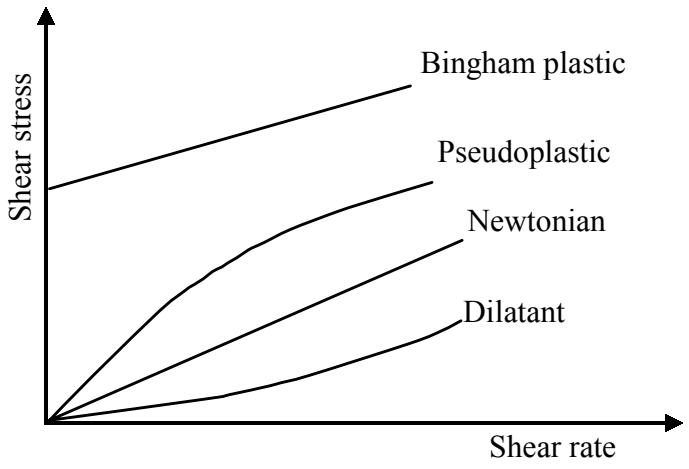

Figure 2.1 Time-independent non-Newtonian fluids.

- Viscous time-dependent but non-elastic non-Newtonian fluids

For these kinds of fluids, their present behaviour is influenced by what happened to them in the recent past. These fluids seem to have a "memory" which fades with time. The relationship between shear rate and shear stress can be expressed as:

$$\frac{du}{dy} = f(\tau, t) \tag{2-3}$$

where t is the time. Time-dependent but non-elastic non-Newtonian fluids are further classified into two groups: thixotropic fluids and rheopectic fluids, depending on whether the shear stresses decrease or increase with time at a given shear rate and constant temperature.

For thixotropic fluids, the materials exhibit a reversible decrease in shear stress with time at a given shear rate and constant temperature. If the flow curve is measured in a single experiment in which shear rate is steadily increased from zero to a maximum value and then immediately decreased steadily toward zero, a form of hysteresis loop would be obtained, as shown in Figure 2.2. The arrows in Figure 2.2 indicate the chronological progress of the experiment.

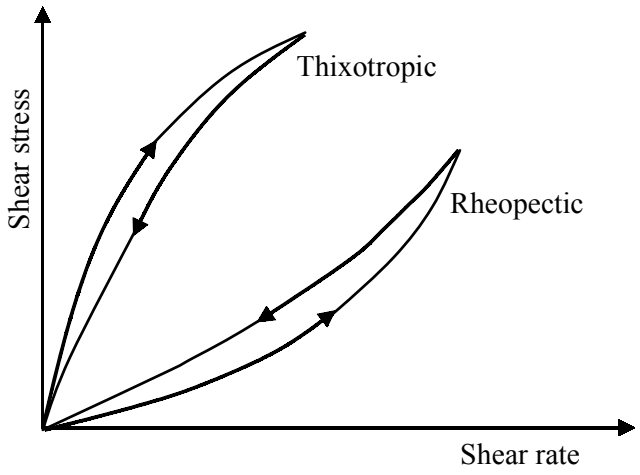

Figure 2.2 Time-dependent non-Newtonian fluids.

For rheopectic fluids, the materials exhibit a reversible increase in shear stress with time at a constant shear rate under isothermal conditions. The location of the hysteresis loop

for a given fluid is again dependent on the time history of the material, including the rate at which du/dy is increased and decreased during the experiment.

- Viscoelastic non-Newtonian fluids

Viscoelastic non-Newtonian fluids are materials which combine the elastic properties of solids with the flow behaviour of fluids. In a purely Hookean elastic solid, the stress corresponding to a given strain is independent of time, whereas for viscoelastic substances the stress will gradually dissipate. In contrast to purely viscous liquids, on the other hand, viscoelastic fluids flow when subjected to stress but part of their deformation is gradually recovered upon removal of the stress (Skelland, 1967).

When Newtonian fluids flow in a micro-cavity, their linear behavior may be changed. As well, the roughness size represents a relatively more important effect than for a macro sized channel. In this case, the fluid may need to be treated as a non-Newtonian fluid (Sabry, 2000; Eringen and Okada, 1995). In fact, for the same Reynolds number (Re), the velocity varies as

$$u = \mathrm{Re}\frac{\nu}{B} \tag{2-4}$$

where ν is the kinematic viscosity, and B is the width of a micro-channel. The wall shear stress is of the order of

$$\tau \sim \mu\frac{u}{B} \tag{2-5}$$

Hence, for the same Re, the wall shear stress is inversely proportional to the square of the cavity width. Thus, the wall shear stress for a 100 μm channel is 10^4 times that for a 1 cm channel. At such high shear stress rates, there is likely a possible influence of non-Newtonian effects. Experimental observations of liquids such as water, silicon oil, alcohol, and polymer solutions in micro channels with the characteristic dimensions of tens of micrometers have shown that the viscosity close to the channel wall is 50 to 80% higher than the bulk viscosity of the fluid. This increase is believed to be due either to the collective molecular motion effects or to the immobility of a layer of molecules in contact with the solid interface. This effect prevails in polymeric flows due to high inter-molecular interaction and the relatively large internal characteristic length, i.e., the gyration radius of a polymeric molecule.

As a result, the classic Navier-Stokes theory with dimension-independent viscosity cannot be used to explain the flow behavior, since the external characteristic length (wall thickness, channel depth) becomes comparable with the polymer gyration radius. Eringen and Okada (1995) introduced a non-local continuum theory of viscous fluids by taking the molecular orientation effects into consideration. Their theory presents the following equation for viscosity (Yao and Kim, 2002)

$$\eta = \eta_b \left[1 + \xi \left(\frac{g}{D_l} \right)^2 \right] \tag{2-6}$$

where η_b is the bulk viscosity disregarding the inner structure of the fluid, ξ is a non-dimensional constant, g is the gyration radius of fluid molecules, and D_l is an external

characteristic length. Figure 2.3 plots the micro-scale viscosity using the coefficients for polystyrene-cyclohexane solutions, $\xi = 19.5$ and $g = 26\ nm$. The label 'MV' in the figure denotes micro-scale viscosity, which increases by about 1.5% at 1 μm and by 130% at 0.1 μm over the bulk viscosity. The effect is expected to be more significant for polymeric flows with larger molecules. Furthermore, from the results shown in Figure 2.3, it can be noted that the size that has significant effect on the viscosity is within about 1 μm. Therefore, considering the gap height in flip-chip package is in the range from 30 μm to 100 μm, the size effect of the viscosity can be neglected in the flip-chip underfill flow analysis.

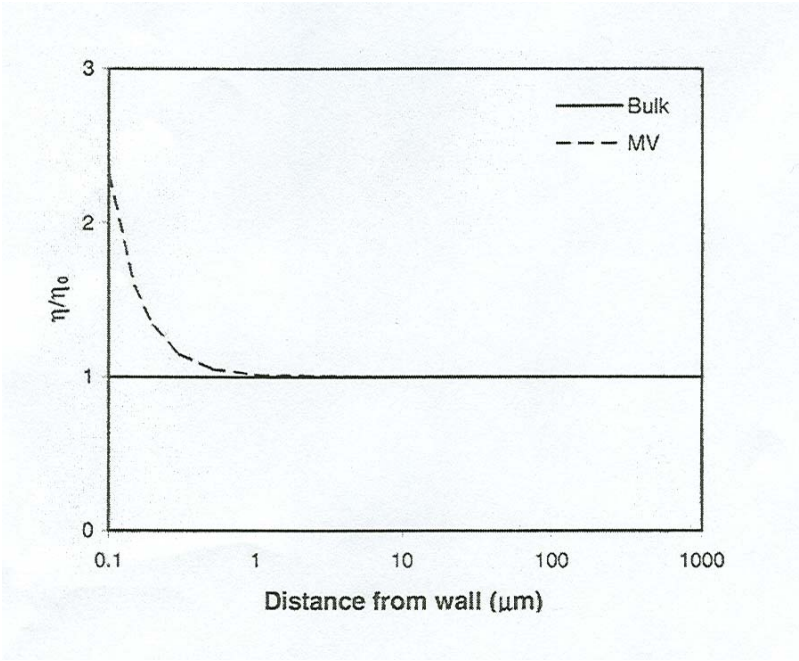

Figure 2.3 Micro-scale viscosities (MV) predicted by the Eringen and Okada equation (Yao and Kim, 2002, reprinted with permission).

Erickson et al. (2002) investigated the dimension-sensitive viscosity of a polymer containing lubricant oils in micro-channels. They found that: (1) at higher shear rates,

the effective viscosity decreased with a decrease of channel size, which may be attributed to cross-streamline polymer migration resulting in a "depleted zone" near the channel wall and an effective slip velocity, (2) at lower shear rates all solutions exhibited a sharp increase in velocity, and (3) in most cases, a cross-over point was reached below which small channels began to exhibit a larger viscosity than large channels.

Partially because of their inherent structure or because of the size effect, most of the encapsulant materials employed in flip-chip packaging are non-Newtonian or rheological fluids, such as epoxy resin and polymer melts. Therefore, a fundamental understanding of non-Newtonian fluid behaviour is required.

2.2 Constitutive Equation of Viscous Time-Independent Liquid

The constitutive equation is fundamental to non-Newtonian fluid flow. It is used to establish the momentum equation, which together with the continuity and energy equations lays down a model for flow behavior. The ratio of shear stress to shear rate is also called the apparent viscosity for rheological fluids in the literature. There are many empirical models available in the literature for the apparent viscosity (viscosity for short) (Faith, 2001; Larson, 1999; Benezech and Maingonnat 1994; Macosko, 1994; Holdersworth, 1993). Many of these models were developed for applications in the fields of liquid food products, blood, polymer melts, etc. In flip-chip packaging, most of the underfill materials show a time-independent rheological behavior characteristic of

viscous fluids. The most important characteristic in these kinds of underfill materials is the dependency of viscosity on shear rate and temperature. Some viscous constitutive relations for modeling such a time-independent rheological behavior of viscous fluids are reviewed in the following sections.

2.2.1 Power-law Model

The most widely used form of the general viscous constitutive relation is the power-law model (Macosko, 1994; Bird, 1977), which is presented as follows:

$$\tau_{ij} = m\left|II_{2D}\right|^{(n-1)/2}(2D_{ij}) \tag{2-7}$$

where D is the rate of deformation tensor, II_{2D} is the second invariant of D, and τ is the shear stress. The first subscript in equation (2-7) refers to the plane on which the components of shear stress are acting and the second indicates the direction of the component on that plane. This equation is often applied to steady simple shear flow in which the absolute value of the second invariant becomes

$$\left|II_{2D}\right| = \dot{\gamma}^2 \tag{2-8}$$

Noting that $2D_{yx} = \dfrac{\partial u}{\partial y}$ for a steady simple shear flow, the power-law model becomes

$$\tau_{yx} = m\dot{\gamma}^{(n-1)}\frac{\partial u}{\partial y} \tag{2-9}$$

which implies that the effective viscosity is given by

$$\eta = m\dot{\gamma}^{n-1} \tag{2-10}$$

where, $\dot{\gamma} = \partial u / \partial y$ is the shear rate. The power-law constitutive equation has two parameters that are determined by measurement. One parameter is $n-1$, which is the slope of $\log\eta$ versus $\log\dot{\gamma}$. The other parameter is *m*, which is called the consistency index; $\log m$ is the y-intercept of the $\log\eta$ versus $\log\dot{\gamma}$ plot. The units of the two parameters *n* and *m* can be deduced from equation (2-10) as ($Pa \cdot s^n$) and dimensionless, respectively.

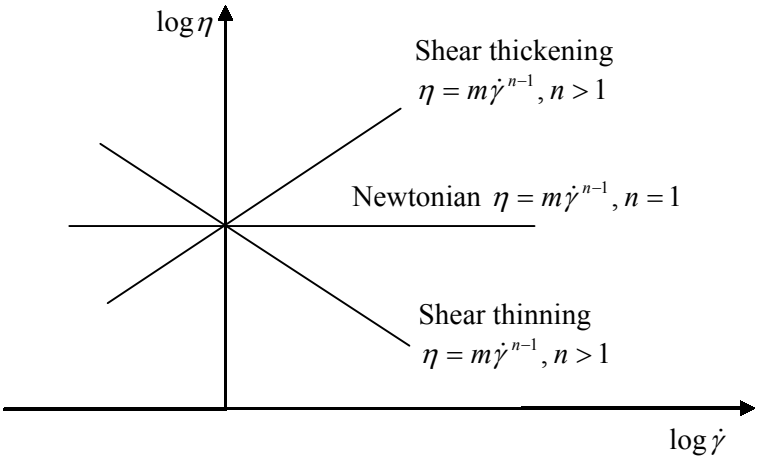

Figure 2.4 Viscosity behaviors as predicted by the power-law model.

It is noted that the power-law model reduces to the one for a Newtonian fluid when $m = \mu$ and $n = 1$; see Figure 2.4. For $n > 1$, the plot of $\log\eta$ versus $\log\dot{\gamma}$ slants upward, and the material is called dilatant or shear-thickening. For $n < 1$, the plot of $\log\eta$ versus $\log\dot{\gamma}$ slants downward, and the behavior is called shear-thinning. The

power-law model has been widely used in calculations applied to the polymer manufacturing process. This model was employed by Razban and Davies (1995) for the behavior of Elastosol M23 (supplied by Evode Ltd., Stafford, Staffordshire), which was dispensed for joint sealing or structural bonding.

2.2.2 Cross Model

To give Newtonian regions at both low and high shear rates, Cross (1965) proposed the following model (Macosko, 1994):

$$\frac{\eta - \eta_\infty}{\eta_0 - \eta_\infty} = \frac{1}{1 + (K^2 \left| II_{2D} \right|)^{(1-n)/2}} \tag{2-11}$$

where K is coefficient, η_0 the viscosity at low shear rate, η_∞ the viscosity at high shear rate. Typically $\eta_0 >> \eta_\infty$, so when $(II_{2D})^{1/2} = \dot{\gamma}$ is very small, η goes to η_0. At intermediate value of $\dot{\gamma}$, the Cross model has a power-law region

$$\eta - \eta_\infty \cong (\eta_0 - \eta_\infty) m \dot{\gamma}^{n-1} \tag{2-12}$$

where $m = K^{n-1}$. Or for $\eta >> \eta_\infty$

$$\eta \cong \eta_0 m \dot{\gamma}^{n-1} \tag{2-13}$$

At very high shear rates, the right hand side of equation (2-12) becomes very small, and η goes to the high shear rate Newtonian limit, η_∞. Figure 2.5 shows a comparison between the Cross model and the power-law model (Macosko, 1994).

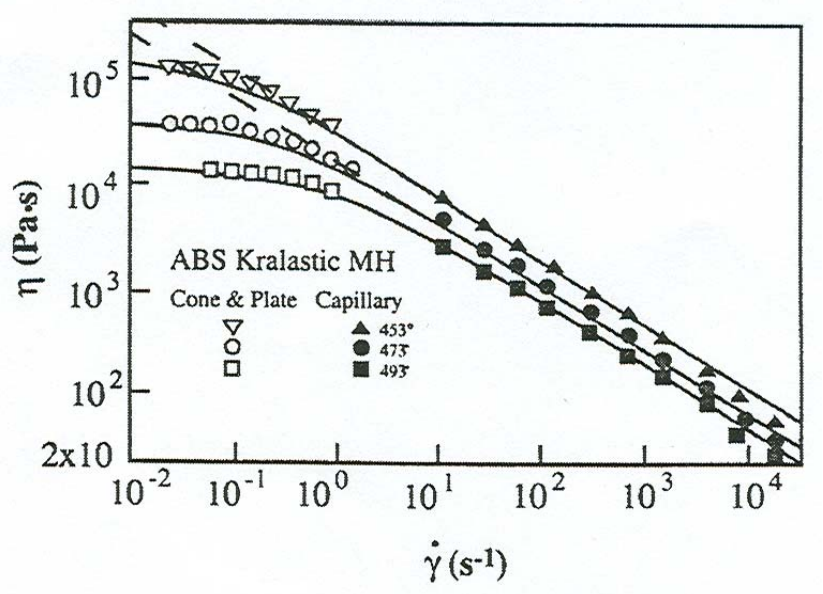

Figure 2.5 Plot of viscosity versus shear rate for an ABS polymer melt at three temperatures: dashed lines, power-law fit; solid line represents Cross model (Macosko, 1994, reprinted with permission).

2.2.3 Carreau-Yasuda Model

Yasuda et al. proposed a model as follows (Morrison, 2001)

$$\frac{\eta-\eta_\infty}{\eta_0-\eta_\infty}=\frac{1}{(1+\lambda^a|II_{2D}|)^{(1-n)/a}} \tag{2-14}$$

The Carreau-Yasuda model has the following effects on the shape of the predicted η curve, as shown in Figure 2.6:

- η_∞ : The viscosity function approaches to the constant value η_∞ as $\dot{\gamma}$ gets large.

- η_0 : The viscosity function approaches to the constant value η_0 as $\dot{\gamma}$ becomes small.
- a: The exponent which affects the shape of the transition region between the zero-shear rate plateau and the rapidly decreasing (power-law-like) portion of the viscosity versus shear rate curve. Increasing a sharpens the transition. When $a = 2$, equation (2-14) is known as the Carreau model.
- λ : The parameter which is a time constant for the fluid. The value of λ determines the shear rate at which the transition occurs from the zero-shear rate plateau to the power-law region. It also governs the transition from power-law to $\eta = \eta_\infty$.
- n: a constant same as power-law parameter, which describes the slope of the rapidly decreasing portion of the η curve.

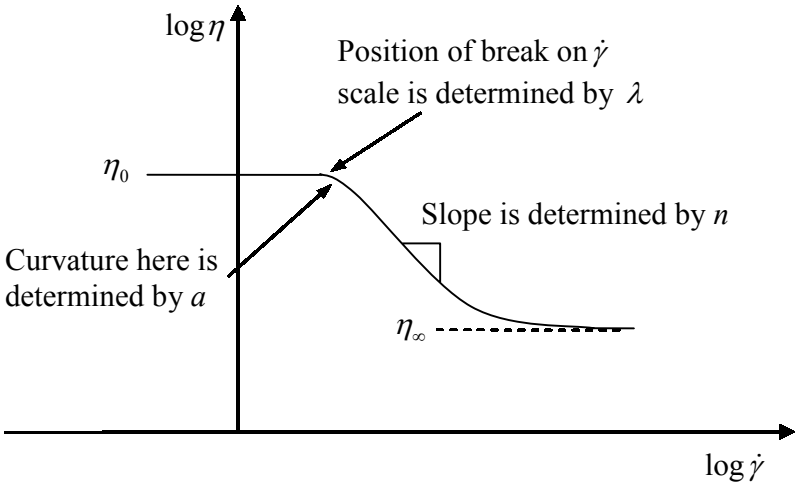

Figure 2.6 Viscosity behaviors as predicted by the Carreau-Yasuda model.

2.2.4 Bingham Model

The Bingham model represents behavior that is fundamentally different from either the power-law or the Carreau-Yasuda model. This model describes fluids that exhibit ae yield stress as shown in Figure 2.7. The viscosity of the Bingham model is given by the following equation (Morrison, 2001)

$$\eta = \begin{cases} \infty & \tau \le \tau_y \\ \mu_0 + \dfrac{\tau_y}{\dot{\gamma}} & \tau > \tau_y \end{cases} \tag{2-15}$$

where τ_y, called the yield stress, is positive. The Bingham model implies that the fluid will not flow until the stress exceeds the yield stress τ_y. When the stress is much higher than the yield stress ($\dot{\gamma} \to \infty$) the fluid flows with a constant viscosity. The Bingham model is a two-parameter model.

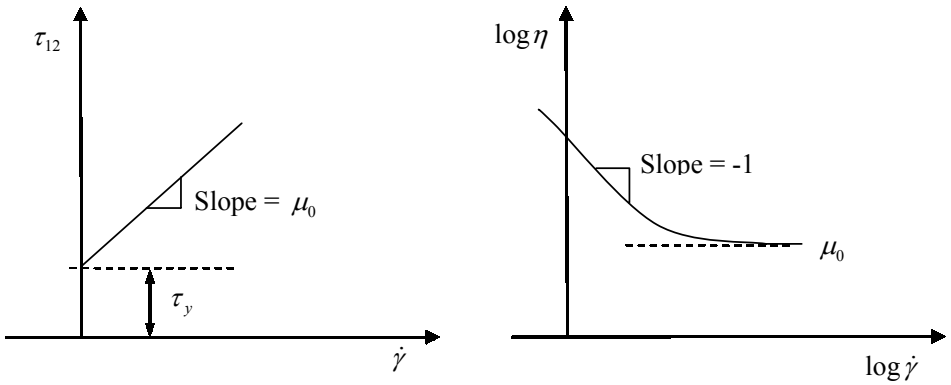

Figure 2.7 Viscosity behaviors as predicted by the Bingham model.

2.2.5 Herschel-Bulkley

As the viscosity of the epoxy-molding compound exhibits a yield stress behavior at low shear rate and a power law behavior at high shear rate, the study reported by Han and Wang (1997a) introduced the Herschel and Bulkley model, in which

$$\tau = \tau_y + K\dot{\gamma}^{(n-1)}\frac{\partial u}{\partial y} \tag{2-16}$$

Noting that $\eta = \tau / \dot{\gamma}$, equation (2-16) becomes

$$\eta = \frac{\tau_y}{\dot{\gamma}} + K\dot{\gamma}^{n-1} \tag{2-17}$$

This equation is called the Herschel-Bulkley equation. In this case, n is the power-law fluid behavior index, $K = m$, and τ_y is the yield stress which is assumed to depend on temperature and be described by:

$$\tau_y = \tau_{y0}\exp\left(\frac{T_y}{T}\right) \tag{2-18}$$

The temperature dependence of viscosity is considered by fitting K in equation (2-17) to the following equation of the Williams-Landel-Ferry (WLF) form (Han and Wang, 1997a):

$$K = K_{00} \exp\left(\frac{-C_A (T - T_g)}{C_B + (T - T_g)} \right) \tag{2-19}$$

where K_{00}, C_A, C_B, T_g are curve-fit parameters.

The above equations imply that the shear dependence is decoupled from the dependence on temperature and the degree of cure. This appears to be an appropriate assumption at low degrees of cure. Han and Wang (1997a) reported that the shear rate dependence remains the same from 70°C to 165°C except in the very low shear-stress range which is not of practical importance. The shear rate dependence of viscosity at low degrees of cure is practically constant.

It should be noted that the encapsulant will not flow unless the shear stress exerted on the encapsulant is higher than the yield stress. For a rectangular cavity, this gives the minimum pressure drop required to fill the cavity for an encapsulant with a yield stress of τ_y, i.e., $\Delta p > 2L\tau_y / h$ (Han and Wang, 1997b).

2.3 Surface Tension

The existence of a tension in a surface or interface is witnessed daily by most people when making lather with soap or detergent, and when wiping up water with a paper towel (Dullien, 1992). With reference to a bubble or a drop, we can consider a spherical cap whose section, as shown in Figure 2.8, is subjected to surface tension σ around the base of the cap and to normal pressures P' and P'' at each point on the surface. The effect of surface tension σ is to reduce the size of the sphere unless it is opposed by a sufficiently large pressure difference between P' and P''. The surface forces, as shown in the figure, are exerted by the rest of the sphere on the cap, which they pull downward. An equal and opposite force (not shown in the figure) is exerted by the cap on the rest of the sphere, pulling it upward.

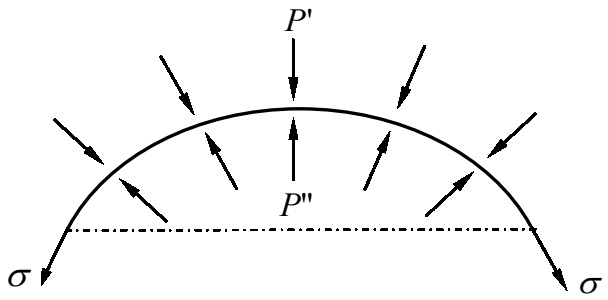

Figure 2.8 Capillary equilibrium of a spherical cap.

The surface is said to be in a state of uniform tension if: (1) at each point, σ is perpendicular to the dividing line and has the same value whatever the direction of this line, and (2) σ has the same value at all points on the surface. In this case, σ can be

called the surface (or interface) tension of the surface (Dullien, 1992). Its dimension is force per unit length, N/m.

2.3.1 Laplace's Equation

Consider an arbitrary smooth surface as shown in Figure 2.9, of which the spherical cap shown in Figure 2.8 is a special case. The effect of gravity is neglected in this analysis. Consider an arbitrary point on the surface and draw on the surface a curve whose distance from P along the surface is a constant ρ. Drawing through P an arbitrary pair of orthogonal lines AB and CD on the surface, and letting their radii of curvature at P be R_1 and R_2, a theorem of Euler (Weatherburn, 1947) states that:

$$\frac{1}{r_1}+\frac{1}{r_2}=\frac{1}{R_1}+\frac{1}{R_2} \tag{2-20}$$

where r_1 and r_2 are the principal radii of curvature.

At point A, an element δl of the boundary line is subjected to a force $\sigma\delta l$ whose projection along the normal PN is

$$\sigma\delta l\sin\phi=\sigma\phi\,\delta l=\sigma\left(\frac{\rho}{R_1}\right)\delta l \tag{2-21}$$

where ϕ is supposed to be very small.

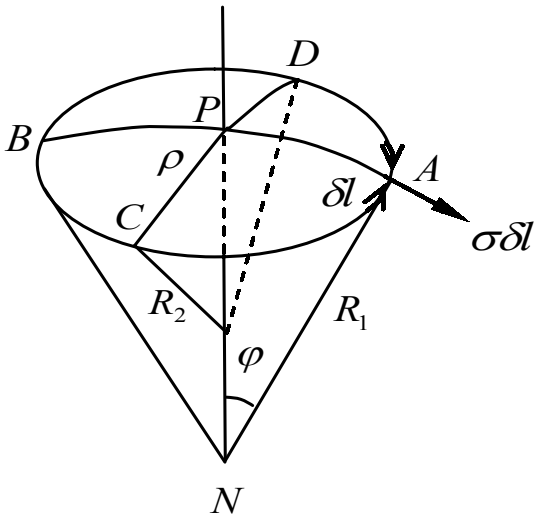

Figure 2.9 Capillary equilibrium of a non-spherical cap.

Considering four elements δl of the periphery at A, B, C, and D, they will contribute the following force:

$$\sigma\delta l\left[2\left(\frac{\rho}{R_1}\right)+2\left(\frac{\rho}{R_2}\right)\right]=2\rho\sigma\delta l\left[\left(\frac{1}{r_1}\right)+\left(\frac{1}{r_2}\right)\right] \tag{2-22}$$

Since this expression is independent of the choice of AB and CD, it can be integrated around the entire circumference. Since four orthogonal elements have been considered, the integration is made over one-quarter of a revolution, which results in

$$\pi\rho^2\sigma\left[\left(\frac{1}{r_1}\right)+\left(\frac{1}{r_2}\right)\right] \tag{2-23}$$

For mechanical equilibrium of the surface, this force is to be balanced exactly by the net pressure force. Therefore,

$$(P'' - P')\pi\rho^2 = \pi\rho^2\sigma\left[\left(\frac{1}{r_1}\right)+\left(\frac{1}{r_2}\right)\right] \tag{2-24}$$

which reduces to the Laplace equation

$$P'' - P' = \sigma\left[\left(\frac{1}{r_1}\right)+\left(\frac{1}{r_2}\right)\right] \tag{2-25}$$

The Laplace equation above shows that due to the existence of surface tension an arbitrary surface can maintain mechanical equilibrium between two fluids at different pressures P' and P''. The phase on the concave side of the surface must have a pressure P'' that is greater than the pressure P' on the convex side.

2.3.2 Young's Equation

Capillary systems always involve a solid phase and at least two fluid phases. Consider a drop of liquid placed on a smooth solid surface as shown in Figure 2.10. Depending on conditions that will be discussed below, the liquid may remain a drop displaying a finite contact angle θ between the two boundaries: liquid/gas and solid/liquid. The contact angle θ is defined as the angle subtended by the tangent to the liquid/gas boundary constructed at a point on the three-phase line of contact and the tangent to the solid/liquid boundary constructed at the same point. For equilibrium, the force components parallel to the solid surface balances so that one can obtain (Hocking and Rivers, 1982; Adam, 1930)

$$\sigma_{SG} - \sigma_{SL} = \sigma_{LG} \cos\theta \tag{2-26}$$

where σ_{LG} and σ_{SG} are the surface tension of the liquid and solid, respectively, σ_{SL} is the interfacial tension between the liquid and solid phase, and θ is a contact angle of a liquid droplet on a given surface. The difference $\sigma_{SG} - \sigma_{SL}$ is termed the "wetting tension" or "adhesion tension". This equation was first given by Young for a liquid drop resting on a solid surface in air and relates the contact angle to the surfaces tensions of the three interfaces.

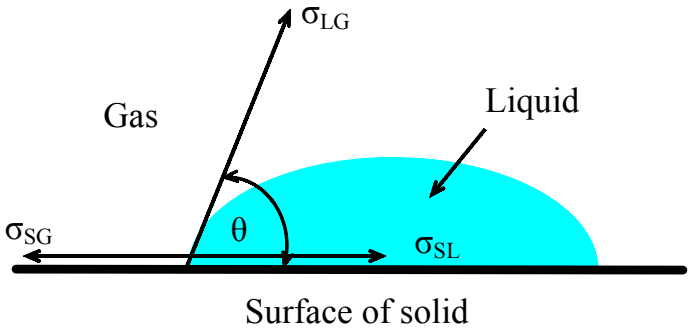

Figure 2.10 Equilibrium state of a drop of liquid laying on the smooth solid surface.

2.3.3 Surface tension in capillary flow between two parallel plates

For capillary flow in a channel, the relationship of the principal radii, r_1 and r_2, to the channel geometry is shown in Figure 2.11. Assuming that the contact angle between the fluid and the top plane wall (Figure 2.11b) is the same as that between the fluid and the side plane wall (Figure 2.11 a), the principal radii are determined based on the following equations:

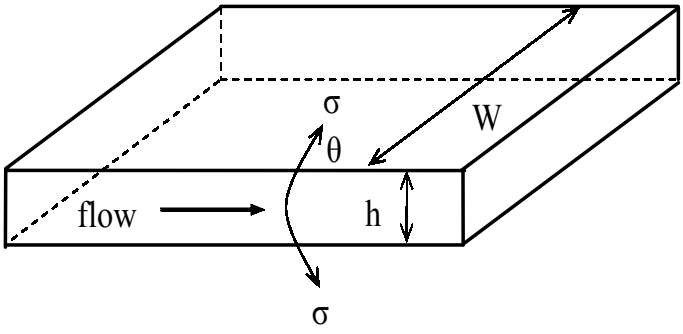

(a)

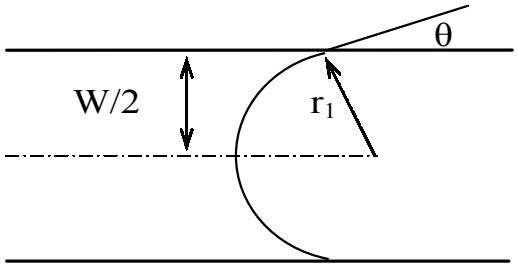

(b)

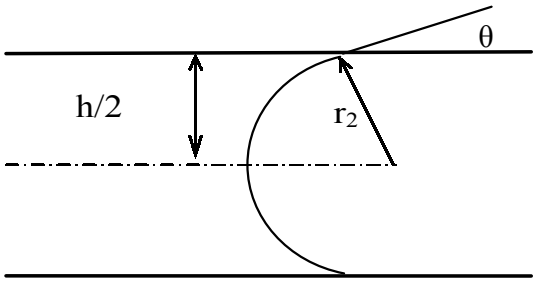

(c)

Figure 2.11 (a) Channel flow driven by surface tension between two parallel plats, (b) flow front shape in width direction, (c) flow front shape in cavity thickness direction

$$r_1 = \frac{W}{2\cos\theta} \tag{2-27a}$$

$$r_2 = \frac{h}{2\cos\theta} \tag{2-27b}$$

where W and h denote the width and thickness of the channel, respectively. Substituting equation (2-27) into (2-25) results in

$$P'' - P' = 2\sigma\cos\theta\left(\frac{1}{W} + \frac{1}{h}\right) \tag{2-28}$$

2.4 Experimental Investigation of Encapsulant Material

In the experimental investigation performed in Assembly Automation Limited, Hong Kong, the underfill material FP4530, made by Dexter Corporation, USA, was chosen, which is a kind of non-Newtonian fluid and is used as an underfill material in flip-chip packaging. The experimental approach and data analysis method are also applicable to other underfill materials used in electronics packaging. The underfill material was stored below -40°C. Before it was used for experiments, it was taken out and thawed for about one hour. For each measurement, a fresh degassed sample was used to eliminate the previous shear history as an additional variable. Degassing was accomplished by placing the sample in a syringe at room temperature until no trapped air was observed.

2.4.1 Cone-and-Plate Rheometer

Numerous instruments employing different rheometric approaches are available commercially for performing rheological measurements. The basic features of the rheometric approaches and main instrument types for their implementation are presented in many textbooks and research papers (Chhabra and Richarson 1999; Macosko, 1994; Barnes et al. 1989).

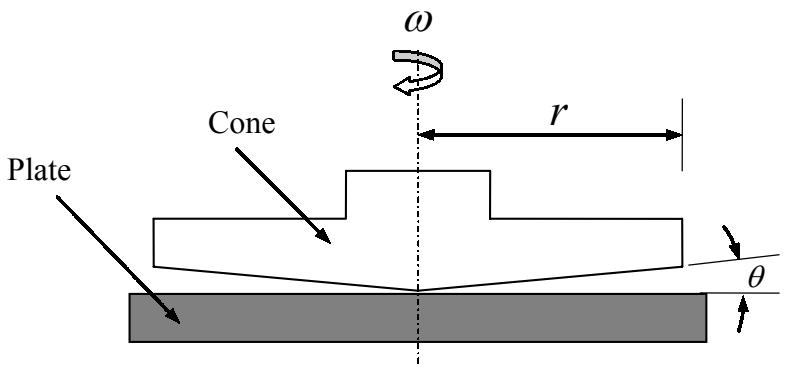

Figure 2.12 Cone-and-plate rheometer geometry.

In this study, a rheometer (DV-III V3.3 with accuracy: ±1.0% of range), made by the Brookfield Engineering Laboratories, Middleboro, U.S.A, was used. It employs a cone-and-plate geometry, as shown in Figure 2.12, consisting of a conical vertex perpendicular to and in point contact with a flat plate. The test sample of the fluid is sheared under torsion within the gap between the cone and plate. The cone is usually made very obtuse (θ less than 4°), and this small cone angle ensures that the shear rate is nearly constant throughout the shearing gap. The basic measurement of the rheometer is the summation of the torque over the conical surface as a function of cone angular

velocity, from which the fundamental flow curve of shear stress versus shear rate can be obtained. The shear stress and shear rate are related to the torque and the cone angular velocity, respectively, as follows (Macosko, 1994)

$$\tau = \frac{3T}{2\pi r^3} \tag{2-29a}$$

and

$$\dot{\gamma} = \frac{\omega}{\sin\theta} \tag{2-29b}$$

where τ is the shear stress, T the torque, r the radius of the cone, $\dot{\gamma}$ the shear rate, and ω the cone angular velocity.

2.4.2 Viscosity

Using the rheometer described above, the viscosity of the filling material was measured at different shear rates and temperatures. In the experiments, the spindle radius of the rheometer with cone geometry was 12 mm and the cone angle was 3°. A fluid sample of 0.5 ml was required to fill the shearing gap between the cone and plate. During the test period, the temperature of the cone-and-plate could be controlled within ± 0.1 °C by using an embedded temperature probe and a constant temperature bath (Brookfield, Middleboro, U.S.A). For the results measured at each temperature as shown in Figure 2.13, the viscosity was fitted to the shear rate using the following power-law constitutive equation:

$$\eta = m\dot{\gamma}^{n-1} \tag{2-10}$$

in which, m and n are curve-fitting parameters. The average relative errors of the regression of the viscosity are 2.4%, 2.3%, and 6.7% for the temperatures of 45°C, 55°C, and 60°C, respectively.

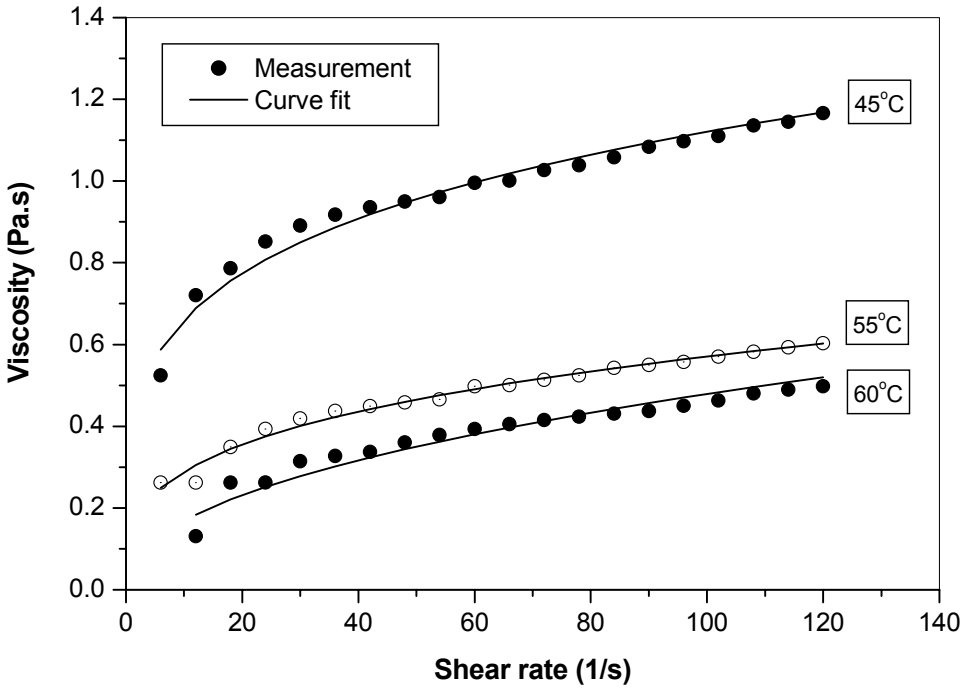

Figure 2.13 Viscosities versus shear rate for different temperature.

From the results shown in Figure 2.13, it can be seen that the viscosity of the material can be adequately fitted to the shear rate using the power-law constitutive equation. Further study found that the curve-fitting parameters, m and n, are temperature

dependent, as shown in Figures 2.14 and 2.15. The dependence of m and n on temperature can be fitted to the following equations, respectively:

$$n = 2.58T^{-0.47672}e^{0.020556T} \tag{2-30}$$

$$m = 5.178762T^{1.076614}e^{-0.14701T} \tag{2-31}$$

The multiple R in Figures 2.14 and 2.15 are 0.953 and 0.995 respectively.

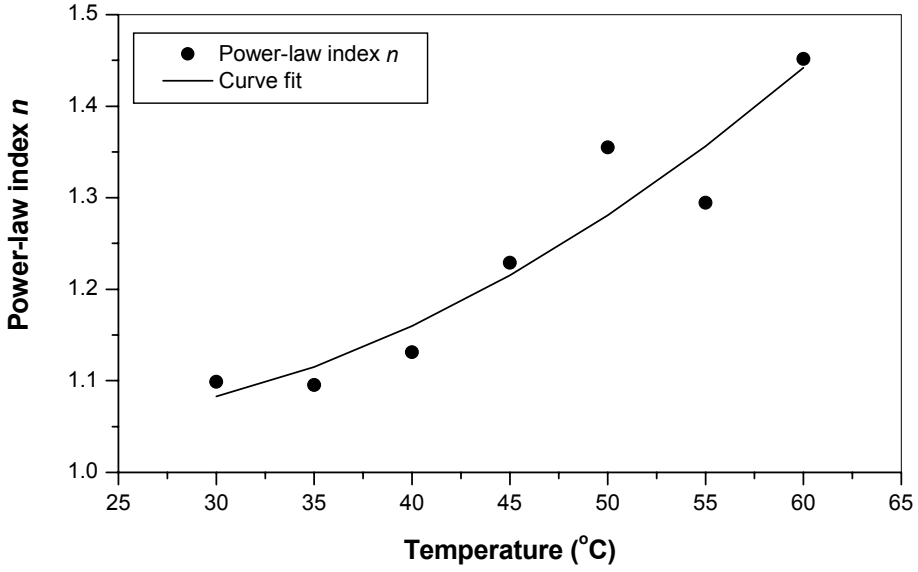

Figure 2.14 Variation of coefficient n with temperature.

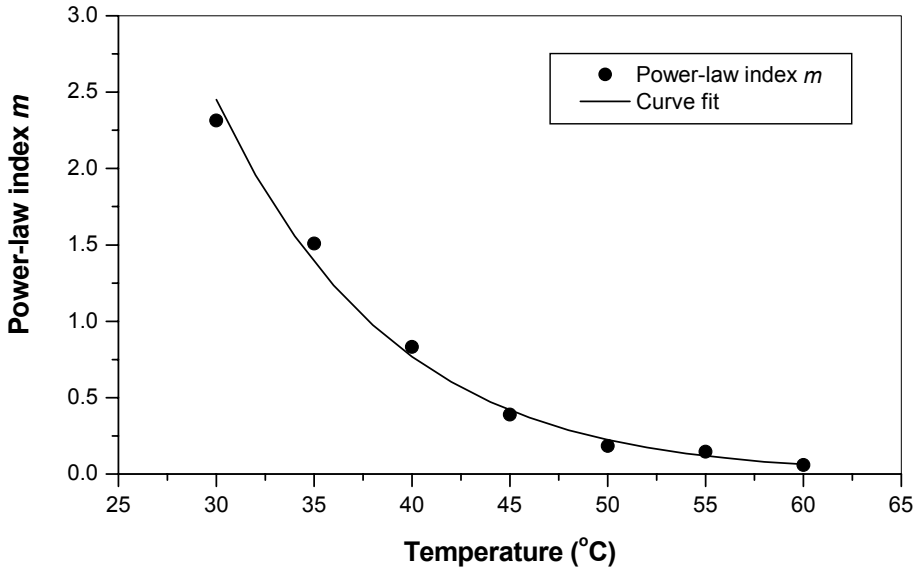

Figure 2.15 Variation of coefficient *m* with temperature.

2.4.3 Surface Tension and Contact Angle

The surface tension and contact angle in this study were measured with the DGD-ASE Contact Angle Meter shown in Figure 2.16, made by GBX Company, France. The surface tension of the liquid was measured using the drop weight method. This is a fairly accurate method and perhaps the most convenient laboratory approach for measuring the surface tension of a liquid-air interface. This method is very old, remarks on it having been made by Tate (1864). A simple expression for the weight W of a drop suspended from a tube is given by what is known as Tate's law:

$$W = 2\pi r\sigma \tag{2-32}$$

where W is the weight of a drop, and r the radius of tube. Equation (2-32) indicates that the maximum force available to support weight W of the drop is given by the surface tension force times the circumference of the tip.

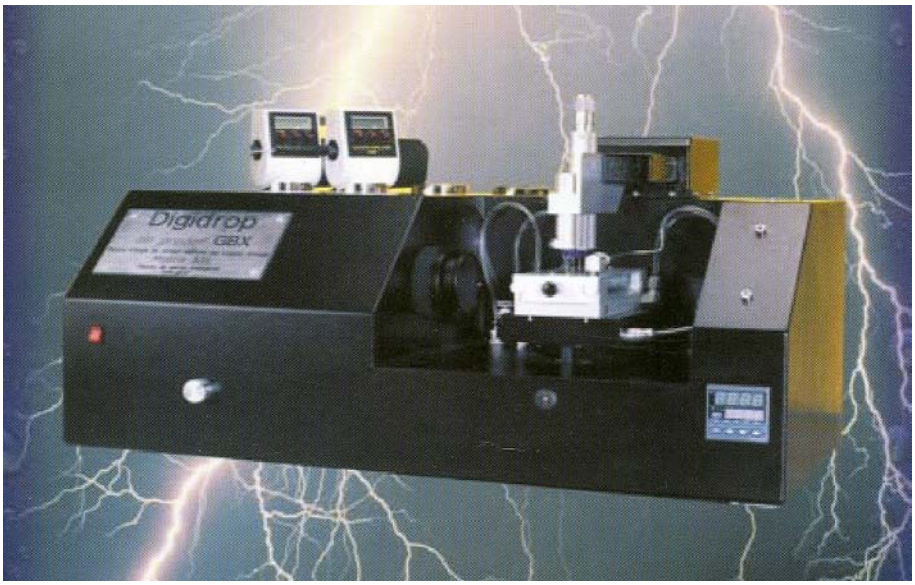

Figure 2.16 DGD-ASE Contact Angle Meter (GBX, France)

In practice, a correction factor f is used for equation (2-32), i.e.,

$$W = 2\pi r\sigma f \tag{2-33}$$

The reason for this becomes evident when the process of drop formation is observed closely. What actually happens is illustrated Figure 2.17. The small drops arise from the mechanical instability of the thin cylindrical neck that develops. In any event, it is clear

that only a portion of the drop that has reached the point of instability actually falls. As much as 40% of the liquid may remain attached to the tip (Adamson, 1990).

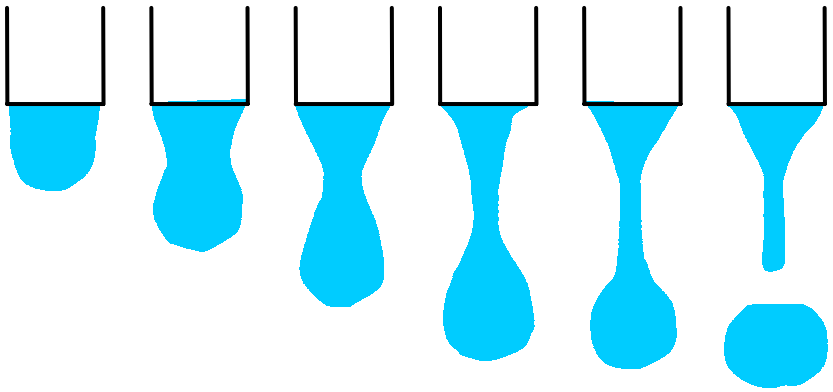

Figure 2.17 Development process of a drop formation.

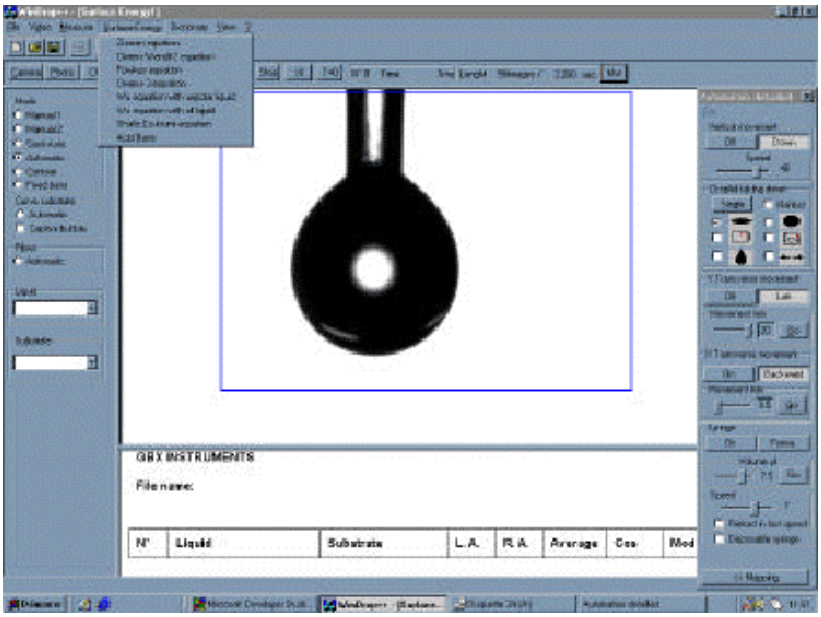

Figure 2.18 Pendant method measures the surface tension of the liquid.

In this instrument, the sample syringe can be precisely adjusted along all three axes using precision drives. The drop image contrast is optimized using variable intensity illumination. The built-in Microsoft® Window's software is used to process images acquired by the video camera, as shown in Figure 2.18. The built-in program calculates the surface tension of the liquid at different times using Equation (2-33) according to the material property data, cylindrical neck diameter, and the measured drop dimensions.

For the contact angle measurements, the Microsoft® Window's software processes the images acquired by the video camera to define the drop boundary reliably. Images of drops are fitted to yield contact angle data. Contact angles are measured at the tangent lines to the surface (see Figure 2.19) and the mean value $\theta = (\theta_1 + \theta_2)/2$ is calculated.

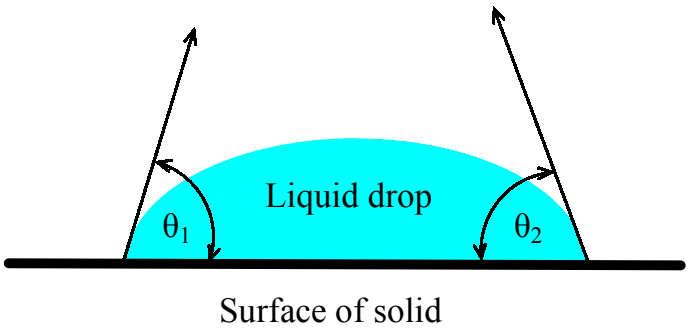

Figure 2.19 Tangent lines at the borders of the liquid drop.

Since both surface tension and contact angle decrease with an increase in temperature, the surface tension and contact angle were measured from 30 to 90°C as shown in Figures 2.20 and 2.21, respectively. They were fitted to the temperature using a second-order polynomial,

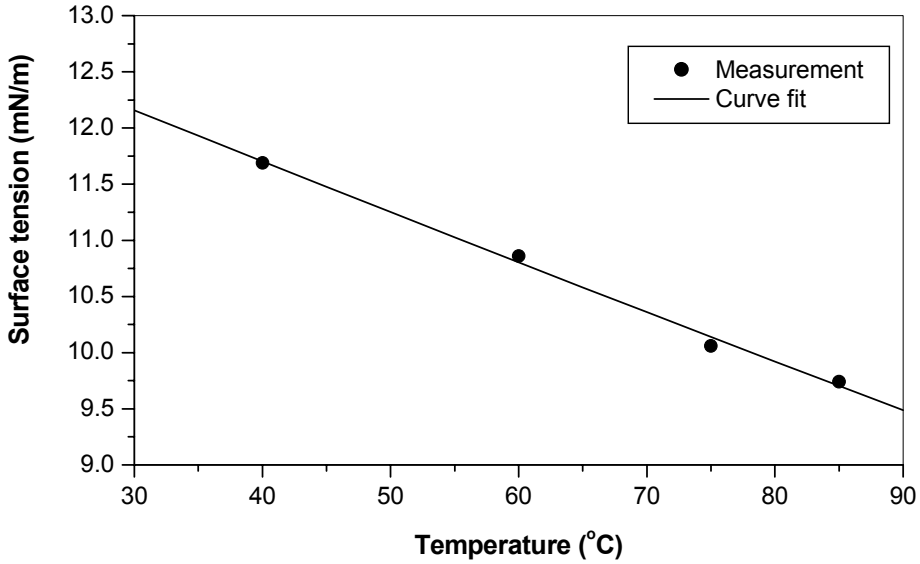

Figure 2.20 Surface tension versus temperature.

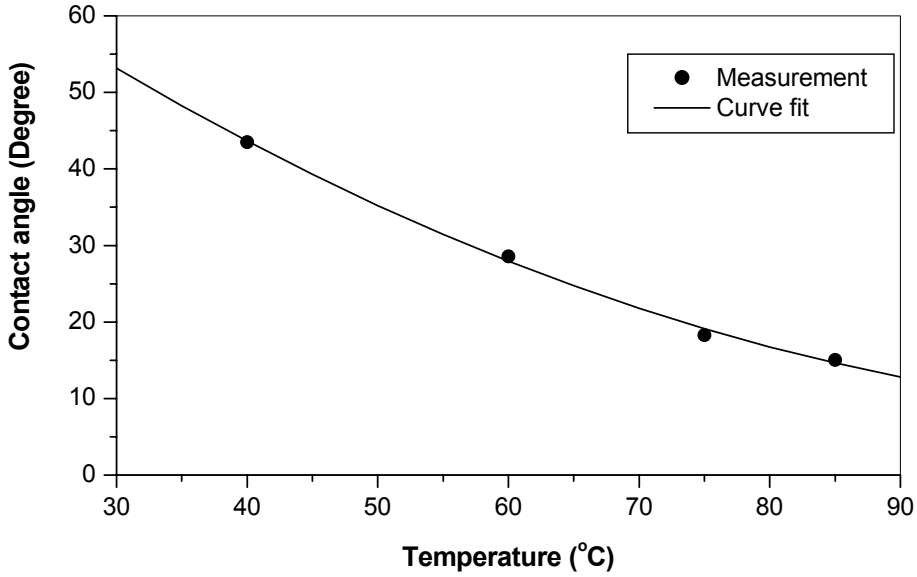

Figure 2.21 Contact angle versus temperature.

$$\sigma = 13.55113 - 0.04701T + 2.04 \times 10^{-5} T^2 \tag{2-34}$$

$$\theta = 88.47453 - 1.34561T + 0.00561T^2 \tag{2-35}$$

where σ is the surface tension coefficient (mN/m), θ is the contact angle (degree), and T the temperature (°C).

2.5 Summary

This chapter presents a brief introduction to the rheological properties of non-Newtonian fluids. One of the distinct characteristics of most fluids used for flip-chip packaging is that the relationship between shear stress and shear rate is non-linear at a given temperature and pressure. The fluid behaviour is said to be time-dependent if it depends on the shearing time, and otherwise time-independent. Some constitutive equations applicable to viscous time-independent liquids are presented. As far as the underfill materials used in flip-chip packaging, the dependency of viscosity on the shear rate and temperature is more important than that of viscosity on time.

In this chapter, the power-law model was reviewed, which describes the rheological behaviour between viscosity and shear rate at a given temperature. The dependency of viscosity on temperature was described using the index m and n of power-law model. Both parameters m and n were fitted as a function of temperature. An experimental

method was used to investigate the rheological behaviour of a typical underfill material FP4530 used in flip-chip packaging, including the dependencies of its viscosity on shear rate and temperature. The experimental results were compared to the correlation using the power-law model, indicating a good agreement between them.

3 ANALYSIS OF UNDERFILL FLOW WITH CONSIDERATION OF TRANSIENT BEHAVIOR

3.1 Introduction

From the discussion in Chapter 1, it is noted that most of the studies reported in the literature applied the Washburn model for two parallel plates to predict the performance of underfill flow in flip-chip packaging. Unfortunately, the result predicted by the Washburn model did not agree well with the results measured in flip-chip packaging. The possible causes for these discrepancies are: (1) the transient behavior of the flow may have an effect on the overall behavior of the underfill flow; (2) the effect of solder bump resistance on the flow may be significant; and (3) the Washburn model is only valid for a Newtonian fluid, whereas the encapsulant fluid in flip-chip packaging shows appreciable non-Newtonian behavior.

In this chapter, the first and the second causes are examined. A second goal of this chapter is to present a model which extends the Washburn model by considering the dynamic contact angle and also the resistance due to the solder bump. This model will be compared with the analytical model developed by Han and Wang (1997a), in which they extended the Washburn model to consider dynamic contact angle but neglected the

resistance of the solder bump. For convenience, their model will be called the Han-Wang model.

3.2 Underfill Flow Analysis between Two Parallel Plates

In this analysis for the underfill flow process shown in Figure 3.1 (the earlier Figure 1.8), it is assumed that:

(1) the fluid is incompressible with Newtonian behavior;

(2) the flow is two-dimensional fully developed laminar flow and neglects gravity;

(3) there is no slip between the fluid and solid wall

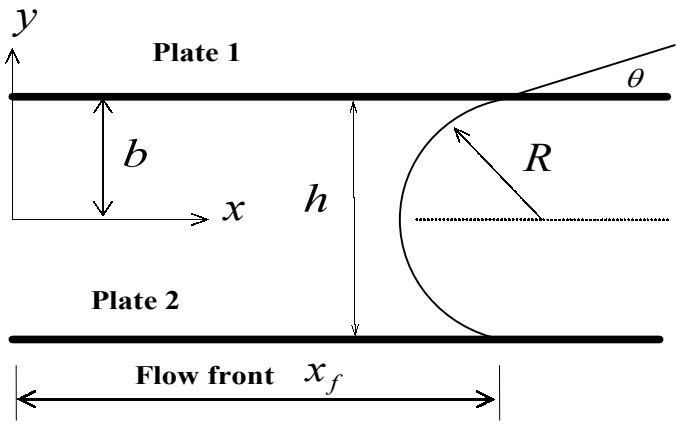

Figure 3.1 Flow between two parallel plates

Under these assumptions, $\frac{\partial}{\partial z} = 0$, $\frac{\partial u}{\partial x} = 0$, $w = 0$. From the continuity equation (A-1) in Appendix A, it concludes that

$$v = 0 \tag{3-1}$$

The momentum equations (A-6) to (A-8) considered in Appendix A simplify to

X-component:

$$\rho \frac{\partial u}{\partial t} = -\frac{\partial p}{\partial x} + \mu \frac{\partial^2 u}{\partial y^2} \tag{3-2}$$

Y-component:

$$0 = -\frac{\partial p}{\partial y} \tag{3-3}$$

Z-component:

$$0 = -\frac{\partial p}{\partial z} \tag{3-4}$$

From the simplified momentum equations (3-3) and (3-4), it can be seen that the pressure is only a function of x, i.e., $p = p(x)$. Rewriting equation (3-2) gives

$$\frac{1}{\nu} \frac{\partial u}{\partial t} = -\frac{1}{\mu} \frac{dp}{dx} + \frac{\partial^2 u}{\partial y^2} \tag{3-5}$$

where $\nu = \frac{\mu}{\rho}$ is the kinematic viscosity. The initial and boundary conditions for the flow are, respectively, given by:

$$u(y,0) = 0 \tag{3-6}$$

$$\frac{\partial u(0,t)}{\partial y} = 0 \tag{3-7a}$$

$$u(b,t) = 0 \tag{3-7b}$$

The above model, i.e., equations (3-5) to (3-7), cannot be solved by the method of separation of variables because of non-homogeneity. However, the decomposition the velocity field into steady and unsteady components, i.e.

$$u(y,t) = \overline{u}(y) + u'(y,t) \tag{3-8}$$

overcomes this difficulty. Let $\overline{u}$ and u' satisfy, respectively,

$$0 = -\frac{1}{\mu}\frac{\partial p}{\partial x} + \frac{\partial^2 u}{\partial y^2} \tag{3-9}$$

$$\frac{\partial \overline{u}(0)}{\partial y} = 0\,,\ \overline{u}(b) = 0 \tag{3-10}$$

and

$$\frac{1}{\nu}\frac{\partial u'}{\partial t} = \frac{\partial^2 u'}{\partial y^2} \tag{3-11}$$

$$u'(y,0) = -\overline{u}(y) \tag{3-12}$$

$$\frac{\partial u'(0,t)}{\partial y} = 0 \tag{3-13a}$$

$$u'(b,t) = 0 \tag{3-13b}$$

The solution for the steady part of the problem, i.e., equations (3-9) and (3-10), is Poiseuille flow, given by

$$\overline{u} = -\frac{dp/dx}{2\mu}(b^2 - y^2) \tag{3-14}$$

The solution for the unsteady problem, i.e., equations (3-11) to (3-13), can be obtained by the method of separation of variables and is given by (Arpaci, 1966)

$$u'(y,t) = \sum_{n=0}^{\infty} a_n \exp(-\lambda_n^2 \nu t)\cos\lambda_n y \tag{3-15}$$

where $\lambda_n b = \dfrac{(2n+1)\pi}{2}$, $n = 0, 1, 2, 3, \cdots$,

and

$$a_n = -2\frac{(-dp/dx)}{\mu}\frac{(-1)^n b^2}{(\lambda_n b)^3}$$

Substituting equations (3-14) and (3-15) into equation (3-8) results in the unsteady velocity distribution, i.e.,

$$\frac{u(y,t)}{\left(-\dfrac{dp}{dx}\right)\dfrac{b^2}{\mu}} = \frac{1}{2}\left[1-\left(\frac{y}{b}\right)^2\right] - 2\sum_{n=0}^{\infty}\frac{(-1)^n}{(\lambda_n b)^3}\exp(-\lambda_n^2 \nu t)\cos\lambda_n y \qquad (3\text{-}16)$$

The speed of the flow-front is equal to the mean velocity, which is given by

$$\begin{aligned} u_m &= \frac{1}{b}\int_0^b u\,dy \\ &= \frac{1}{b}\left(-\frac{dp}{dx}\right)\frac{b^2}{\mu}\left[\int_0^b \frac{1}{2}\left(1-\left(\frac{y}{b}\right)^2\right)dy - 2\sum_{n=0}^{\infty}\frac{(-1)^n}{(\lambda_n b)^3}\exp(-\lambda_n^2 \nu t)\int_0^b \cos(\lambda_n y)\,dy\right] \end{aligned}$$

in which

$$\int_0^b \frac{1}{2}\left[1-\left(\frac{y}{b}\right)^2\right]dy = \frac{1}{3}b$$

and

$$\int_0^b \cos(\lambda_n y)dy = \frac{1}{\lambda_n}\sin(\lambda_n b) = \frac{1}{\lambda_n}\sin\left(\frac{(2n+1)\pi}{2}\right) = \frac{(-1)^n}{\lambda_n}$$

Therefore

$$u_m = \left(-\frac{dp}{dx}\right)\frac{b}{\mu}\left[\frac{1}{3}b - 2\sum_{n=0}^{\infty}\frac{(-1)^n}{(\lambda_n b)^3}\exp(-\lambda_n^2 \nu t)\frac{(-1)^n}{\lambda_n}\right]$$

or

$$u_m = \frac{dx_f}{dt} = \left(-\frac{dp}{dx}\right)\frac{b^2}{\mu}\left[\frac{1}{3} - 2\sum_{n=0}^{\infty}\frac{1}{(\lambda_n b)^4}\exp(-\lambda_n^2 \nu t)\right] \tag{3-17}$$

Notice that dp/dx is assumed as constant, so that in terms of the external pressure and the pressure at the flow front,

$$-\frac{dp}{dx} = \frac{p_0 - p_f}{x_f} = \frac{\Delta p}{x_f}$$

Thus

$$\frac{dx_f}{dt} = \frac{\Delta p b^2}{x_f \mu}\left[\frac{1}{3} - 2\sum_{n=0}^{\infty}\frac{1}{(\lambda_n b)^4}\exp(-\lambda_n^2 \nu t)\right] \tag{3-18}$$

Integration of equation (3-18) leads to

$$x_f^2 = \frac{2\Delta p b^2}{\mu}\left[\frac{1}{3}t - 2\sum_{n=0}^{\infty}\frac{1}{(\lambda_n b)^4}\frac{1}{\lambda_n^2 \nu}(1-\exp(-\lambda_n^2 \nu t))\right] \tag{3-19}$$

or

$$x_f^2 = \frac{2\Delta p b^2}{\mu}\left[\frac{1}{3}t - 2\sum_{n=0}^{\infty}\frac{1}{(\lambda_n b)^4 \lambda_n^2 \nu} - 2\sum_{n=0}^{\infty}\frac{\exp(-\lambda_n^2 \nu t)}{(\lambda_n b)^4 \lambda_n^2 \nu}\right] \tag{3-20}$$

3.3 Effect of Time on the Flow Front

Equation (3-20) consists of two time-dependent parts. First, the term $\exp(-\lambda_n^2 \nu t)$ in the second series is examined. The variation of $\exp(-\lambda_n^2 \nu t)$ versus time is plotted in Figure 3.2 for different *n* and a gap height of 100 μm; the specific data is also listed in Table 3.1. These results show that this term drops very quickly with increase of time. When *n* is greater than or equal to 1, this term reduces to almost zero just after 0.002 s. This means that it is sufficient to take one term (*n* = 0) for considering the influence of time on the term $\exp(-\lambda_n^2 \nu t)$. That is, by taking $\lambda_0 = \frac{\pi}{2b} = \frac{\pi}{h}$, equation (3-20) becomes

$$x_f^2 = \frac{2\Delta p b^2}{3\mu}t - \frac{4\Delta p b^2}{\mu}\left(1-\exp(-\frac{\pi^2}{h^2}\nu t)\right)\sum_{n=0}^{\infty}\frac{1}{(\lambda_n b)^4}\frac{1}{\lambda_n^2 \nu} \tag{3-20b}$$

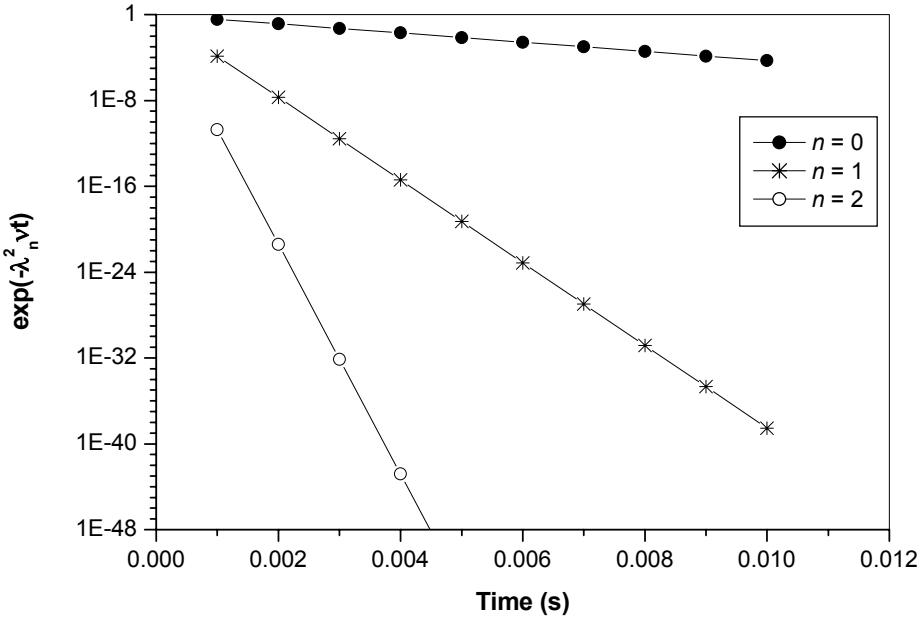

Figure 3.2 Term $\exp(-\lambda_n^2 vt)$ versus n (the gap height h = 100 μm).

Table 3.1 Term $\exp(-\lambda_n^2 vt)$ versus different n

(Fluid: water with the gap height h = 100 μm).

Time (s)	*n=0*	*n=1*	*n=2*
0.001	3.73E-01	1.40E-04	1.97E-11
0.002	1.39E-01	1.96E-08	3.89E-22
0.003	5.19E-02	2.75E-12	7.68E-33
0.004	1.94E-02	3.85E-16	1.51E-43
0.005	7.23E-03	5.38E-20	2.99E-54
0.006	2.70E-03	7.54E-24	5.89E-65
0.007	1.01E-03	1.06E-27	1.16E-75
0.008	3.75E-04	1.48E-31	2.29E-86
0.009	1.40E-04	2.07E-35	4.53E-97
0.01	5.22E-05	2.90E-39	8.9E-108

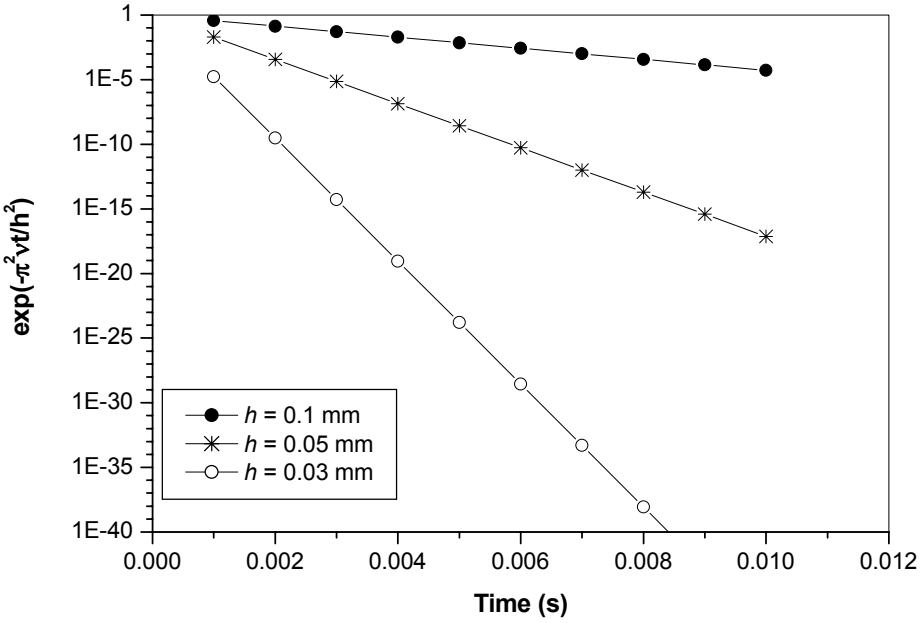

Figure 3.3 Term $\exp(-\lambda_n^2 \nu t)$ versus different gap heights (the fluid: water).

Table 3.2 Term $\exp(-\lambda_n^2 \nu t)$ versus different gap heights (Fluid: water with $n = 0$).

Time (s)	h=100 μm	h=50 μm	h=30 μm
0.001	3.73E-01	1.94E-02	1.75E-05
0.002	1.39E-01	3.75E-04	3.05E-10
0.003	5.19E-02	7.27E-06	5.33E-15
0.004	1.94E-02	1.41E-07	9.31E-20
0.005	7.23E-03	2.73E-09	1.63E-24
0.006	2.70E-03	5.29E-11	2.84E-29
0.007	1.01E-03	1.02E-12	4.96E-34
0.008	3.75E-04	1.98E-14	8.67E-39
0.009	1.40E-04	3.85E-16	1.51E-43
0.01	5.22E-05	7.45E-18	2.65E-48

In equation (3-20b), the effect of the gap height on the term $\exp(-\pi^2 \nu t / h^2)$ with respect to time is plotted in Figure 3.3. The specific value is further listed in Table 3.2. From these results, it can be seen that the term $\exp(-\pi^2 \nu t / h^2)$ drops very quickly with an increase of time. For a cavity thickness of 50 μm, the term $\exp(-\pi^2 \nu t / h^2)$ drops nearly to zero in just 0.001 s. For comparison note that the fast-flow underfill materials used today take about 40 s to underfill a common-size chip (6 mm x 6 mm) with a gap height of 50 μm. Since the cavity thickness in the flip-chip package is usually around 50 μm and the viscosities of encapsulant materials are greater than the viscosity of water, it is reasonable to drop the second term $\exp(-\pi^2 \nu t / h^2)$ in equation (3-20b) for the underfill flow in a micro-cavity. Thus, equation (3-20b) can be approximated as

$$x_f^2 \approx \frac{2\Delta p b^2}{3\mu} t - \frac{4\Delta p b^2}{\mu} \sum_{n=0}^{\infty} \frac{1}{(\lambda_n b)^4 \lambda_n^2 \nu} \tag{3-21}$$

In Appendix C, it is shown that with respect to the sum in equation (3-21), the relative error introduced by taking only the first term of the series is less than 1.6%. Therefore, it is sufficiently accurate to retain only the first term of the sum, so that equation (3-21) becomes

$$x_f^2 = \frac{h^2 \Delta p}{2\mu} \left(\frac{1}{3} t - \frac{32 h^2}{\pi^6 \nu} \right) \tag{3-22}$$

The filling time can be obtained from equation (3-22) as

$$t_f = \frac{6\mu}{h^2 \Delta p} x_f^2 + \frac{96h^2}{\pi^6 \nu} \tag{3-23}$$

In the case of underfill flow driven by capillary action, the pressure Δp is the pressure Δp_σ due to the surface tension. The pressure Δp_σ can be calculated using the following equation (Kim et al., 2002; Schwiebert and Leong, 1996)

$$\Delta p_\sigma = \frac{\sigma}{R} = \frac{2\sigma \cos\theta}{h} \tag{3-24}$$

Substituting equation (3-24) into equation (3-22) and (3-23), respectively, gives

$$x_f^2 = \frac{h\sigma \cos\theta}{\mu}\left(\frac{1}{3}t - \frac{32h^2}{\pi^6 \nu}\right) \tag{3-25}$$

$$t_f = \frac{3\mu}{h\sigma \cos\theta} x_f^2 + \frac{96h^2}{\pi^6 \nu} \tag{3-26}$$

From equation (3-26), it can be seen that the second term, which is associated with the unsteady flow process, is only related to the cavity thickness and the viscosity of the encapsulant. Let Δt_f denote the unsteady part of the filling time, i.e.,

$$\Delta t_f = \frac{96h^2}{\pi^6 \nu} \tag{3-27}$$

Table 3.3 Δt_f caused by unsteady process.

Materials	μ (Pa·s)	ν (m^2/s)	$\Delta t_f = 96h^2/\pi^6\nu$ (s)		
			h=100 μm	h=50 μm	h=30 μm
Water	0.001	$1.01\text{x}10^{-6}$	$9.9\text{x}10^{-4}$	$2.50\text{x}10^{-4}$	$8.9\text{x}10^{-5}$
SAE 30 oil	0.29	$3.25\text{x}10^{-4}$	$3.08\text{x}10^{-6}$	$7.70\text{x}10^{-7}$	$2.77\text{x}10^{-7}$
Glycerin	1.5	$1.18\text{x}10^{-3}$	$8.49\text{x}10^{-7}$	$2.12\text{x}10^{-7}$	$7.64\text{x}10^{-8}$

Table 3.3 lists the value of Δt_f for three different fluids with different viscosities and cavity thicknesses. From the equation 3-27 and the results shown in Table 3.3, it can be seen that the Δt_f decreases with a decrease in the cavity thickness and an increase in the viscosity. Since the cavity thickness in a flip-chip package is around 50 μm, and the viscosities of encapsulant materials are greater than the viscosity of water, the correction term Δt_f due to the transient behavior of a flow driven by surface tension can be neglected.

To verify the above conclusion, Table 3.4 lists the errors caused when only the steady part is considered for the three encapsulant materials reported by Nguyen et al. (1999). The maximal relative error is found to be 0.00014 % for material C with gap thickness h=100 μm. When the cavity thickness is less than 50 μm, the maximal error is less than 0.000017%.

Table 3.4 Relative error caused by use of steady model.

Encapsulant material	A	B	C	
Viscosity (Pa-s)	0.7	0.34	0.165	Gap height (μm)
Density (kg/m^3)	1600	1600	1700	
Surface tension (N/m)	0.027	0.027	0.031	
Contact angle (degree)	25.5	20.4	17.5	
Filling time calculated with unsteady model (s)	38.68272 77.36544 128.9424	18.09322 36.18644 60.31073	7.515784 15.03155 25.05258	100 50 30
Filling time calculated with steady model (s)	38.68272 77.36544 128.9424	18.09322 36.18644 60.31072	7.515774 15.03155 25.05258	100 50 30
Relative error (%)	5.9×10^{-6} 7.38×10^{-7} 1.6×10^{-7}	2.6×10^{-5} 3.25×10^{-6} 7.01×10^{-7}	1.37×10^{-4} 1.7×10^{-5} 3.7×10^{-6}	100 50 30

3.4 Analysis of the Flow Resistance in the Flip-chip Package

Studies (Wang, 2002; Kim et al., 2002; Han and Wang, 1997a; Gordon et al., 1999; Gamota and Melton, 1996; Schwiebert and Leong, 1996) reported in the literature applied the Washburn model (1921) to the case of two parallel plates. The studies reported by Nguyen et al. (1999) and Lehmann et al. (1998) showed that the Washburn

model gives a poor prediction in the case of underfill flow in the flip-chip package. One possible reason is that the Washburn model does not consider the influence of the solder bump resistance on underfill. The experimental results, as shown in Figure 3.3 (Fine et al., 2000), clearly show that the filling material in the perimeter array flows faster than in the full array packaging. This implies that the flow resistance caused by the solder bump has significant effect on the underfill flow and it should not be neglected in the underfill flow analysis in flip-chip packaging. The following section develops a method to estimate the solder bump resistance in flip-chip underfill flow.

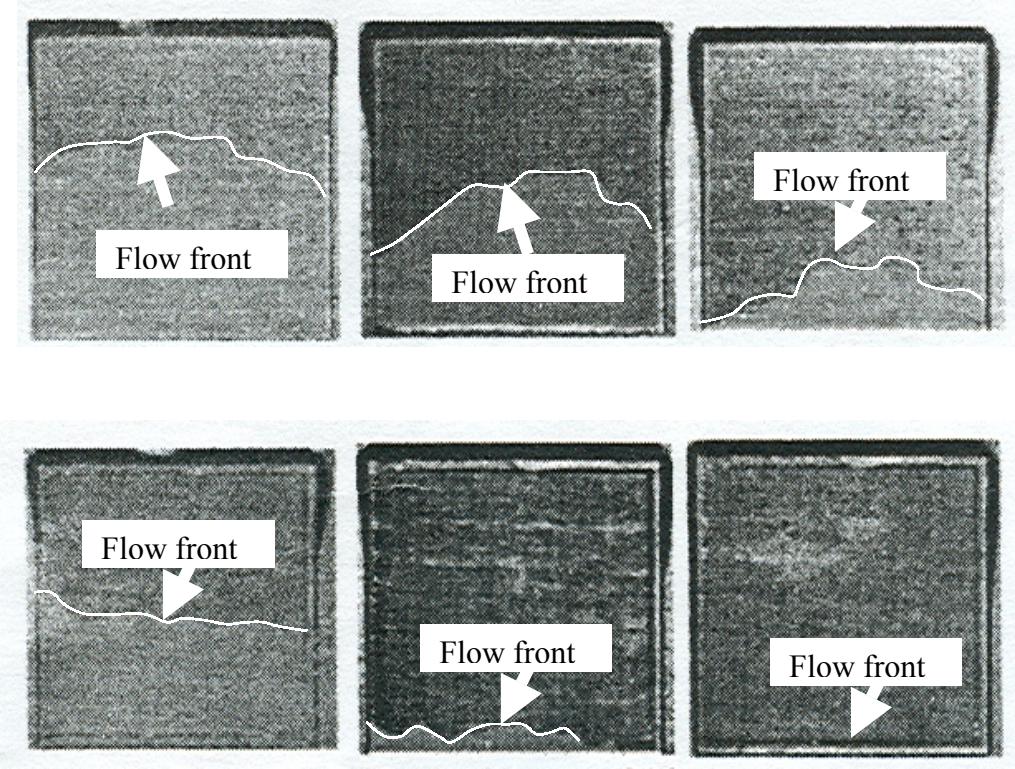

Figure 3.4 The flow front on test flip-chip package at 10, 25, and 45 s. (Top: Full array with 200 μm pitch, Bottom: Perimeter array with 200 μm pitch) (Fine et al., 2000, © 2000 IEEE, reprinted with permission).

The full array solder bump pattern, as a generic feature of the flip-chip package, is described in Figure 3.5. The solder bump pattern can be represented by a three–row array as a representative structure (Figure 3.5a). Based on the assumption that underfill flow consists of a set of one dimensional channel flows, the problem can be further simplified to that shown in Figure 3.5b (Erickson et al., 2002). In Figure 3.5, P_t is solder bump pitch, W is the clearance between two adjacent solder joints, and d is the solder diameter.

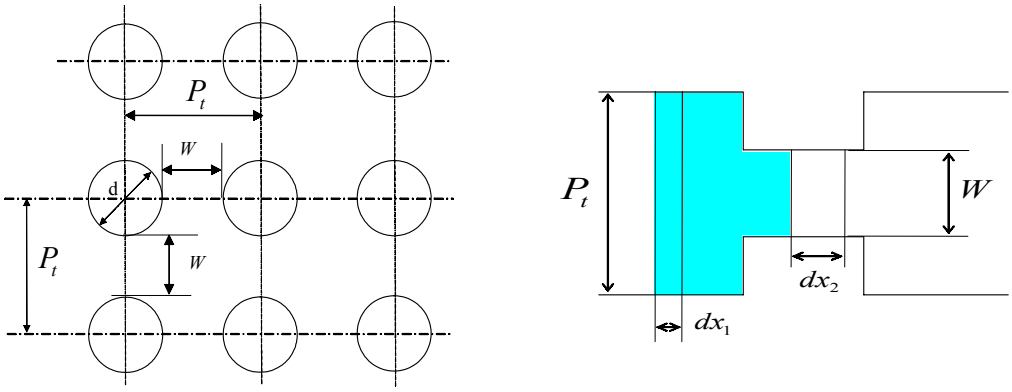

Figure 3.5 Flip-chip package pattern: (a) general structure pattern, (b) generic flow pattern.

The pressure which drives the flow is now the pressure Δp_σ reduced by the pressure loss Δp_j due to the solder bump resistance, i.e.,

$$\Delta p = \Delta p_\sigma - \Delta p_j \tag{3-28}$$

It is noted that in this case Δp_σ is determined by equation (2-28), i.e.,

$$\Delta p_\sigma = 2\sigma \cos\theta \left(\frac{1}{W} + \frac{1}{h} \right) \tag{3-29}$$

where σ is the surface tension coefficient of the fluid in N/m, h the thickness of the cavity, and θ the contact angle.

For the capillary flow shown in Figure 3.5b, the pressure drop, Δp_j, caused by the variation between two cross sections 1 and 2, can be calculated from virtual work principle (Hosokawa et al., 1999). In the control volume of the flow shown in Figure 3.5b, the pressure and capillary force are in equilibrium. By definition, the pressure increment Δp_j is equal to the pressure difference in the equilibrium state. Consider the virtual displacement of the surfaces, dx_1 and dx_2. According to the virtual work principle

$$dU_P = dU_S \tag{3-30}$$

where dU_P is the virtual work done by the pressure, and dU_S is the surface energy change of the control volume. The dU_p is expressed by

$$dU_P = p_1 P_t h_1 dx_1 - p_2 W h_2 dx_2 \tag{3-31}$$

Considering that the flow is incompressible, thus

$$P_t h_1 dx_1 = W h_2 dx_2 \tag{3-32}$$

Substituting equation (3-32) into equation (3-31) gives

$$dU_P = (p_1 - p_2) P_t h_1 dx_1 = \Delta p_j P_t h_1 dx_1 \tag{3-33}$$

The surface energy change in the control volume can be expressed by

$$dU_S = (\sigma_{SG} - \sigma_{SL}) dS \tag{3-34}$$

where σ_{SG} is the solid-gas interface tension, and σ_{SL} is the solid-liquid interface tension, as shown in Figure 2.10. From Young's equation (2-31) (Madou, 2002; Dullien, 1992),

$$\sigma_{SG} - \sigma_{SL} = \sigma_{LG} \cos\theta .$$

The area change caused by the virtual displacement is expressed by

$$dS = 2(W + h_2) dx_2 - 2(P_t + h_1) dx_1 = 2 dx_1 \left[\frac{P_t h_1}{W h_2} (W + h_2) - (P_t + h_1) \right] \tag{3-35}$$

Substituting equations (3-33)-(3-35) into (3-29) gives

$$\Delta p_j = 2\sigma \cos\theta \left[\left(\frac{1}{h_2} + \frac{1}{W} \right) - \left(\frac{1}{h_1} + \frac{1}{P_t} \right) \right] \tag{3-36}$$

When the channel thickness is the same, i.e., $h_1 = h_2$, the above equation reduces to

$$\Delta p_j = 2\sigma \cos\theta \left(\frac{1}{W} - \frac{1}{P_t} \right) \tag{3-37}$$

Given the flip-chip geometry, an underfill flow can be approximated as a combination of a set of flow channels, as shown in Figure 3.4a, in which

$$P_t = W + d \tag{3-38}$$

Substituting equation (3-38) into (3-37) gives

$$\Delta p_j = \frac{2d\sigma \cos\theta}{W(W+d)} \tag{3-39}$$

Substituting equations (3-29) and (3-39) into (3-28) gives

$$\Delta p = \frac{2\sigma \cos\theta (W^2 + hW + dW - dh)}{hW(W+d)} \tag{3-40}$$

3.5 Dynamic Contact Angle

The equations for the dynamics of capillary flow as developed in the above assumed that the rate of wetting or development of an equilibrium contact angle is sufficiently rapid relative to the rate of movement of the liquid. Thus, the contact angle was assumed constant. However, the studies reported by Luo et al. (2000), Gertach et al. (1999), and Schonhorn et al. (1966), showed that the contact angle is time dependent. The measured dynamic contact angle and dynamic viscosity of encapsulant increases with time (Gertach et al., 1999). In the study given by Newman (1968), for horizontal capillary flow, the contact angle can be calculated by the following equation

$$\cos\theta = \cos\theta_e(1 - ae^{-ct}) \tag{3-41}$$

where θ_e is the contact angle at an equilibrium state, a and c are coefficients, which are determined by

$$a = 1 - \frac{\cos\theta_0}{\cos\theta_e} \tag{3-42a}$$

$$c = \frac{\sigma}{\mu M} \tag{3-42b}$$

where θ_0 is the initial contact angle, and M is a constant which depends on the surface in contact with the encapsulant.

3.6 Theoretical Model for the Underfill Flow in Flip-Chip Package

Substituting equations (3-40) and (3-41) into equation (3-21) and neglecting the transient term give

$$\frac{dx_f}{dt} = \frac{2b^2\sigma\cos\theta_e(W^2 + hW + dW - dh)}{3\mu x_f hW(W+d)}\left(1 - ae^{-ct}\right) \tag{3-43}$$

Integration of equation (3-43) leads to

$$x_f^2 = \frac{4b^2\sigma\cos\theta_e(W^2 + hW + dW - dh)}{3\mu hW(W+d)}\left[t + \frac{a}{c}\left(e^{-ct-1}\right)\right] \tag{3-44}$$

The filling time becomes

$$t_f = \frac{3\mu W(W+d)}{h\sigma\cos\theta_e(W^2 + hW + dW - dh)}x^2 + \frac{a}{c}\left(1 - e^{-ct_f}\right) \tag{3-45}$$

Since equation (3-45) is a nonlinear function of filling time t_f, an iterative procedure is needed to evaluate the equation.

3.7 Model Verification

The verification of the theoretical model developed by considering the dynamic contact angle and solder bump resistance is carried out using the experimental results reported by Han and Wang (1997a).

3.7.1 Viscosity

Han and Wang (1997a) measured the viscosity of the encapsulant material Hysol FP4510 from Dexter Corporation, USA. The viscosity was measured at different temperatures, shear rates, and degrees of cure. The measured results were fitted with the Herschel-Bulkley model (see discussion in Chapter 2). The constants K_{00}, C_A, C_B, T_g are given in Table 3.5. When the thickness of the cavity is different from the reference thickness $h_0 = 1.89 \times 10^{-4} m$, the viscosity needs to be corrected using the following correlation

$$\eta = \eta_0 (4.3343 + 0.3888 \ln h) \tag{3-46}$$

where η_0 is the viscosity of non-Newtonian fluid at the reference thickness h_0.

Table 3.5 Constitutive constants (Han and Wang, 1997a)

n	K_{00} (Pa-s^n)	τ_{y0} (Pa)	T_y (K)	T_g (K)	C_1	C_A	C_B (K)
0.916	153.6	0.00138	2148.6	250	3.671	18.44	199.6

3.7.2 Equilibrium Contact Angle and Surface Tension Coefficient

In Han and Wang's measurements, the equilibrium contact angle was fitted to the temperature by a second-order polynomial,

$$\theta = 17.27 + 0.176T - 3.76\times10^{-4}T^2 \tag{3-47}$$

while the surface tension coefficient was fitted to

$$\sigma = 0.1236\exp(-3.8\times10^{-3}T) \tag{3-48}$$

3.7.3 Shear Rate

For steady flow between parallel plates of width B separated by a distance h, the velocity distribution for laminar flow is (Roberson and Crowe, 1997)

$$u = \frac{1}{8\mu}\left(-\frac{dp}{dx}\right)(h^2 - 4y^2) \tag{3-49}$$

The volume flow is

$$Q = 2\int_0^{\frac{h}{2}} uBdy = \frac{Bh^3}{12\mu}\left(-\frac{dp}{dx}\right) \tag{3-50}$$

The wall shear stress is computed from equation (3-49) as follows

$$\tau_w = \left|\mu\frac{du}{dy}\right|_{y=\pm h/2} = \frac{h}{2}\left(-\frac{dp}{dx}\right) \tag{3-51}$$

or

$$-\frac{dp}{dx} = \frac{2\mu}{h}\frac{du}{dy} = \frac{2\mu}{h}\dot{\gamma} \tag{3-52}$$

Substituting equation (3-52) into (3-50) gives

$$Q = \frac{Bh^3}{12\mu}\frac{2\mu}{h}\dot{\gamma} = \frac{Bh^2}{6}\dot{\gamma} \tag{3-53}$$

The volume flow rate can be calculated by

$$Q = \bar{v}hB = \frac{L}{t_f}hB \tag{3-54}$$

where $\bar{v}$ is the average velocity over the whole filling length L, and B is the width of the channel. Substituting equation (3-54) into (3-53) gives

$$\dot{\gamma} = \frac{6L}{ht_f} \tag{3-55}$$

3.7.4 Results and Discussions

The experimental conditions reported by Han and Wang (1997a) were as follows: the length of the chip was 7 mm, the thickness of the cavity was 100 μm, the solder diameter was 160 μm, the clearance between adjacent solder joints was 90 μm, the initial contact angle $\theta_0 = 84.8^o$, and $M = 17.1$. Under these conditions, the filling time was calculated using the proposed analytical model, equation (3-45). The calculation procedure is as follows:

(1) calculate the equilibrium contact angle and surface tension coefficient with equations (3-47) and (3-48), respectively;
(2) assume an initial filling time;
(3) calculate the shear rate with equation (3-55);
(4) calculate the viscosity with equations (2-17)-(2-19);
(5) calculate filling time with equations (3-45); and
(6) use the newly calculated filling time to repeat steps (3) to (5) until the calculation converges for the tolerance $|\Delta t| \le 0.01s$.

Table 3.4 Comparison between measured and theoretical filling time.

Temperature (°C)	80	50	23	23	23
Fraction of volume filled (%)	0.926	0.676	0.25	0.402	0.646
Measured filling time (s) (Han and Wang, 1997a)	60	180	180	600	2700
Filling time calculated with Han-Wang model (s) (Equation 1-6)	46.6	133.6	121.4	330.0	835.1
Filling time calculated with the proposed analytical model (s) (Equation 3-45)	61.5	189.5	187.7	535.4	1502

The theoretical filling time was compared with the measured filling time as well as with the Han-Wang model (Han and Wang, 1997a), and the results are given in Table 3.4. From the results shown, it can be seen that the prediction using the proposed analytical model can match the measured filling times better than that using the Han-Wang model. This confirmed that the flow resistance caused by the solder bump has a significant effect on the underfill flow, and it should not be neglected in the underfill flow analysis in flip-chip packaging. The theoretical result does not match the measured results at 23°C for volume fractions of 0.402% and 0.646%. In these cases, the difference between the experimental and the theoretical results may be caused by the temperature and time dependence of the viscosity. This is because the underfill flow process is to a certain degree coupled with the fluid solidification process. The solidification process will affect the viscosity of the fluid, and such an effect becomes significant with an increase in the filling time (Hsu et al., 2002, He, 2001; He et al., 2000; Han and Wang,

2000b; Karkanas and Partridge, 1996). When the underfill flow is performed at lower temperatures and long filling time, the viscosity may increase significantly with respect to time.

3.8 Conclusions

In this chapter, first, the transient behavior of the flow in the micro-cavities was investigated. Then an equation for calculating the solder resistance in flip-chip underfill was derived. At last, a theoretical model based on the Washburn model with two extensions (dynamic contact angle and solder bump resistance) was developed. From the study reported in this chapter, it is concluded that:

(1) For the small cavity thickness (less than 100 μm) and large fluid viscosity (larger than 0.1 Pa·s), the transient influence on the flow front and the filling time becomes negligible. Therefore, for the underfill flow process in a micro-cavity, the assumption of steady flow for the underfill process is reasonable.

(2) The solder bump resistance has a significant effect on the underfill flow, and it should not be neglected in the underfill flow analysis in flip-chip packaging.

(3) The Han-Wang model is not applicable to the underfill flow process in flip-chip packaging.

(4) The proposed theoretical model which is based on the Washburn model with two extensions (dynamic contact angle and solder bump resistance) performs better than the Han-Wang model.

4 ANALYTICAL MODEL FOR UNDERFILL FLOW

4.1 Introduction

In the preceding chapter, it was shown that the effect of transient behavior on the underfill flow in the context of flip-chip packaging can be ignored. The second study in the preceding chapter attempted to extend the Washburn model by considering the dynamic contact angle for the underfill flow in flip-chip packaging. The result from that study indicated the need for further study; specifically, to implement constitutive equations for non-Newtonian fluids. This is simply because underfill materials demonstrate significant non-Newtonian flow behavior (see discussions in Chapter 2). Furthermore, the goal of retaining an analytical form of the model with a closed-form solution is pursued.

Specifically in this chapter, two lumped parameter analytical models, Model I and Model II, are developed using the power-law constitutive equation for the underfill materials under study. The difference between these models is that Model I is based on parallel plate geometry, while Model II consider a more realistic flip-chip package geometry.

4.2 Model I: The Underfill Flow between Two Parallel Plates

Figure 4.1 (shown earlier Figure 1.8) illustrates the physical setting of an underfill flow as well as the coordinate system. Since the underfill flow driven by capillary action is a very slow one-directional flow process, this analysis assumes that:

(1) the fluid is incompressible with non-Newtonian behavior;

(2) the flow is steady one-directional, two-dimensional laminar flow;

(3) the flow is fully developed at any instant; and

(4) there is no slip between the fluid and solid wall.

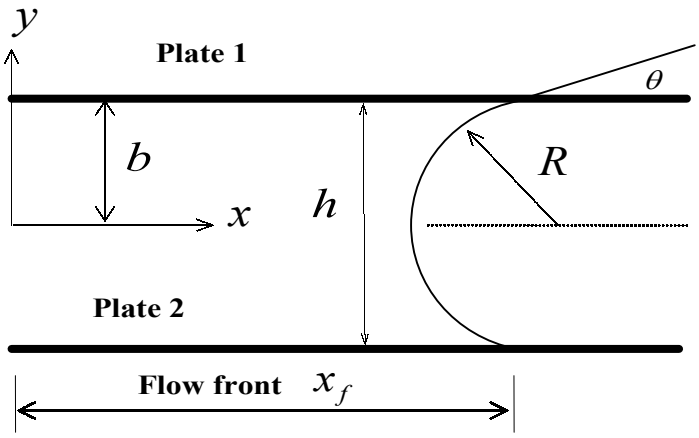

Figure 4.1 Underfill flow between two parallel plates.

Under the above assumptions, $\frac{\partial}{\partial z} = 0$, $\frac{\partial}{\partial t} = 0$, and $w = 0$. From the continuity equation (A-1) in Appendix A, we obtain

$$v = 0 \tag{4-1}$$

Furthermore, from

$$\frac{\partial u}{\partial x} = 0 \tag{4-2}$$

u is function of y only, i.e. $u = u(y)$. From the momentum equations (A-3) to (A-5) in Appendix A and neglecting the gravity, we obtain

$$0 = -\frac{\partial p}{\partial x} - \frac{\partial \tau_{yx}}{\partial y} \tag{4-3}$$

$$0 = -\frac{\partial p}{\partial y} \tag{4-4}$$

From equations (4-3) and (4-4), it is clear that the pressure is only a function of x, i.e. $p = p(x)$.

The power-law model presented in chapter 2 is adopted as the constitutive equation for this problem, i.e.,

$$\tau_{yx} = \eta \frac{\partial u}{\partial y} \tag{4-5}$$

where, η is the viscosity of the non-Newtonian fluid given by

$$\eta = m\dot{\gamma}^{n-1} \tag{4-6}$$

where $\dot{\gamma} = |du/dy|$ is the shear rate, and m and n are constants depending on the temperature. Substituting equation (4-5) into equation (4-2) gives

$$\frac{d}{dy}\left(\eta \frac{du}{dy}\right) = -\frac{dp}{dx} \tag{4-7}$$

It is noted that that the pressure gradient, i.e., the right side of equation (4-7), is a constant. This is because the only possibility for two terms, one related to x and the other related to y, to be equal is that they are both equal to the same constant.

Integrating equation (4-7) subject to the symmetry boundary condition at the center line, i.e., $\left.\frac{du}{dy}\right|_{y=0} = 0$, gives

$$\eta \frac{du}{dy} = \left(-\frac{dp}{dx}\right) y \tag{4-8}$$

Substituting equation (4-6) into (4-8) gives

$$m\left(\frac{du}{dy}\right)^n = \left(-\frac{dp}{dx}\right)y \tag{4-9}$$

Rearranging the above equation gives

$$\frac{du}{dy} = \left(\frac{-dp/dx}{m}\right)^{\frac{1}{n}} y^{\frac{1}{n}} \tag{4-10}$$

Integration of equation (4-10) subject to the no-slip boundary condition, i.e., $u\big|_{y=\pm b} = 0$, gives the gap-wise velocity profile, i.e.,

$$u(y) = \frac{n}{n+1}\left(\frac{-dp/dx}{m}\right)^{\frac{1}{n}}\left(b^{\frac{n+1}{n}} - y^{\frac{n+1}{n}}\right) \tag{4-11}$$

where $b = h/2$, h is the thickness of the cavity gap, and dp/dx is the pressure gradient. The speed of the flow-front is equal to the average gap-wise velocity and is given by

$$\overline{u} = \frac{dx_f}{dt} = \frac{1}{b}\int_0^b u dy \tag{4-12}$$

Substituting equation (4-11) into (4-12) and integrating gives

$$\frac{dx_f}{dt} = \frac{n}{2n+1}\left(\frac{-dp/dx}{m}\right)^{\frac{1}{n}} b^{\frac{n+1}{n}} \tag{4-13}$$

The above equation can be rearranged into

$$\frac{m\left(\frac{dx_f}{dt}\right)^n}{\left(\frac{n}{2n+1}\right)^n b^{n+1}} = -\frac{dp}{dx} \tag{4-14}$$

Since dx_f / dt is independent of x and dp/dx is independent of t, equation (4-14) can be separated into two ordinary differential equations, i.e.,

$$\frac{m\left(\frac{dx_f}{dt}\right)^n}{\left(\frac{n}{2n+1}\right)^n b^{n+1}} = c \tag{4-15}$$

and

$$-\frac{dp}{dx} = c \tag{4-16}$$

Integration of equation (4-16) and applying the boundary conditions, $x = 0$, $p = p_0$, and $x = x_f$, $p = p_f$, leads to

$$p = -\frac{p_0 - p_f}{x_f} x + p_0 = -\frac{\Delta p}{x_f} x + p_0 \tag{4-17}$$

Therefore

$$\frac{dp}{dx} = -\frac{\Delta p}{x_f} \tag{4-18}$$

Substituting equations (4-18) and (4-16) into (4-15) gives

$$\frac{m\left(\frac{dx_f}{dt}\right)^n}{\left(\frac{n}{2n+1}\right)^n b^{n+1}} = \frac{\Delta p}{x_f} \tag{4-19}$$

By integration of the above equation, the flow front and the filling time are given by the following equations, respectively:

$$x_f = \frac{h}{2}\left(\frac{\Delta p}{m}\right)^{\frac{1}{n+1}}\left(\frac{n+1}{2n+1}t\right)^{\frac{n}{n+1}} \tag{4-20}$$

$$t_f = \frac{2n+1}{n+1}\left(\frac{m}{\Delta p}\right)^{\frac{1}{n}}\left(\frac{2x}{h}\right)^{\frac{n+1}{n}} \tag{4-21}$$

where, x_f is the position of the flow-front at time *t* (see Figure 4.1), and t_f is the filling time for a cavity of length *x*. The net driving pressure in this case, Δp, is the net pressure difference due to surface tension, which is calculated using the following equation (Kim et al., 2002; Hau, 2002; Schwiebert and Leong, 1996)

$$\Delta p_\sigma = \frac{\sigma}{R} = \frac{2\sigma\cos\theta}{h} \tag{4-22}$$

where σ is the surface tension coefficient of the fluid in N/m, R is the radius of curvature of the flow-front, and θ is the contact angle (see Figure 4.1). By substituting equation (4-22) into equations (4-20) and (4-21) and rearranging, the flow front and the filling time can be expressed by the following equations, respectively:

$$x_f = \left(\frac{\sigma\cos\theta}{m}\right)^{\frac{1}{n+1}}\left(\frac{(n+1)b}{2n+1}t\right)^{\frac{n}{n+1}} \tag{4-23}$$

$$t_f = \left(\frac{2n+1}{(n+1)b}\right)\left(\frac{m}{\sigma\cos\theta}\right)^{\frac{1}{n}} x^{\frac{n+1}{n}} \tag{4-24}$$

It can be verified that when n = 1, equations (4-23) and (4-24) reduce to equations (1-1) and (1-2), respectively, i.e., the Washburn model in the case of two parallel plates. This gives confidence in the derivation of equations (4-23) and (4-24).

4.3 Model II: The Underfill Flow in Flip-Chip Package

In Model I, the capillary flow was assumed to be between two parallel plates with a uniform section. For an actual flip-chip package, the underfill fluid flows between two parallel plates with a set of solder bumps. The flow resistance caused by the solder bump has significant effect on the underfill flow (see the discussion in Chapter 3), and therefore it cannot be neglected in the underfill flow analysis. To account for the effect of the solder bump, the same set of assumptions as applied with reference to Figure 3.4 is applied here. The net driving pressure in this case should be the net pressure difference due to surface tension reduced by the pressure loss due to the presence of the solder bump, i.e.,

$$\Delta p = \Delta p_{\sigma} - \Delta p_{j} \tag{4-25}$$

where Δp_{j} is the pressure loss due to the presence of the solder bump (i.e., the cross-section variation) and is calculated by the following equation:

$$\Delta p_{j} = \frac{2d\sigma\cos\theta}{W(W+d)} \tag{4-26}$$

Substituting equations (4-22) and (4-26) into (4-25) gives

$$\Delta p = \frac{2\sigma \cos\theta (W^2 + dW - dh)}{hW(W+d)} \tag{4-27}$$

By substituting (4-27) into equation (4-20) and (4-21), the flow front and the filling time in the flip-chip package are given by the following equations, respectively:

$$x_f = \frac{h}{2}\left(\frac{2\sigma \cos\theta (W^2 + dW - dh)}{mhW(W+d)}\right)^{\frac{1}{n+1}}\left(\frac{n+1}{2n+1}t\right)^{\frac{n}{n+1}} \tag{4-28}$$

$$t_f = \frac{2n+1}{n+1}\left(\frac{mhW(W+d)}{2\sigma \cos\theta (W^2 + dW - dh)}\right)^{\frac{1}{n}}\left(\frac{2x}{h}\right)^{\frac{n+1}{n}} \tag{4-29}$$

It can be verified that when $d = 0$, the above equations reduce to equation (4-23) and (4-24), i.e., the flow between two parallel plates, which gives confidence in the derivation of equations (4-28) and (4-29).

4.4 Summary and Discussion

In this chapter, first, a lumped parameter analytical model (Model I) was developed for predicting the underfill flow behavior between two parallel plates driven by capillary action. The power-law constitutive equation was used to describe the non-Newtonian viscous behavior of the underfill material. This model was verified by an experimental study which will be reported in Chapter 5. Furthermore, a lumped parameter analytical

model (Model II) was developed for predicting the flow behavior of underfill flow in the flip-chip package (i.e., two parallel plates with solder bumps) driven by capillary action. The power-law constitutive equation was used to describe the non-Newtonian viscous behavior of the underfill material. This model was also verified by an experimental study which will be reported in Chapter 5.

These two models are presented as closed form solutions to the governing equations; specifically they describe the relation between the underfill flow performance indices (the fluid filling time and the flow front in this case) and the package parameters. This is the result of applying the power-law constitutive equation to the problem in question. It is noted that Model II includes both Model I (by taking the solder diameter to be zero) and the Washburn model (by taking the power-law index $n = 1$ and solder diameter to be zero). It is further noted that the starting point in deriving these two models is essentially different from that adopted by Han and Wang (1997a), since they used the constitutive equation for a Newtonian fluid. Although they considered the contact angle to be time-varying (i.e., the dynamic contact angle), the model for the dynamic contact angle was based on the condition of an open plate with a drop of fluid on it. This condition is different from that of the condition of the flip-chip package, which could be a significant source of error with the models developed by Han and Wang.

5 EXPERIMENTAL STUDY

In this chapter, an experimental study is described, which tests the Washburn model discussed in chapter 1 and the analytical models, i.e., Model I and Model II, developed in chapter 4. In this chapter, Section 5.1 describes the general set-up of the experiment. Section 5.2 presents the validation of the Washburn model. Section 5.3 and section 5.4 present the validation of Model I and Model II, respectively. Conclusions of the experimental studies are presented in section 5.5.

5.1 General Experimental Set-Up

Three experiments were performed to validate the models as described in Chapter 1 and Chapter 4, respectively. The generic part of these experimental setup is shown in Figure 5.1. In Figure 5.1, two pieces of plastic shim stock were placed between the quartz die and the FR4 substrate for the experiment using two parallel plates. The gap width was 9.5 mm, and there were three different gap heights, 45, 85, and 115 μm. For the experiment concerning the flip-chip package, an array of solder bumps was placed between the die and the substrate.

The encapsulant was dispensed along one side of the quartz die with the DS500 precision dispensing system (see Figure 5.2) provided by Assembly Automation Limited, Hong Kong (ASM, 2000). Since the quartz die was transparent, the flow fronts at different times were recorded using a CCD video camera (15 frames/second). The CCD video camera was placed above the die.

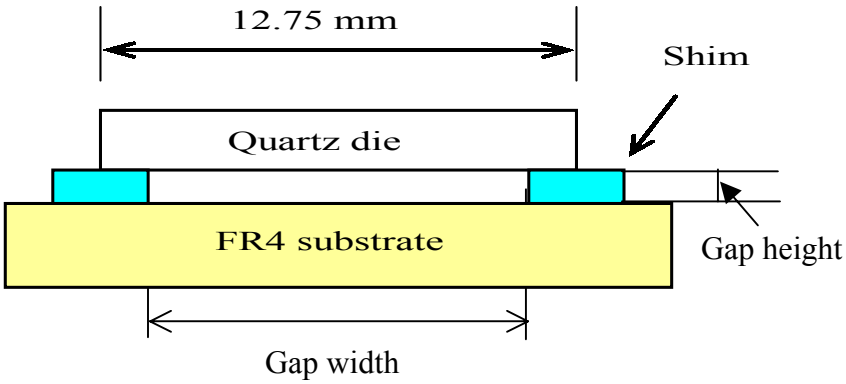

Figure 5.1 Parallel underfill flow test setup.

The material properties (viscosity, surface tension, and contact angle) needed to be measured for the underfill material. Specifically, the surface tension and the contact angle were measured with the DGD-ASE Contact Angle Meter, made by GBX Company, France. The viscosity was measured with a cone-and-plate rheometer, made by the Brookfield Engineering Laboratory, Middleboro, U.S.A. For detailed information about the measurements and determination of the material properties refer to Chapter 2.

Figure 5.2 DS500 precision dispensing system provided by Assembly Automation Limited, Hong Kong (Chen, 2002, reprinted with permission).

5.2 Experimental Verification for the Washburn Model

The purpose of this experiment was to validate the Washburn model. Brookfield 5000 standard fluid, which is a Newtonian fluid used for viscosity calibration, was employed in this study. Its viscosity at 25 °C is 4.83 Pa·s. Three different gap heights (45, 85, and 115 μm) were set up for the experiment. Since the Brookfield 5000 standard fluid flows very slowly at a temperature of 25°C, a stop watch (with resolution 0.01s) was used to measure the time.

The fluid filling times measured at different flow front positions for different gap heights of 45, 85, and 115 μm, are shown in Figures 5.3 to 5.5. Specifically, the results shown in Figure 5.3 are the flow fronts measured at filling times of 177, 411, 720, and 1122s for the gap height of 45 μm. The results shown in Figure 5.4 are the flow fronts measured at the filling times of 81, 212, 342, and 696s for the gap height of 85 μm. The results shown in Figure 5.5 are the flow fronts measured at the filling times of 128, 332, 464, and 576s for the gap height of 115 μm. From these results it can be seen that the flow fronts have a uniform shape.

Figures 5.6 to 5.8 present a comparison between the measured results and the predicted results using the Washburn model. From these figures, it can be seen that the two match very well, which implies that the Washburn model can give a good prediction for the Newtonian fluid flow. The average uncertainty of the measurements is 11.6%. The

uncertainty analysis is given in Appendix B. Note that Figures 5.6 to 5.8 indicate that the filling time decreases with an increase in the gap height.

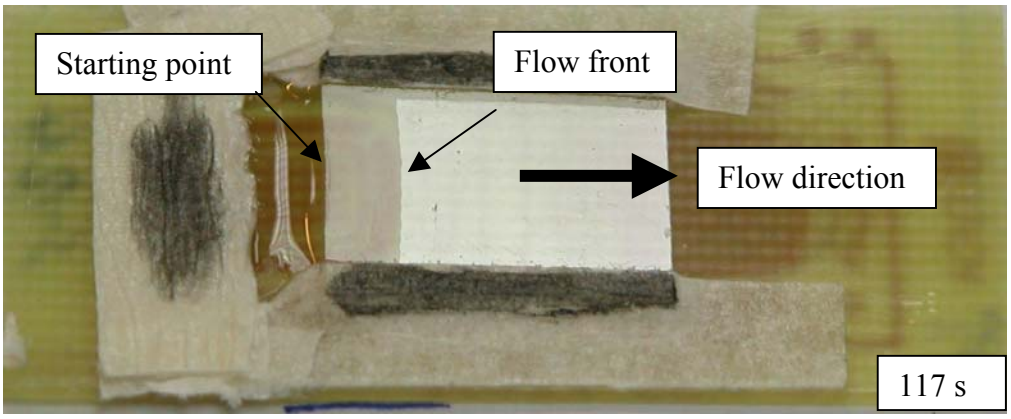

Figure 5.3 (a) Flow front for the filling time 177 s at 25°C with gap height of 45 μm.

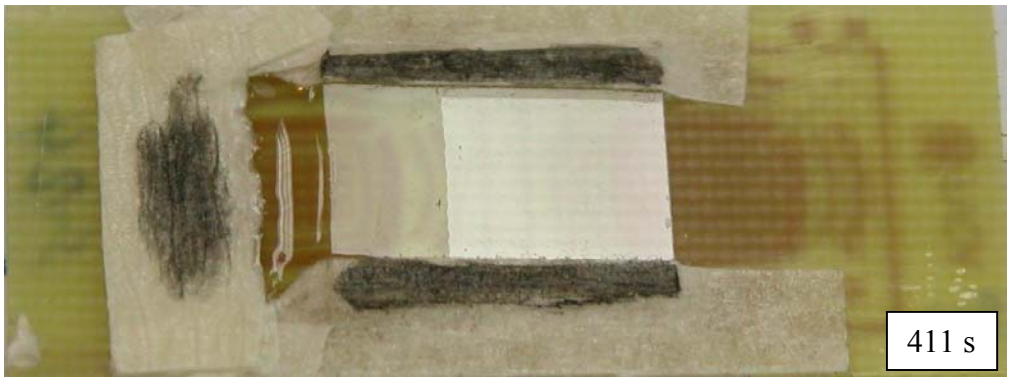

Figure 5.3 (b) Flow front for the filling time 411 s at 25°C with gap height of 45 μm.

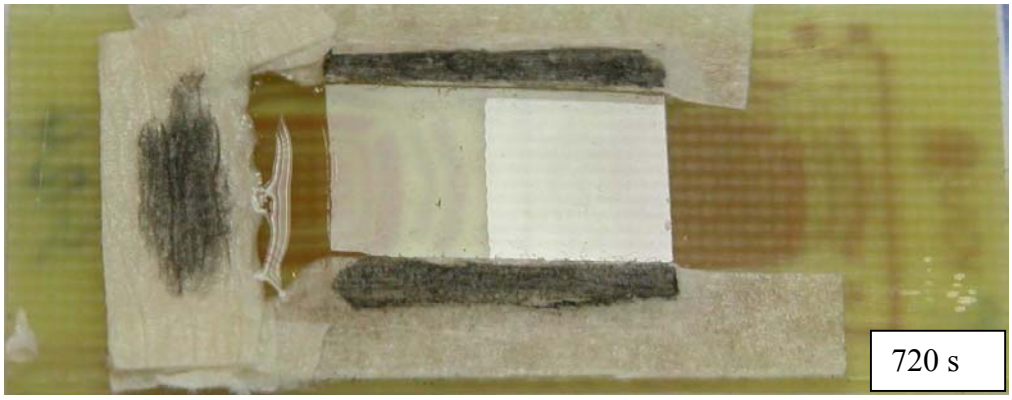

Figure 5.3 (c) Flow front for the filling time 720 s at 25°C with gap height of 45 µm.

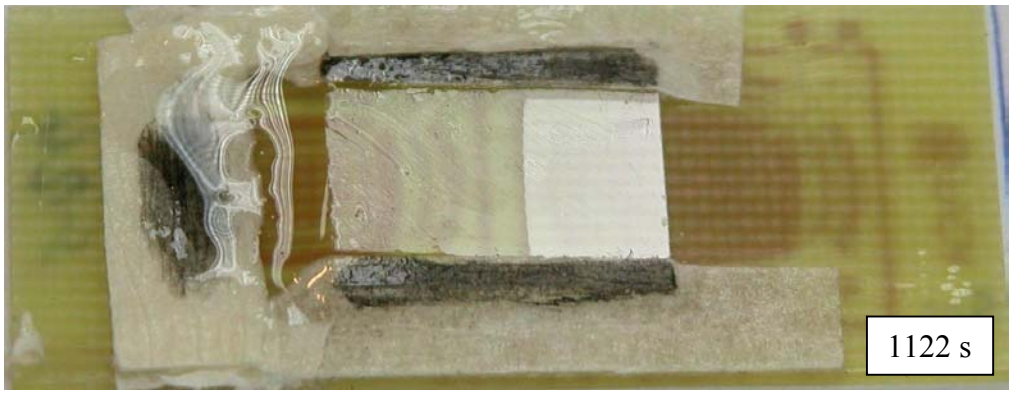

Figure 5.3 (d) Flow front for the filling time 1122 s at 25°C with gap height of 45 µm.

.

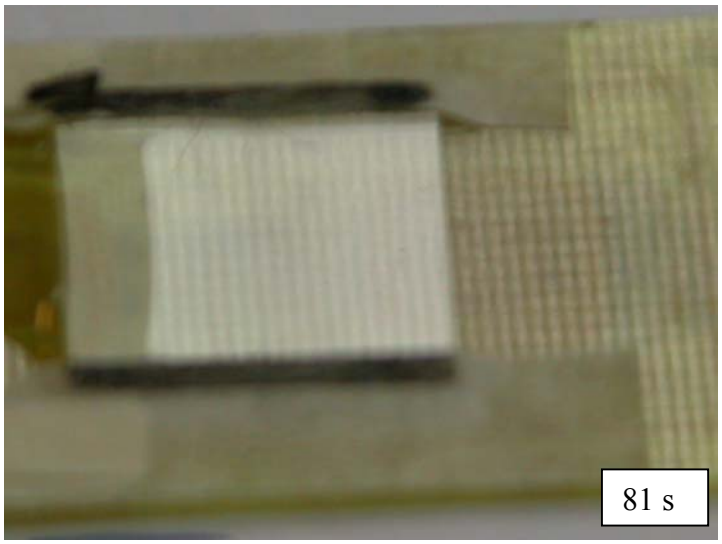

Figure 5.4 (a) Flow front for the filling time 81s at 25°C with gap height of 85 µm.

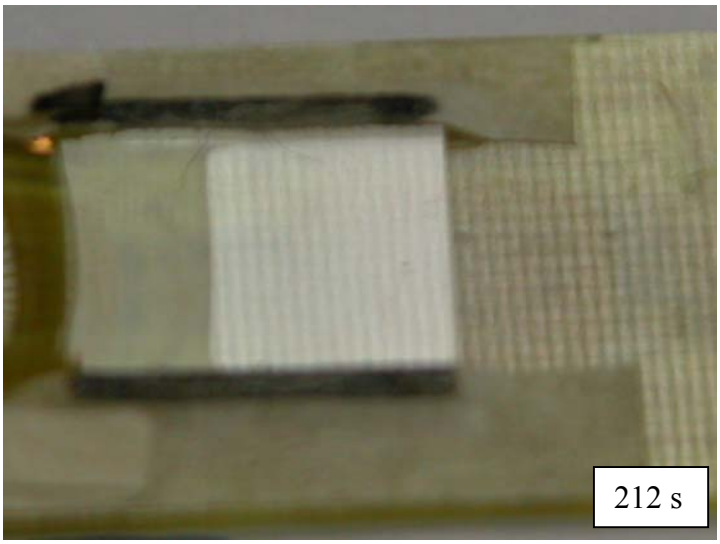

Figure 5.4 (b) Flow front for the filling time 212 s at 25°C with gap height of 85 µm.

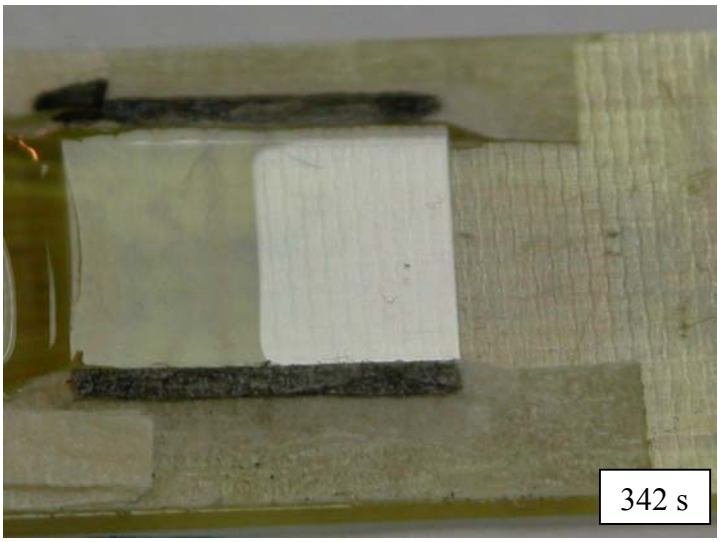

Figure 5.4 (c) Flow front for the filling time 342 s at 25°C with gap height of 85 µm.

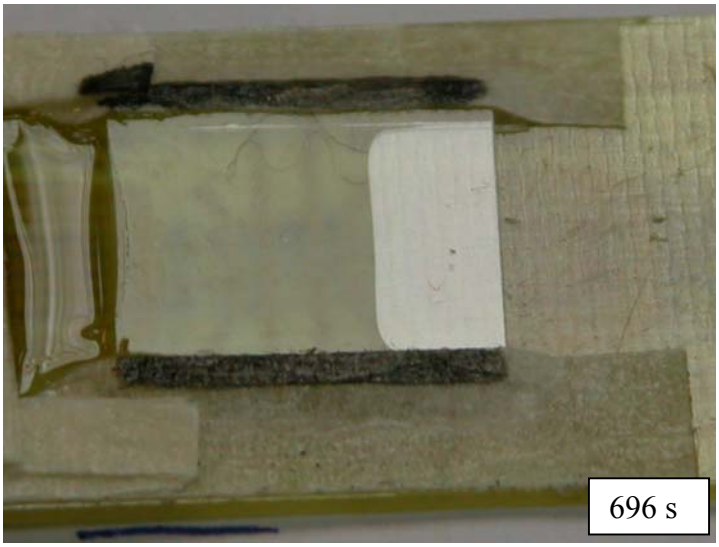

Figure 5.4 (d) Flow front for the filling time 696 s at 25°C with gap height of 85 µm.

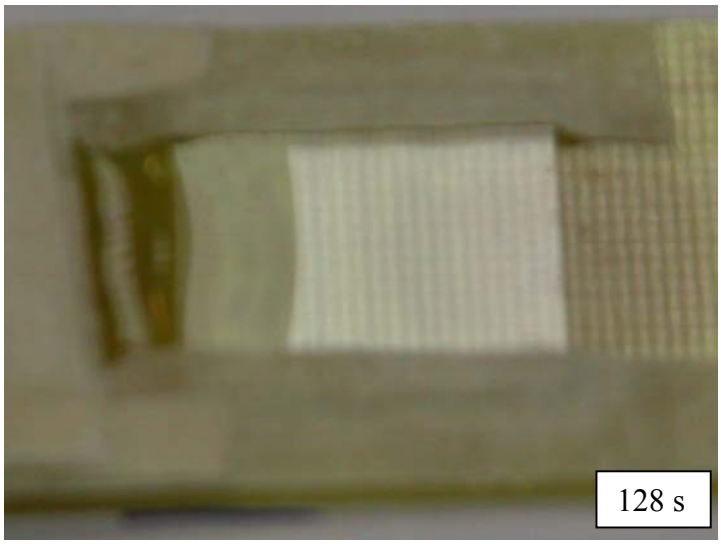

Figure 5.5 (a) Flow front for the filling time 128 s at 25°C with gap height of 115 μm.

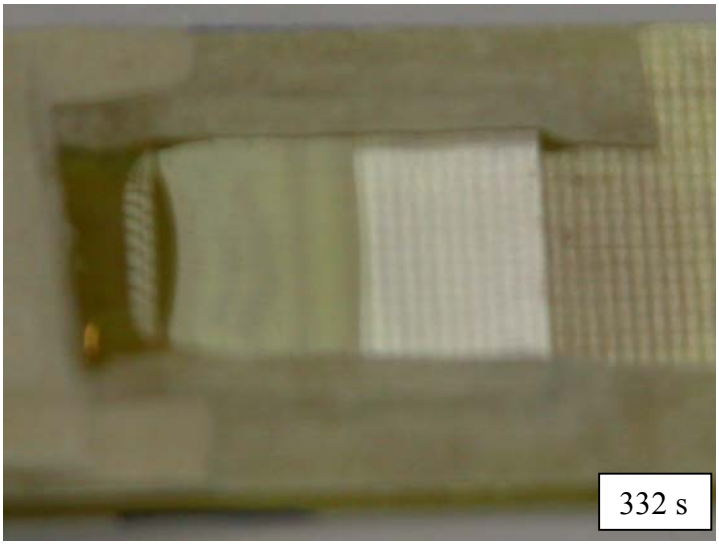

Figure 5.5 (b) Flow front for the filling time 332 s at 25°C with gap height of 115 μm.

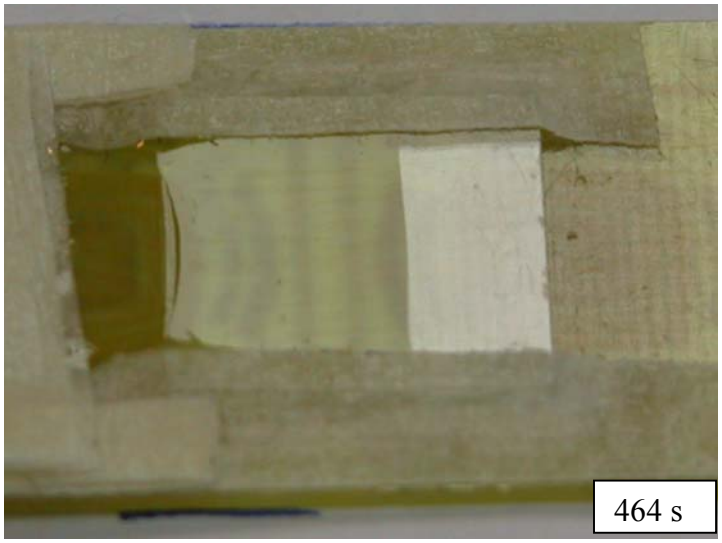

.

Figure 5.5 (c) Flow front for the filling time 464 s at 25°C with gap height of 115 μm.

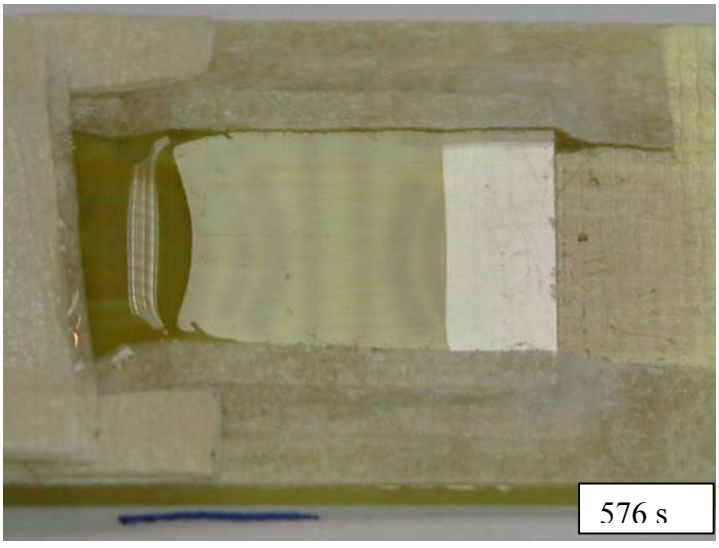

Figure 5.5 (d) Flow front for the filling time 576 s at 25°C with gap height of 115 μm.

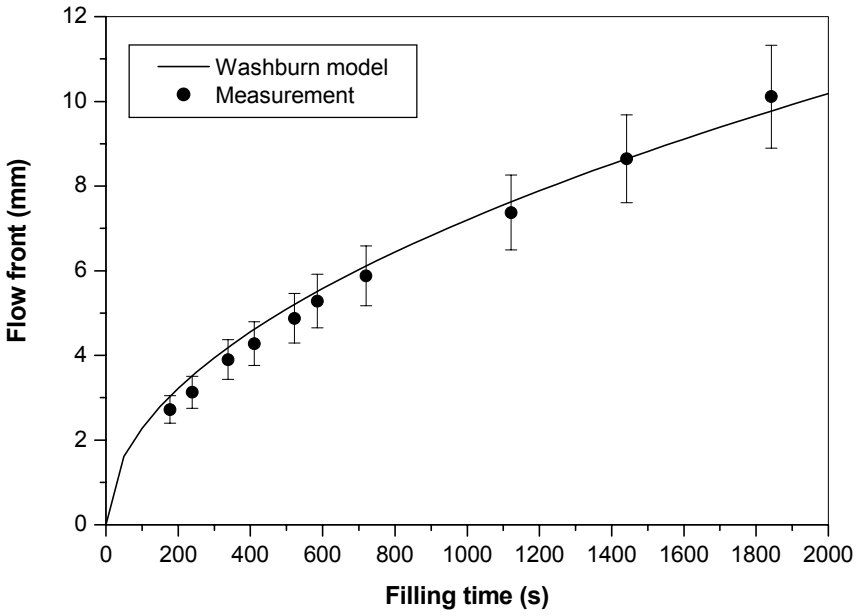

Figure 5.6 Flow front versus filling time at 25°C with a gap height of 45 μm.

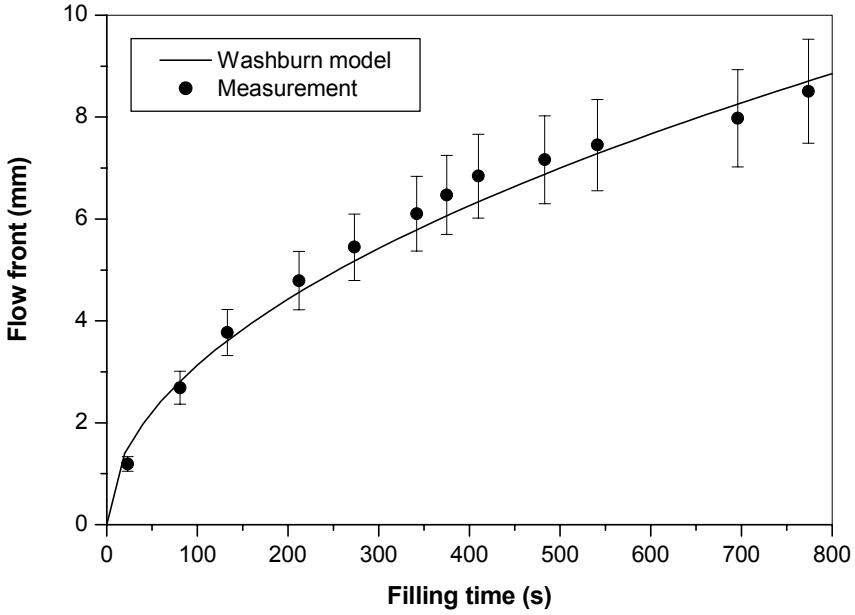

Figure 5.7 Flow front versus filling time at 25°C with a gap height of 85 μm.

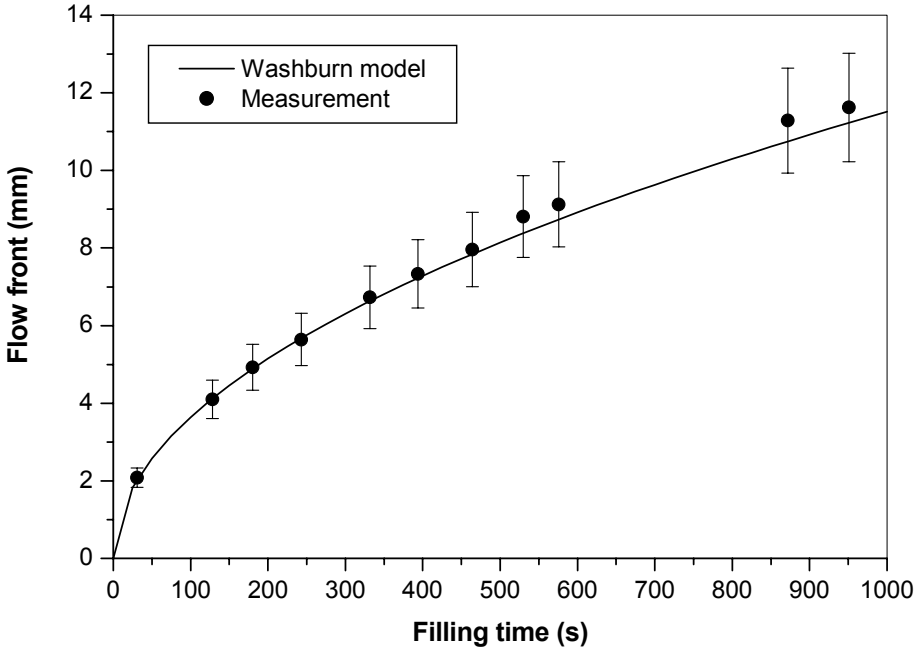

Figure 5.8 Flow front versus filling time at 25°C with gap height of 115 μm.

5.3 Experimental Verification for Model I

5.3.1 Material and Method

The experimental set-up was the same as that described in Figure 5.1. The underfill material used for this experiment was FP4530 made by Dexter Corporation, USA. Three different gap heights (45, 85, and 115 μm) were set. Since the quartz die is transparent, the fluid flow distribution was captured using a CCD video camera. The material properties with their conditions are as follows: (1) parameters *m* and *n* in the power-law

model at a temperature of 60°C were 0.06 Pa · s^n and 1.45, respectively; (2) the contact angle on the FR4 substrate is 28.5°; and (3) the surface tension is 0.011 N/m.

5.3.2 Results and Discussion

Figures 5.9 to 5.11 show the flow fronts measured at filling times of 10, 20, 30, and 50 s for a gap height of 45, 85, and 115 μm, respectively. From these figures, it can be seen that the flow fronts have a uniform shape at filling times of 20, 30 and 40 s but at 10 s; at the time of 10 s, the flow front appears a little slant. This may be caused by the time delay of the dispenser when the dispensing syringe was moving from the top to the bottom. As the filling time increased, the influence of the time delay in the dispenser movement became negligible.

Figures 5.12 to 5.14 and Tables 5.1 to 5.3 show a comparison between the measured results and the predicted results. The prediction calculated using the Washburn model was also plotted in these figures. From these figures and tables, it can be seen that the measured results agree well with the predicted results using Model I, and the predictions of Model I are superior to the Washburn model. It is noted that the average uncertainty of the measurements is 9.21%. A detailed uncertainty analysis is given in Appendix B. Again, from these results, it can be seen that the filling time decreases with an increase in the gap height.

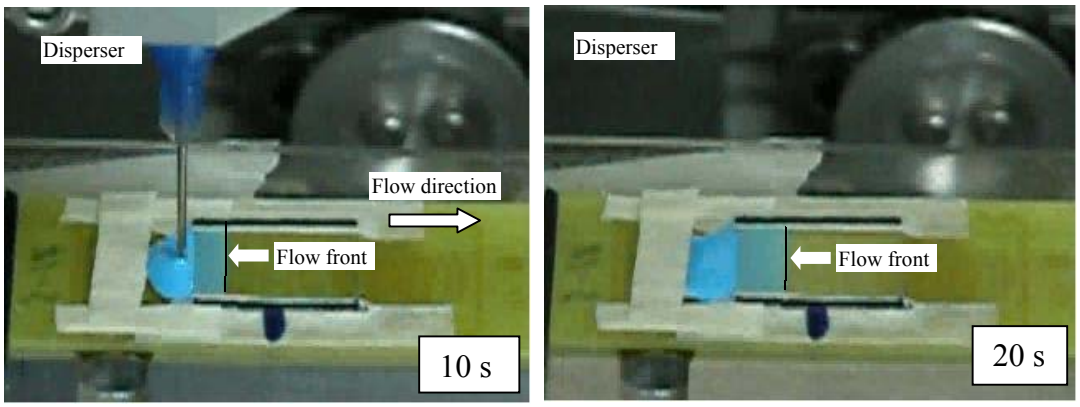

(a) (b)

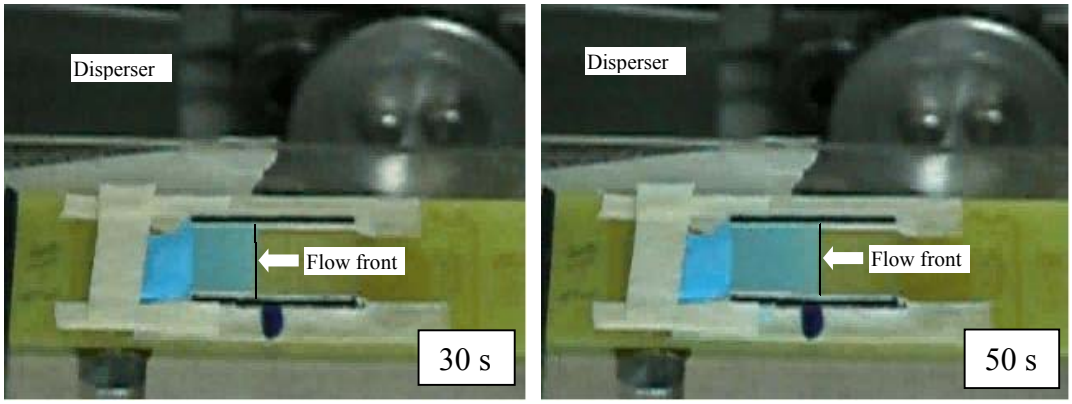

(c) (d)

Figure 5.9 Flow front shapes at filling time 10, 20, 30, and 50 s for a gap height of 45 μm and temperature of 60°C.

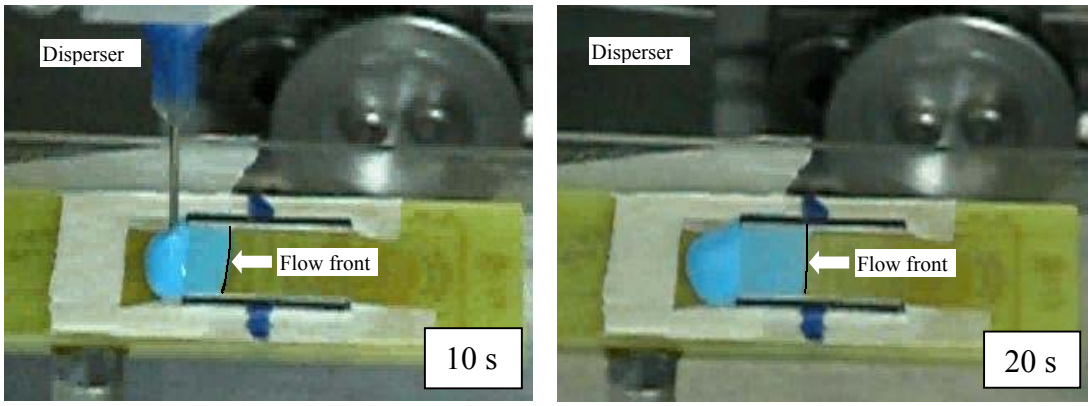

(a) (b)

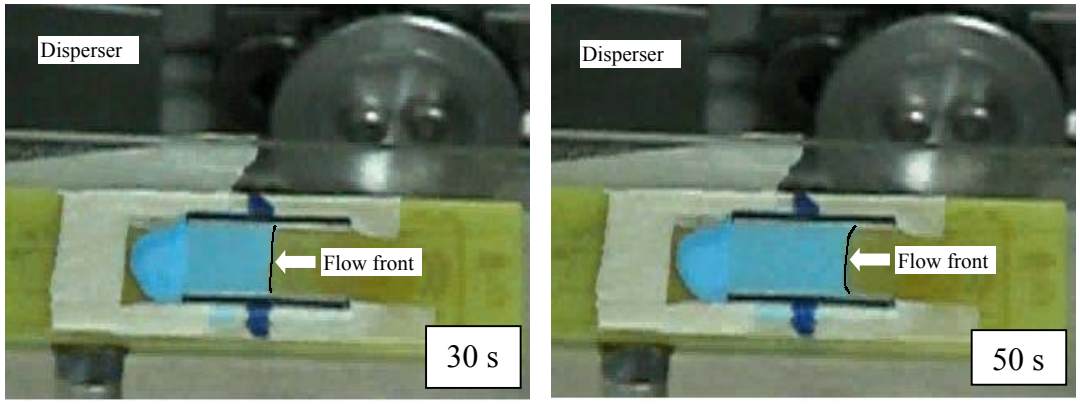

(c) (d)

Figure 5.10 Flow front shapes at filling time 10, 20, 30, and 50 s for a gap height of 85 μm and temperature of 60°C.

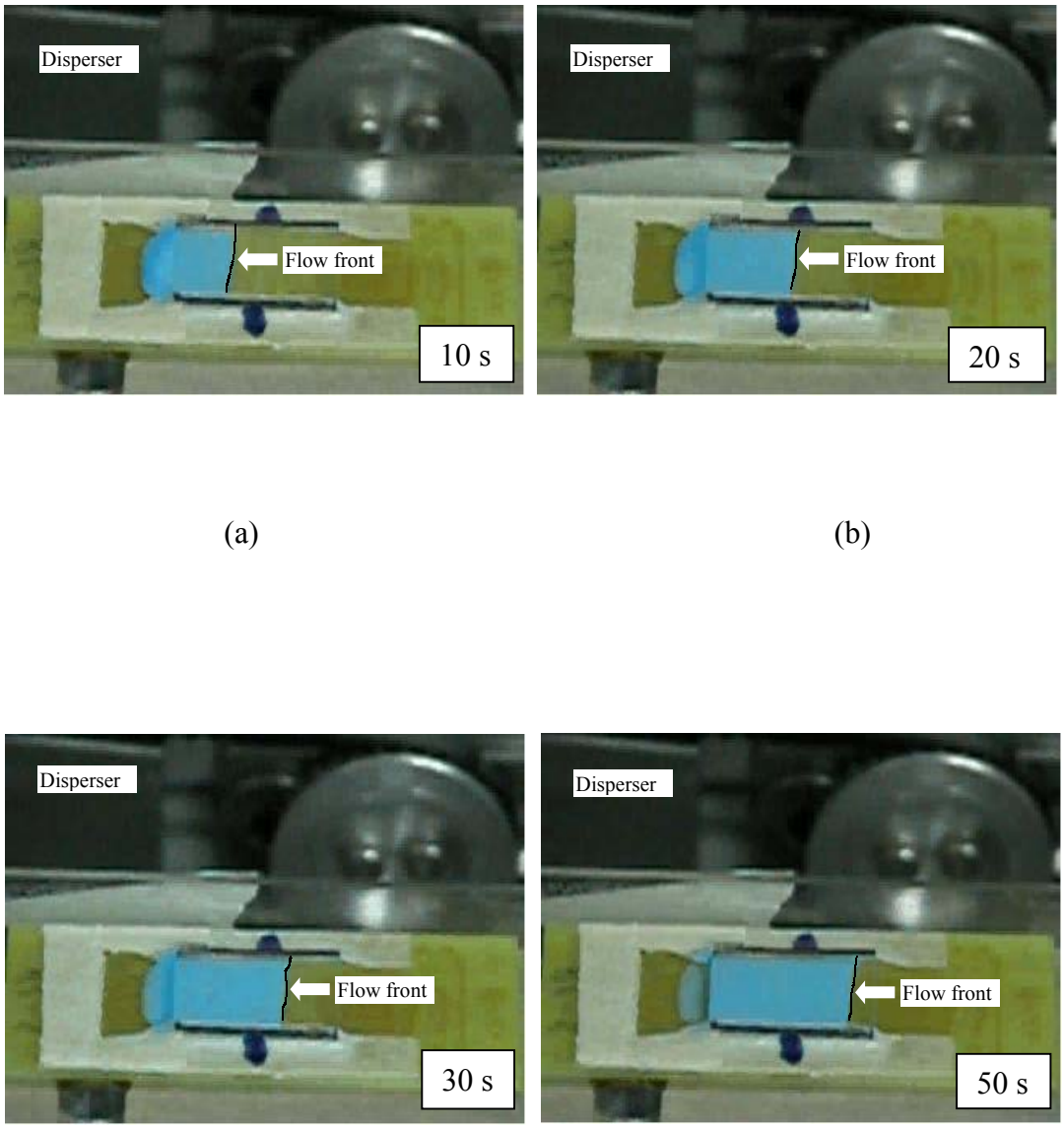

Figure 5.11 Flow front shapes at filling time 10, 20, 30, and 50 s for a gap of height 115 μm and temperature of 60°C.

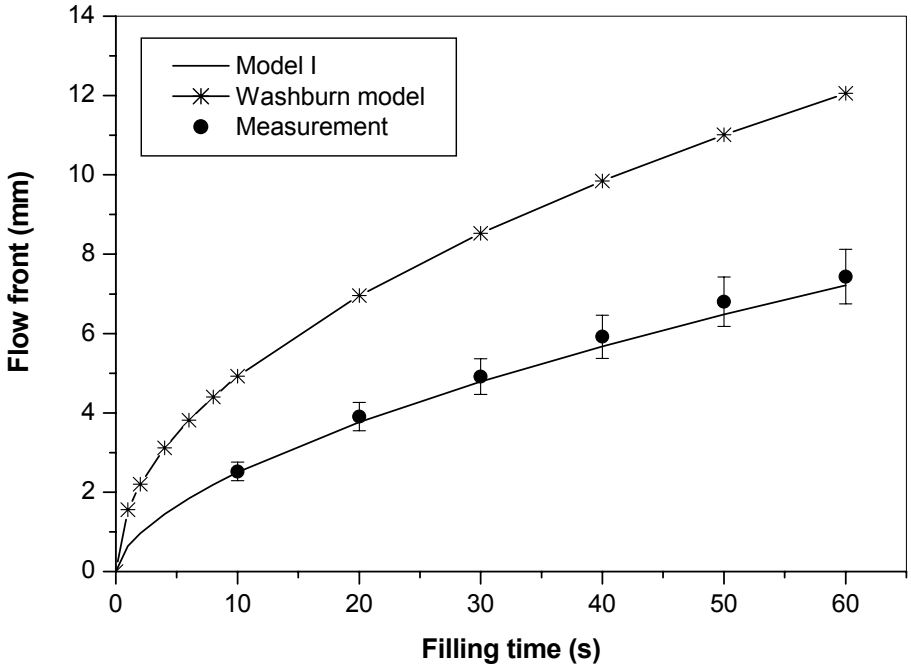

Figure 5.12 Flow front versus filling time at 60°C with a gap height of 45μm.

Table 5.1 Comparison of the flow front predicted by Model I and experiment (gap height: 45μm).

Filling time (s)	Analytical results (mm)	Measured results (mm)	Relative error (%)
10	2.50	2.5	0.1
20	3.77	3.9	3.4
30	4.79	4.9	2.3
40	5.68	5.9	3.8
50	6.48	6.8	4.7
60	7.22	7.4	2.5

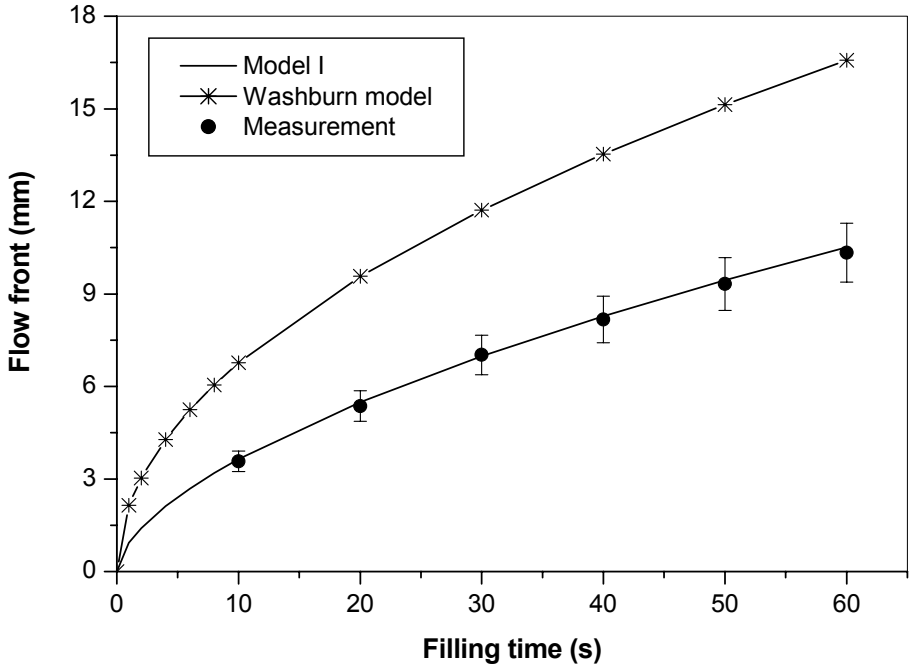

Figure 5.13 Flow front versus filling time at 60°C with a gap height of 85 μm.

Table 5.2 Comparison of the flow front predicted by Model I and experiment (gap height: 85μm).

Filling time (s)	Analytical results (mm)	Measured results (mm)	Relative error (%)
10	3.64	3.5	4.0
20	5.49	5.5	0.2
30	6.98	7.1	1.7
40	8.27	8.5	2.7
50	9.44	9.5	0.6
60	10.52	10.5	0.2

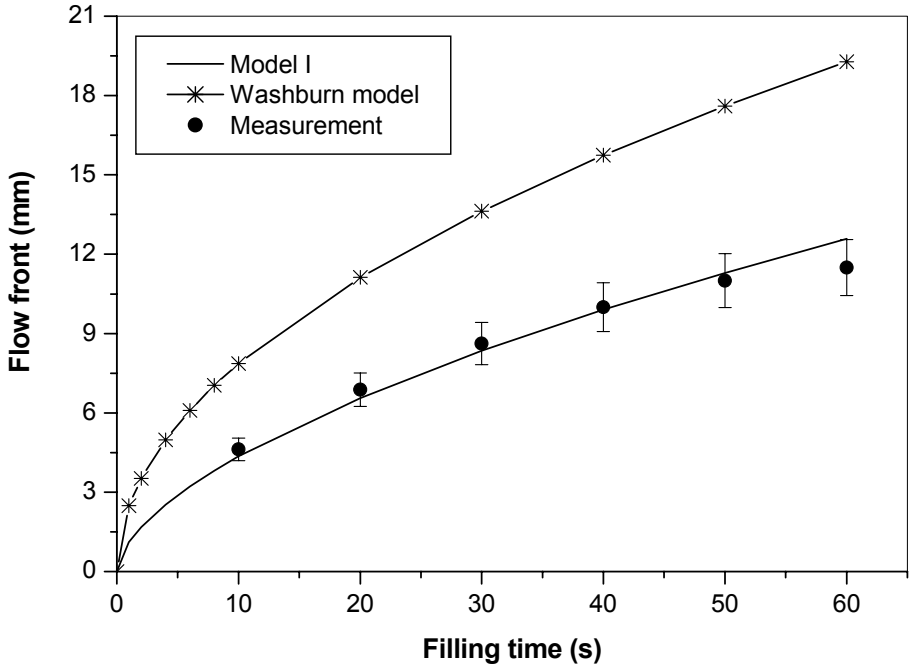

Figure 5.14 Flow front versus filling time at 60°C with a gap height of 115 μm.

Table 5.3 Comparison of the flow front predicted by Model I and experiment (gap height: 115μm).

Filling time (s)	Analytical results (mm)	Measured results (mm)	Relative error (%)
10	4.35	4.6	5.3
20	6.56	6.9	4.9
30	8.35	8.6	3.0
40	9.90	10.0	1.0
50	11.29	11.0	2.7
60	12.58	11.5	9.4

5.4 Experimental Verification for Model II

5.4.1 Material and Method

The underfill material used for this experiment is FP4530. The size of the quartz die was 6 mm x 6 mm, as shown in Figure 5.15. The height of the cavity gap was 50 μm, the solder bump pitch was 250 μm, and the diameter of solder bump was 100 μm. The encapsulant was dispensed along one side of the quartz die. The material properties with their conditions are as follows: (1) parameters *m* and *n* in the power-law model at temperature 60°C were 0.06 Pa · s^n and 1.45, respectively, (2) the contact angle on the FR4 substrate was 28.5°, and (3) the surface tension was 0.011 N/m.

5.4.2 Results and Discussion

Figure 5.16 shows the measured flow fronts at the filling times of 5, 10, 15, 20, 25, and 30 s for the flip-chip underfill flow. From these figures it can be seen that the flow fronts have a uniform distribution except at the time of 5 s. The flow front shape at the filling time of 5 s is a little inclined. This is caused by the time delay of dispenser when the syringe was moving from top to bottom. The influence of the time delay became negligible as filling time increased.

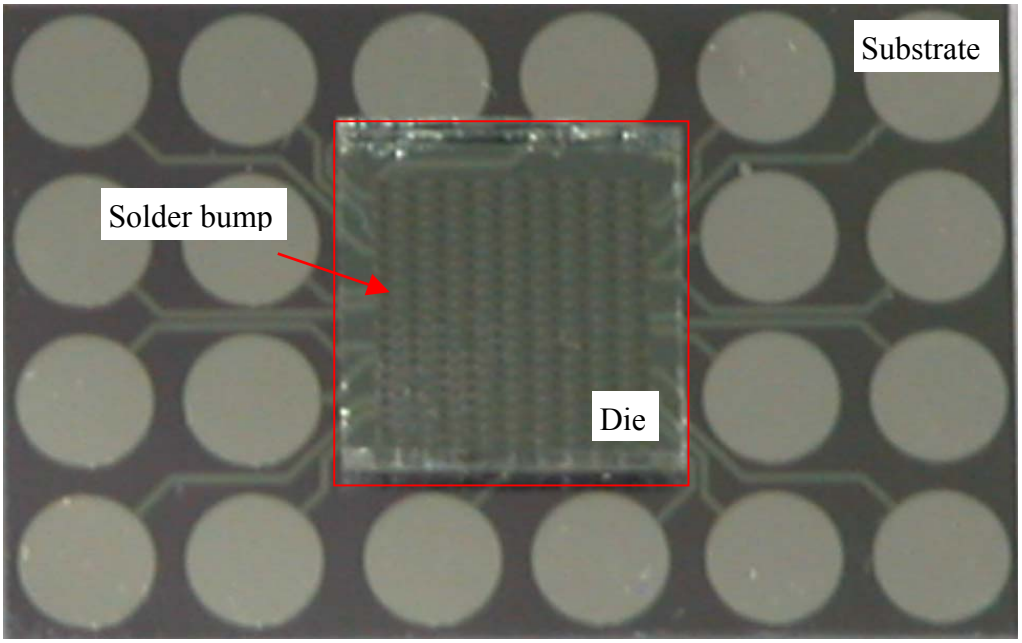

Figure 5.15 Flip-chip experiment set up.

Figure 5.17 and Table 5.4 show a comparison between the measured and predicted results. The prediction calculated from the Washburn model was also plotted in this figure. To make the comparison for the geometry of the flip-chip package, the Washburn model was improved by consideration of the solder bump resistance. In this case, equations (1-1) and (1-2) were rewritten as

$$x_f^2 = \frac{h^2 \Delta p}{6\mu} t \tag{5-1}$$

$$t_f = \frac{6\mu x^2}{\Delta p h^2} \tag{5-2}$$

where the net driving pressure in this case should be the net pressure difference due to the surface tension reduced by the pressure drop due to the presence of the solder bump, which is given by equation (4-27), i.e.,

$$\Delta p = \frac{2\sigma \cos\theta (W^2 + dW - dh)}{hW(W + d)} \tag{5-3}$$

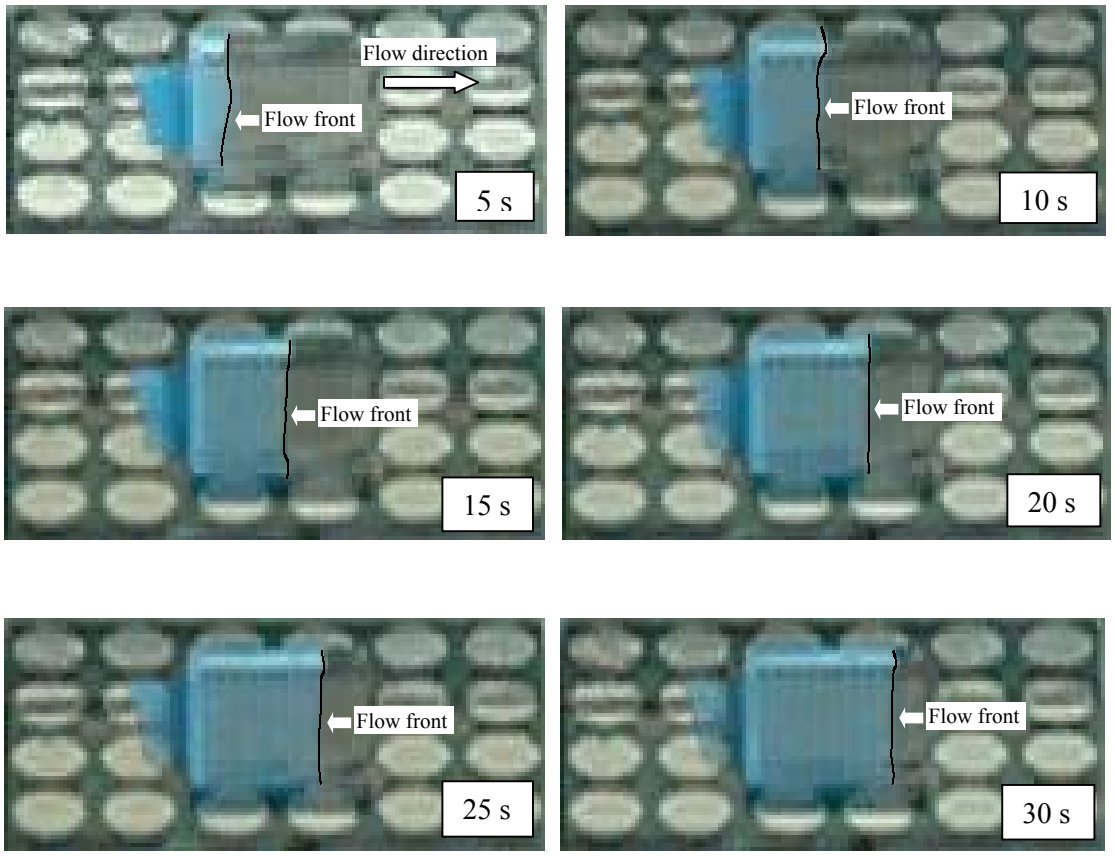

Figure 5.16 Flow front of flip-chip underfill at times of 5, 10, 15, 20, 25, and 30 s.

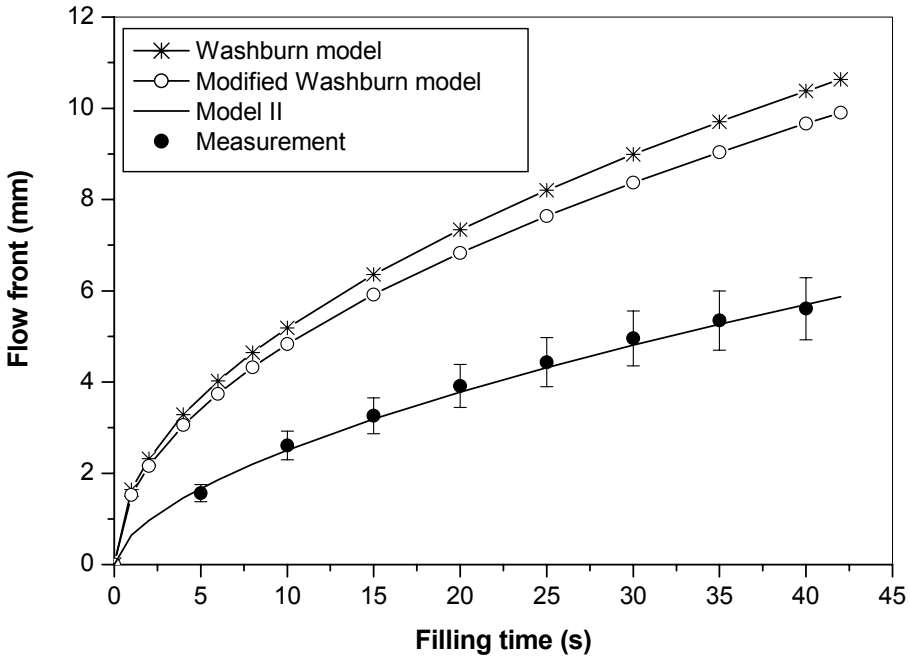

Figure 5.17 Flow front versus filling time for the flip-chip packaging.

Table 5.4 Comparison of the flow front predicted by analytical Model II and experiment for flip-chip packaging.

Filling time (s)	Analytical results (mm)	Exprimental results (mm)	Relative error (%)
5	1.64	1.6	2.8
10	2.51	2.6	3.5
15	3.19	3.3	3.4
20	3.78	3.9	3.0
25	4.32	4.4	1.9
30	4.81	5.0	3.9
35	5.27	5.3	0.6
40	5.70	5.6	1.8

From Figure 5.17 and Table 5.4, it can be seen that the measured results agree well with the results predicted using Model II. The average uncertainty of the measurements is 12.1%. A detailed uncertainty analysis is given in Appendix B. The results show that Model II is better than both the Washburn model and the modified Washburn model. The improved Washburn model does not significantly improve the Washburn model. It is speculated that the Washburn model is inherently deficient for representing the flow behavior of a non-Newtonian fluid in the flip-chip packaging setting. This observation can lead to another result, that is, under the experimental condition, the influence of the solder bump on the filling time and the flow front position is much less than that of the fluid properties. A further discussion regarding this observation will be presented in Chapter 7.

5.5 Conclusions

In this chapter, experiments were implemented to test the Washburn model and the two new models (Model I and Model II). From this experimental investigation, it can be concluded that:

1. The Washburn model can give a good prediction for the Newtonian fluid in the parallel-plate underfill flow, but is not applicable for non-Newtonian fluids.

2. Model I is much better than the Washburn model for predicting the capillary underfill flow between two parallel plates for a non-Newtonian fluid. The fluid filling time calculated using Model I agrees well with the measured result. Model I was shown to be excellent for describing the non-Newtonian underfill flow for the geometry of two parallel plates.

3. Model II is much better than the Washburn model or the improved Washburn model for predicting the capillary underfill flow in flip-chip packaging. The fluid filling time calculated using Model II agrees well with the measured result. Model II was shown to be excellent for describing the non-Newtonian underfill flow for the geometry of the flip-chip package.

6 NUMERICAL MODELING FOR UNDERFILL FLOW

6.1 Introduction

In Chapter 4, two lumped parameter analytical models were developed to investigate the characterization of the underfill flow process. Since these analytical models were developed for a one-directional, two-dimensional assumption, they are inadequate for investigation of the flow front distribution in a two-directional, two-dimensional field affected by the solder bump patterns, including the bump pitch, the bump diameter, and the gap height. The objective of the study presented in this chapter was to develop a numerical model to investigate the flow front distribution for two-directional, two-dimensional flow, as well as the "racing effect" reported by Nguyen et al. (1999) in the flip-chip underfill flow process, which was believed to be induced by the "wicking effect" of the edges. The understanding obtained from this study will help to further optimize the package design.

In this chapter, a two-dimensional numerical model for underfill flow was implemented using the ANSYS software package (Version 7.0). In this numerical analysis, the finite element method (FEM) was used to discretize the fluid flow equations, and the volume

of fluid (VOF) technique was used to track the flow front. The power-law model was applied for the constitutive relation of the non-Newtonian fluid behaviour.

6.2 Finite Element Model Development for Underfill Flow

The finite element method is a numerical technique. It gives approximate solutions to a differential equation, which models problems arising in physics and engineering. The basic idea of the finite element method is to use a set of "simple" elements to simulate a real physical entity. On each element, the unknown variables are approximated using known functions. These functions can be linear or higher-order polynomial expansions. The governing equations are integrated over each element and the solution assembled over an entire problem domain. A set of linear equations is obtained in terms of a set of unknown parameters over each element and solved using linear algebra techniques. A detailed introduction can be found in the literature, such as Reddy and Garting (2001); Reddy (1993); and Pepper and Heinrich (1992).

To complete a finite element model, one needs to specify: (1) the governing equation, (2) the boundary conditions, (3) the fluid material properties, (4) the type of element, and (5) the mesh (i.e., a set of elements that "cover" the problem domain). There are two ways to develop a model with ANSYS. One way is through the graphical user interface, and the other way is through codes written by the modeller. The first way will only work for a relatively simple problem. In this study, the second way was adopted.

Step 1: Define element type

The ANSYS FLOTRAN elements, FLUID141 and FLUID142, were used to solve for two- and three-dimensional flow, pressure, and temperature distributions in a single phase viscous fluid, respectively. For these elements, the ANSYS program calculates velocity components, pressure, and temperature from the conservation of mass, momentum, and energy. Note that in the study presented in this thesis, the volume of fluid (VOF) technique was used to track the flow front (a discussion about VOF is given later). Currently, the VOF capability in ANSYS software package is available only for quadrilateral elements for two-dimensional planar or axis-symmetrical analyses. Therefore, in this study, the quadrilateral element, named FLUID141 in the ANSYS package, was used. Table 6.1 lists the main properties of this element.

Table 6.1 Two-dimensional element.

Element	Dimension	Shape or Characteristic	Degrees of freedom
FLUID141	2-D	Quadrilateral, four nodes	Fluid velocity, pressure, temperature, volume fraction

Step 2: Create mesh

For a flip-chip package, there are solder bumps between the substrate and the chip. A square shape was used to represent the solder bump cross section. A typical meshed

geometric model for a full array of the flip-chip underfill flow is shown in Figure 6.1, in which the dimension of the die of the chip is 6.7 mm x 6.7 mm, the solder bump pitch is 250 μm, the bump width is 168 μm, and the number of solder bumps is 25 x 25. In the simulation code developed, the DO-loops structure was used to create the area of fluid flow. The ANSYS command AESIZE is used to create the quadrilateral mesh. The quadrilateral finite element mesh was used to implement the VOF technique to calculate the flow front position.

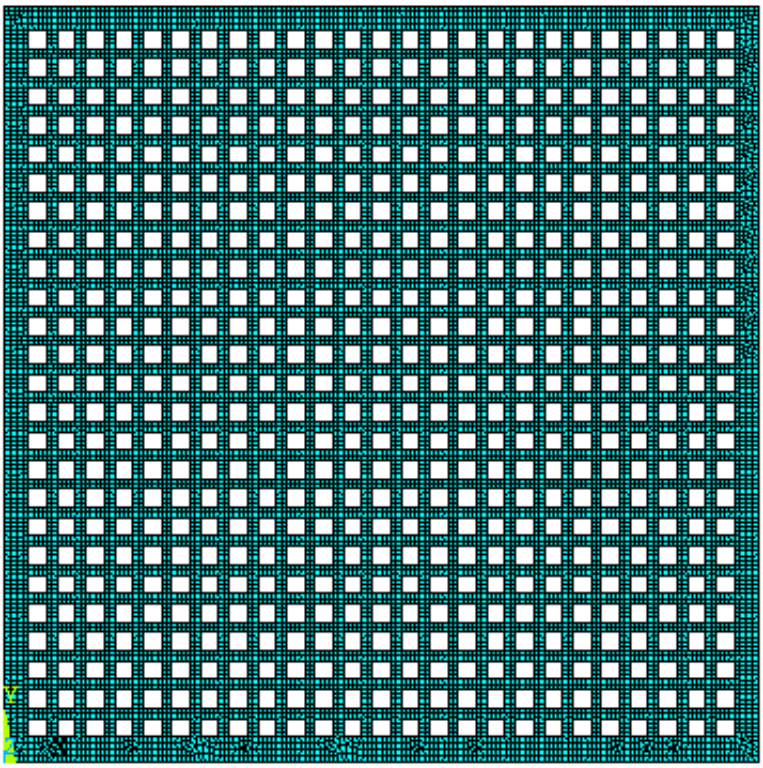

Figure 6.1 The meshed geometric model for a full array flip-chip underfill flow.

Step 3: Define boundary conditions

For an underfill flow driven by capillary action, the boundary conditions are shown in Figure 6.2. At the inlet:

$$p = p_{atm} \tag{6-1}$$

At the flow front:

$$p = p_{atm} - \Delta p_{\sigma} \tag{6-2}$$

where, p_{atm} is the atmospheric pressure and Δp_{σ} is the pressure change due to surface tension.

On the other solid walls or symmetric boundaries:

$$V_n = 0 \tag{6-3}$$

where, V_n is the velocity in the normal direction to the solid wall or symmetry axis.

In this study, the pressure boundary condition at the inlet was converted into a time-dependent velocity function in order to consider the flow resistance caused by the

parallel plates in the gap-wise direction. From the study presented in Chapter 4, the flow front position in the underfill flow is given by the following equation:

$$x_f = \frac{h}{2}\left(\frac{\Delta p}{m}\right)^{\frac{1}{n+1}}\left(\frac{n+1}{2n+1}t\right)^{\frac{n}{n+1}} \tag{6-4}$$

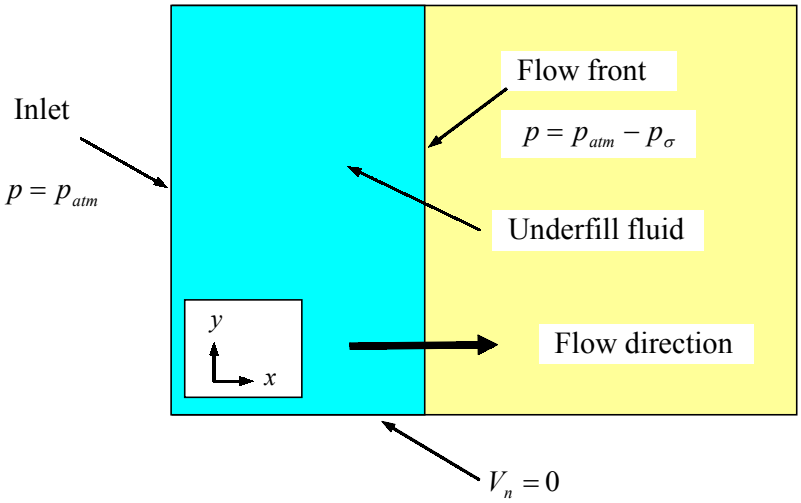

Figure 6.2 Boundary conditions of the underfill flow driven by surface tension.

By differentiating equation (6-4) with respect to time, the velocity is obtained as

$$u = \frac{nh}{2(n+1)}\left(\frac{\Delta p}{m}\right)^{\frac{1}{n+1}}\left(\frac{n+1}{2n+1}\right)^{\frac{n}{n+1}} t^{-\frac{1}{n+1}} \tag{6-5}$$

where as before, u is the velocity, t is the filling time, h is the gap height, m and n are the consistency coefficient and flow behaviour index of power-law viscosity equation,

respectively, and Δp is the driving pressure. For the underfill flow between two parallel plates, Δp is calculated with the following equation (see the discussion in Chapter 4):

$$\Delta p = \frac{2\sigma \cos\theta}{h} \tag{6-4}$$

For the flip-chip underfill flow simulation (see the discussion in Chapter 4)

$$\Delta p = \frac{2\sigma \cos\theta (W^2 + dW - dh)}{hW(W + d)} \tag{6-5}$$

For a VOF analysis, it should be noted that when creating the finite element mesh, at least two boundary nodes are required for every element located at the inlet/outlet boundary.

Step 4: Establish fluid properties

Fluid properties include the density, thermal conductivity, specific heat, and viscosity. ANSYS provides three kinds of non-Newtonian fluid viscosity: power-law model, Carreau model, and Bingham model. The power-law model in ANSYS was used in this study. In ANSYS, this model is activated by command FLDATA7. The four coefficients associated with the power-law model are specified by the commands FLDATA8 to FLDATA11.

Step 5: Select solution method

Solution options are set by the ANSYS command FLDATA1. For the underfill flow analysis using the VOF technique, the VOF algorithm is activated with the ANSYS command FLDATA1. The volume of fluid (VOF) method determines the shape and location of the free surface based on the concept of a fractional volume of fluid. A unity value of the volume fraction (VFRC) corresponds to a full element occupied by the liquid, and a zero value indicates an empty element containing no fluid (or gas). A VFRC value between zero and one indicates that the corresponding element is partially filled (called a partial element). In general, the evolution of free surface is computed through the following equation:

$$\frac{\partial F}{\partial t} + u\frac{\partial F}{\partial x} + v\frac{\partial F}{\partial y} = 0 \tag{6-6}$$

where F is defined as volume fraction (or VFRC). This equation states that F moves with the fluid. The average value of F in a cell would then represent the fractional volume of the cell occupied by fluid. In particular, a unit value of F would correspond to a cell full of fluid, while a zero value would indicate that the cell contained no fluid. Cells with F values between zero and one must then contain a free surface. In ANSYS, an algorithm called Computational Lagrangian-Eulerian Advection Remap (CLEAR) is used to track the evolution of the free surface with time. A detailed description on the

CLEAR advection algorithm can be found in the CFD Guide in the ANSYS software package (Pantuso et al., 2003, Hirt and Nichols, 1981).

6.3 Model Verification

6.3.1 The Underfill Flow between Two Parallel Plates

Before using the numerical model for simulation, experimental results were used to verify this model. The simulation results were based on the following conditions: the plane dimension of the die was 12.75 mm x 9.5 mm, the average gap height between the chip and the substrate was 45, 85, and 115 μm. The power-law index m and n were 0.06 $Pa \cdot s^n$ and 1.45, respectively. The contact angle on the FR4 substrate was 28.58, the surface tension was 0.011 N/m, and the density of the underfill fluid was 1800 kg/m^3.

The simulation results are shown in Figure 6.3, together with the experimental results for comparison. Figure 6.4 gives a comparison of the simulated flow front with the analytical and experimental results. The relative errors of both the numerical simulation and analytical calculation with Model I are listed in Table 6.2. From these results it can be seen that the numerical simulation results can predict very well for the underfill flow between two parallel plates in terms of both the filling time and the flow front distribution. Similar results are shown in Figures 6.5 and 6.6, and Table 6.3 for a gap height of 85 μm, and in Figures 6.7 and 6.8, and Table 6.4 for a gap height of 115 μm.

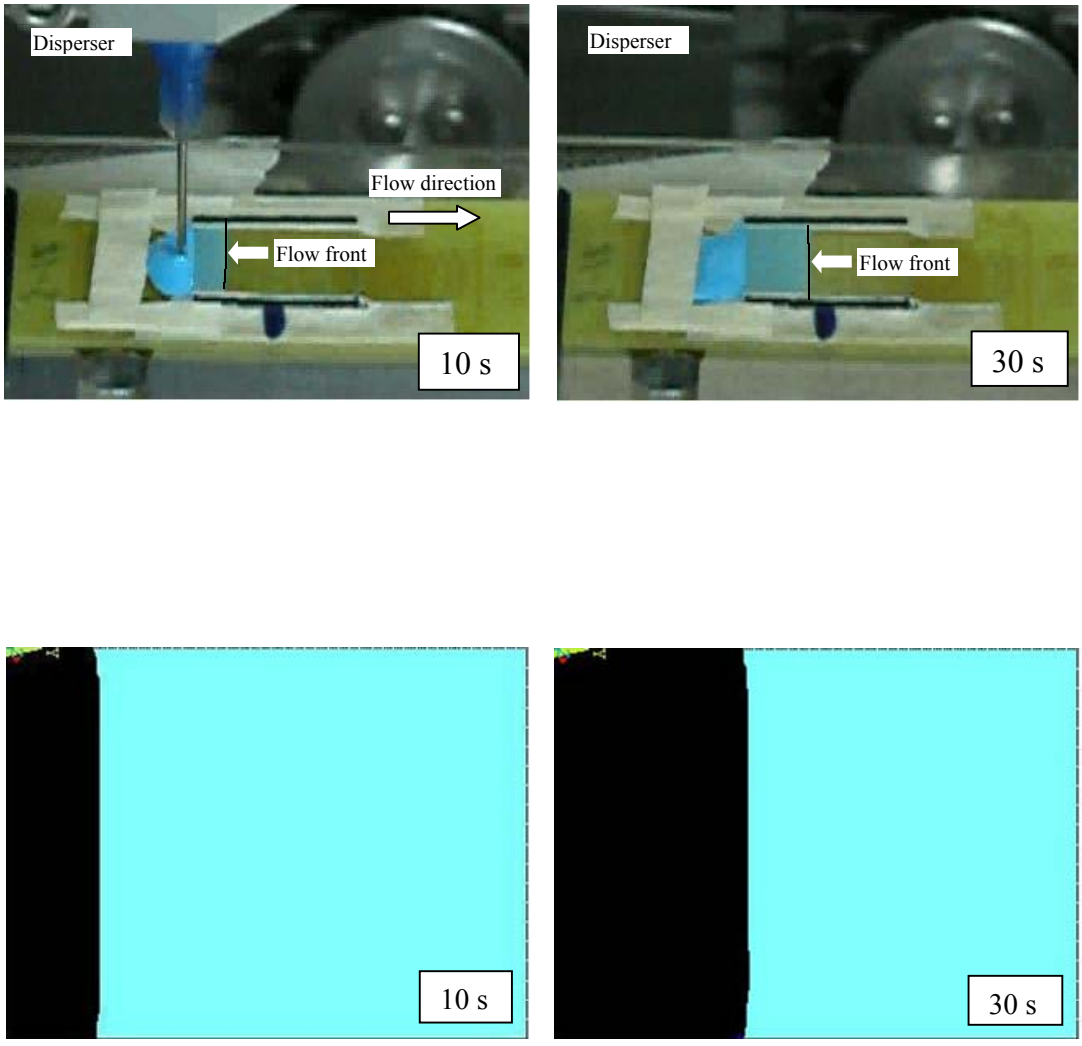

Figure 6.3 Simulated flow front (bottom) compared to measured flow front (top) at filling times of 10 and 30 s and a gap height of 45 µm.

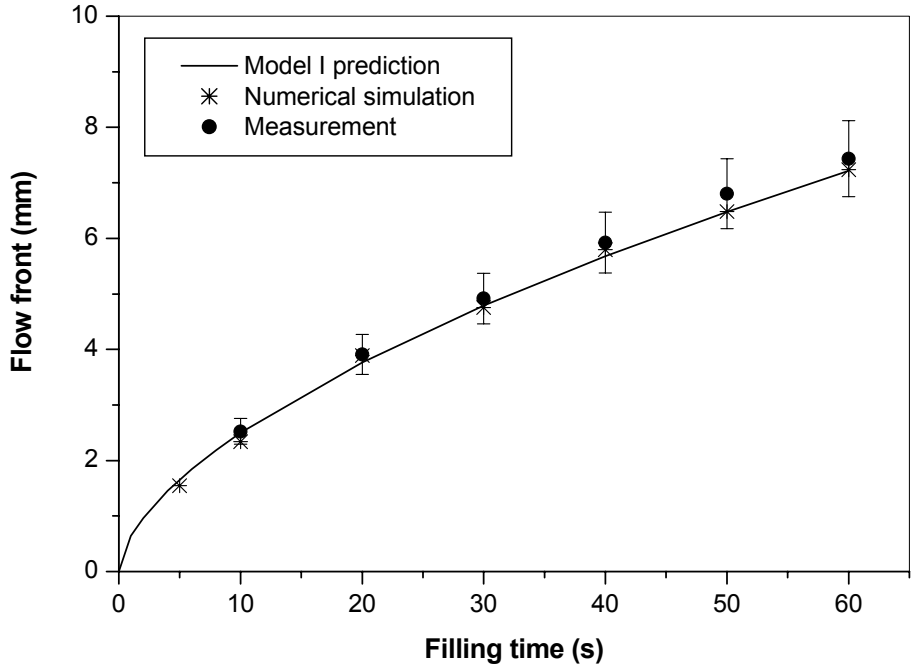

Figure 6.4 Comparison of the simulated flow front with the analytical and experimental results at a gap height of 45μm.

Table 6.2 Comparison of the simulated flow front with the analytical and experimental results at a gap height of 45μm

Filling time (s)	Simulated results (mm)	Analytical prediction (mm)	Measured results (mm)	Relative error using simulation (%)	Relative error using analytical model (%)
10	2.3	2.50	2.5	8.0	0.1
20	3.9	3.77	3.9	0.0	3.4
30	4.8	4.79	4.9	2.0	2.3
40	5.8	5.68	5.9	1.7	3.8
50	6.5	6.48	6.8	4.4	4.7
60	7.2	7.22	7.4	2.7	2.5

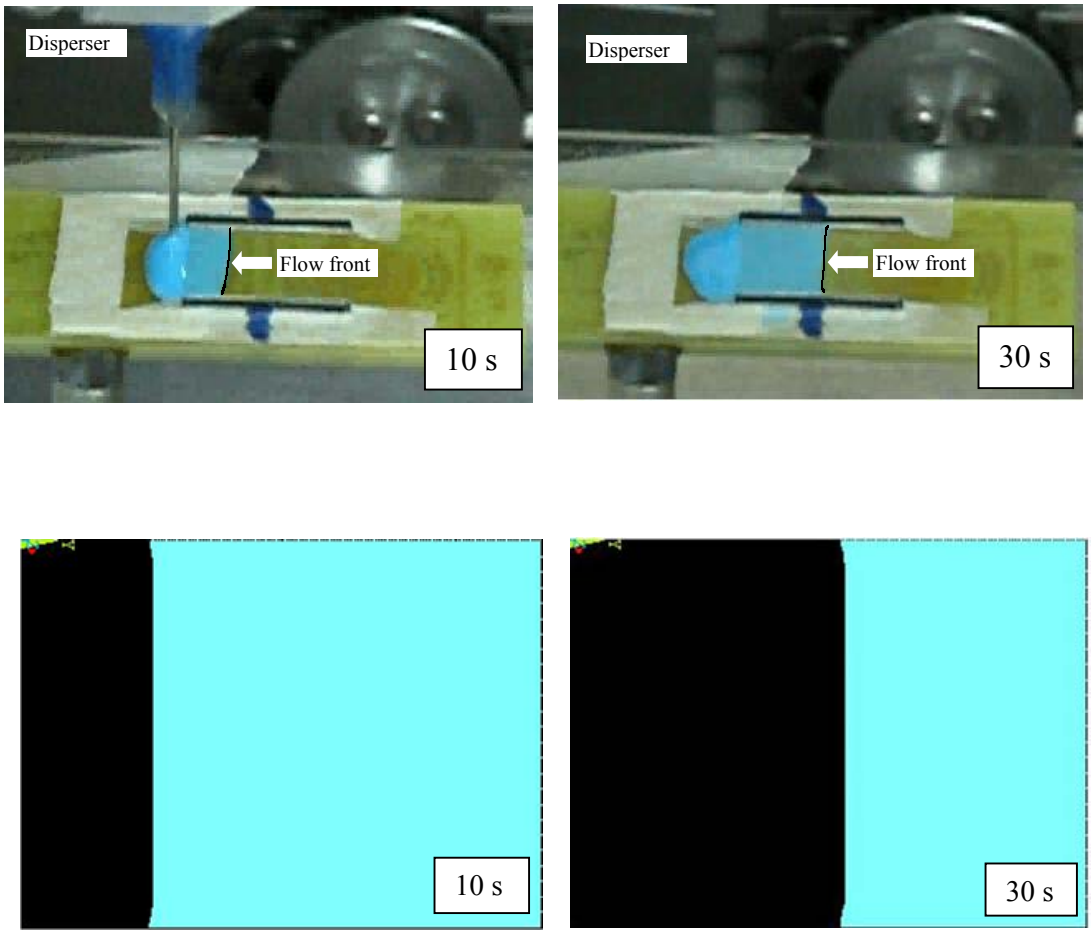

Figure 6.5 Simulated flow front (bottom) compared to measured flow front (top) at filling times of 10 and 30 s and a gap height of 85 μm.

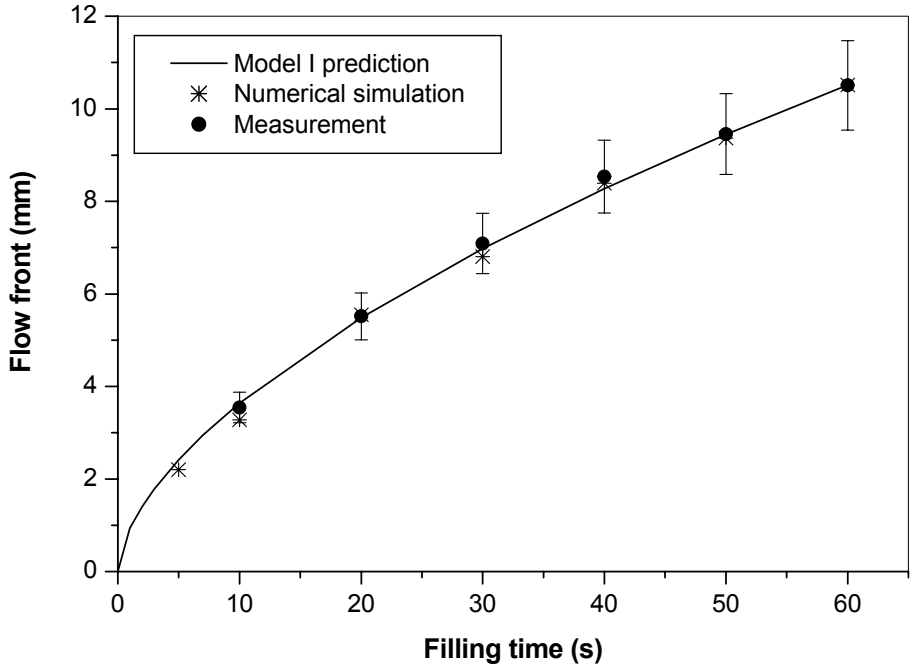

Figure 6.6 Comparison of the simulated flow front with the analytical and experimental results at a gap height of 85 μm.

Table 6.3 Comparison of the simulated flow front with the analytical and experimental results at a gap height of 85 μm.

Filling time (s)	Simulated results (mm)	Analytical prediction (mm)	Measured results (mm)	Relative error using simulation (%)	Relative error using analytical model (%)
10	3.3	3.64	3.5	5.7	4.0
20	5.5	5.49	5.5	0.0	0.2
30	6.8	6.98	7.1	4.2	1.7
40	8.4	8.27	8.5	1.2	2.7
50	9.4	9.44	9.5	1.1	0.6
60	10.5	10.52	10.5	0.0	0.2

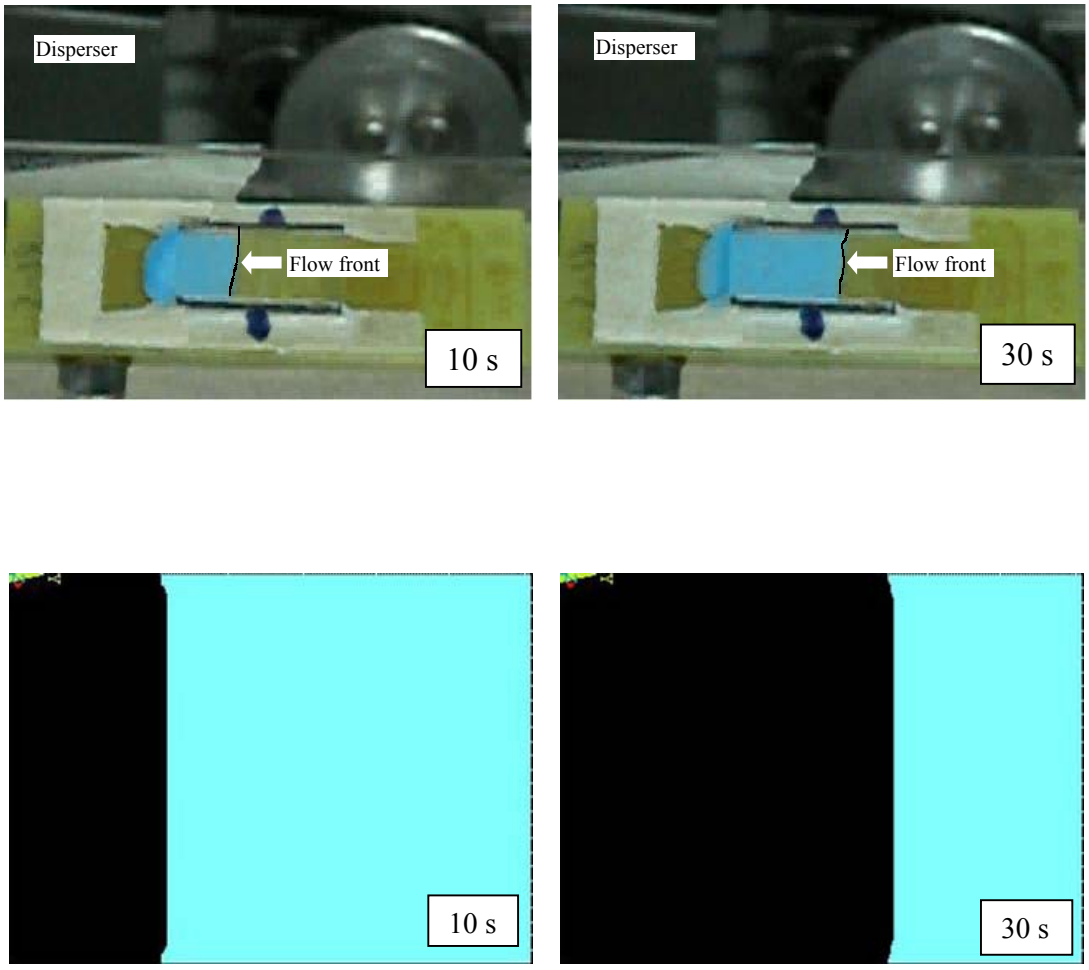

Figure 6.7 Simulated flow front (bottom) compared to measured flow front (top) at filling times of 10 and 30 s and a gap height of 115 μm.

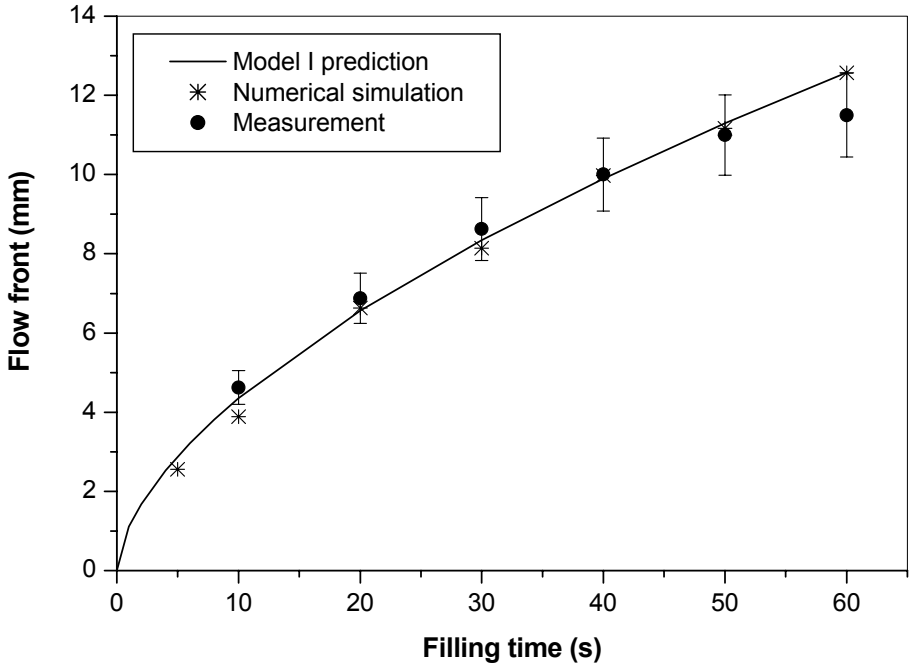

Figure 6.8 Comparison of the simulated flow front with the analytical and experimental results at a gap height of 115 μm.

Table 6.4 Comparison of the simulated flow front with the analytical and experimental results at a gap height of 115 μm.

Filling time (s)	Simulated results (mm)	Analytical prediction (mm)	Measured results (mm)	Relative error using simulation (%)	Relative error using analytical model (%)
10	3.9	4.35	4.6	15.2	5.3
20	6.6	6.56	6.9	4.3	4.9
30	8.1	8.35	8.6	3.5	3.0
40	10.0	9.90	10.0	0.0	1.0
50	11.2	11.30	11.0	1.8	2.7
60	12.6	12.58	11.5	9.6	9.4

6.3.2 The Underfill Flow in Flip-chip Packaging

The numerical simulation was based on the following conditions: the plane dimension of the die was 6 mm x 6 mm, the average gap height between the chip and the substrate was 50 μm, the solder bump pitch was 250 μm, and the diameter of the solder bump was 100 μm. The fitting parameters *m* and *n* of the power-law model were 0.06 Pa · s^n and 1.45, respectively, the contact angle on the FR4 substrate was 28.5°, the surface tension was 0.011 N/m, and the density was 1800 kg/m^3.

The simulation results are shown in Figures 6.9 and 6.10, and Table 6.5, in which the flow front positions were determined from the arithmetic mean value. From these results it can be seen that the calculated arithmetic mean of filling time does adequately match the measured result. However, the flow front shape does not match the measured results very well. This may be because the fluid distribution in the flip-chip underfill flow is three-dimensional in nature. Another possible cause is the variation in manufacturing accuracy for solder bumps, where they are treated as uniform in the finite element model. The simulation results show that that the numerical model can still give adequate prediction for the underfill flow process in flip-chip packaging. It is noted that the current simulation was based on the finite element model with the mesh size being about 75 μm (6808 elements). The Pentium 4 personal computer was used for the computation. To simulate the 2D underfill process for the filling time of 30 s shown in Figure 6.9, it takes about 8 hours for the current mesh model to complete the whole simulation process. Different meshes were tried. It is found that denser meshes other than one used in this study did not improve accuracy in any meaningful sense, however did

dramatically increase the computational time. For example, when the mesh size was reduced to a half of the current mesh size, i.e., mesh size is about 37.5 μm (24222 elements), the computation time would approximately be three days.

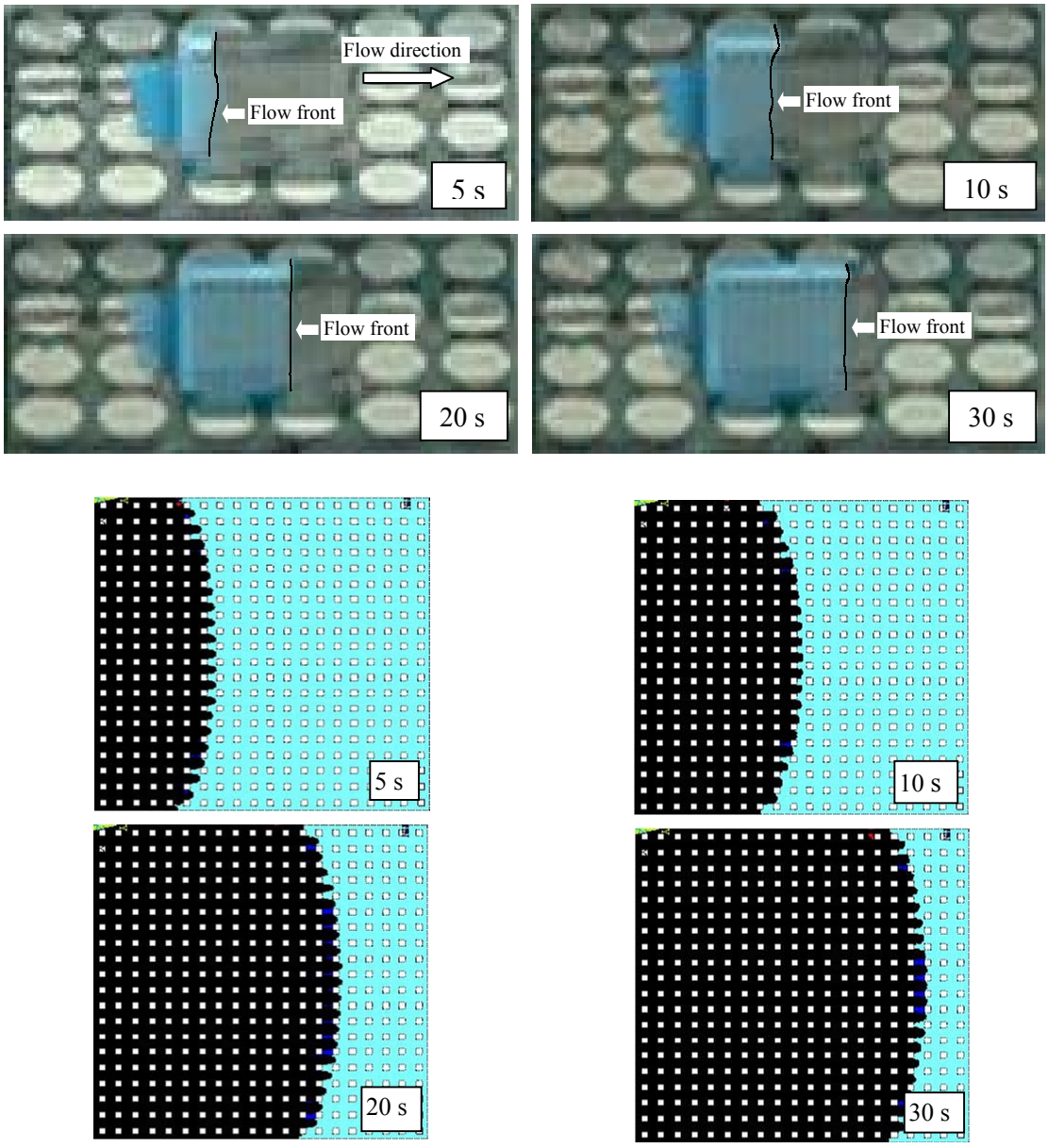

Figure 6.9 Simulated flow front (bottom) compared to measured flow front (top) at filling time of 5, 10, 20, and 30 s in flip-chip packaging.

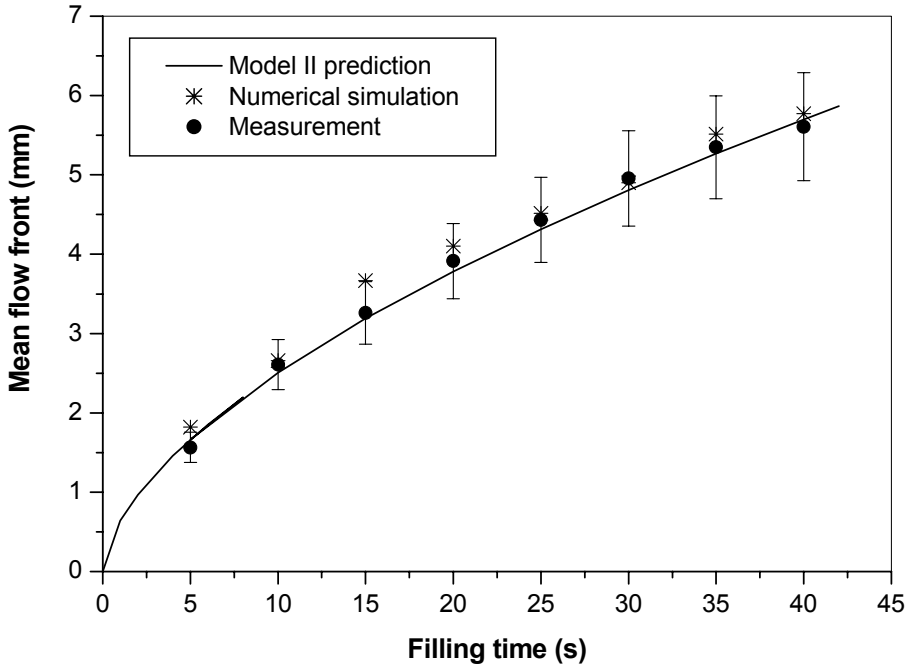

Figure 6.10 Comparison of the simulated flow front with the analytical and experimental results in flip-chip packaging.

Table 6.5 Comparison of the simulated flow front with the analytical and experimental results in flip-chip packaging.

Filling time (s)	Simulated results (mm)	Analytical prediction (mm)	Measured results (mm)	Relative error using simulation (%)	Relative error using analytical model (%)
5	1.8	1.64	1.6	12.5	2.8
10	2.7	2.51	2.6	3.8	3.5
15	3.7	3.19	3.3	12.1	3.4
20	4.1	3.78	3.9	5.1	3.0
25	4.5	4.32	4.4	2.3	1.9
30	4.9	4.81	5.0	2.0	3.9
35	5.5	5.27	5.3	3.8	0.6
40	5.8	5.70	5.6	3.6	1.8

Another verification of the model was carried out using the experimental results reported by Nguyen et al. (1999). The simulation and experiment were based on the following conditions: a 25 x 25 array pattern of solder bumps connected to the quartz die and the substrate, respectively. The dimension of the die was 6.7 mm x 6.7 mm, and the average gap height between the chip and the substrate was 56 μm. The bump diameter was 168 μm and the bump pitch was 262 μm. The meshed geometric model is given in Figure 6.1. The power-law coefficients *m* and *n* for this underfill fluid were 1.03 Pa · s^n and 1.09, respectively. The contact angle on the FR4 with the solder mask substrate was 25.5°, and the surface tension was 0.027 N/m.

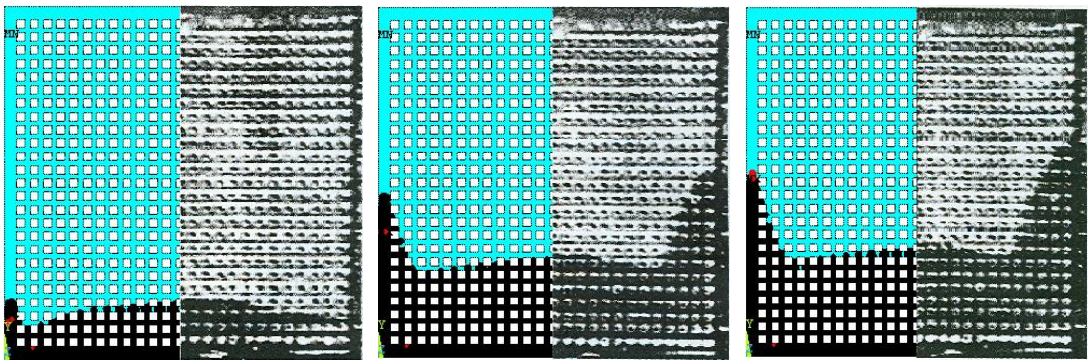

Figure 6.11 Simulated flow front (left) compared to measured flow front (right) at 5.3 s, 19.6 s, and 23.9 s elapsed flow time, respectively.

Figure 6.11 gives a comparison of the simulated flow front with the measured flow front at filling times of 5.3, 19.6 and 23.9 s. The right sides correspond to the measured flow front with the quartz dies reported by Nguyen et al. (1999). Due to symmetry, only half

of the device is shown in Figure 6.11. From these results, it can be seen that the predicted shape of the flow front does adequately match the measured flow front. This suggests that the developed numerical modeling model can be used to simulate the underfill flow process with relatively good results.

6.4 Modeling the Effect of the Edge Size on the Flow Front

One phenomenon relating to the package reliability is the void generated by the "racing effect" reported by Fine *et al*. (2000) and Nguyen *et al*. (1999), as shown in Figure 6.12.

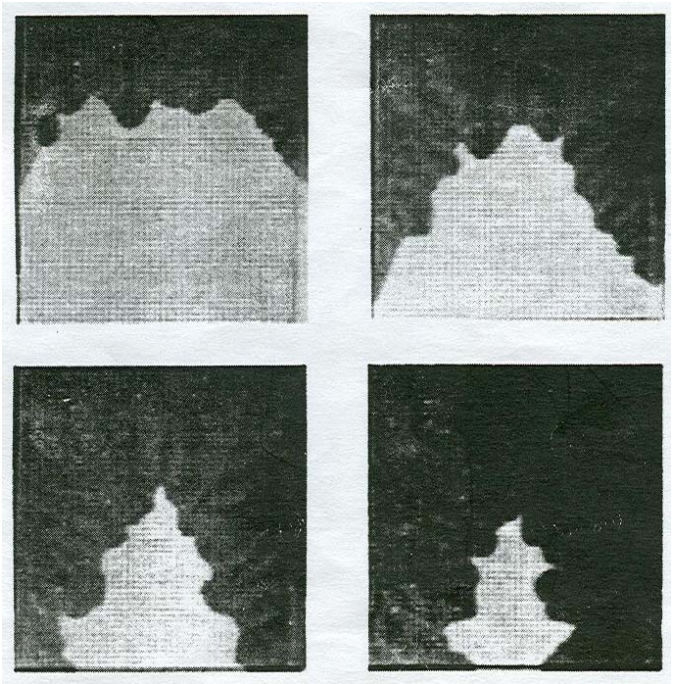

Figure 6.12 Flow front void and "racing effect" caused by edge flow (Nguyen *et al*., 1999, flow front shown at 19, 38, 57, and 76% of 728 s total underfill time, © 1999 IEEE, reprinted with permission).

Figure 6.12 presents the experimental observation reported by Nguyen *et al*. (1999). These experimental results showed that a faster flow develops along the edge which forms an air void in the center region of the chip. This phenomenon was termed the "racing effect" by Nguyen *et al*. (1999), and was generated by the wicking effect of the edges. Since the air void formed in the center region of chip creates areas of high stress concentrations and leads to early delamination of the encapsulant, the "racing effect" greatly reduces the reliability of the flip-chip package. Therefore, such voids should be eliminated.

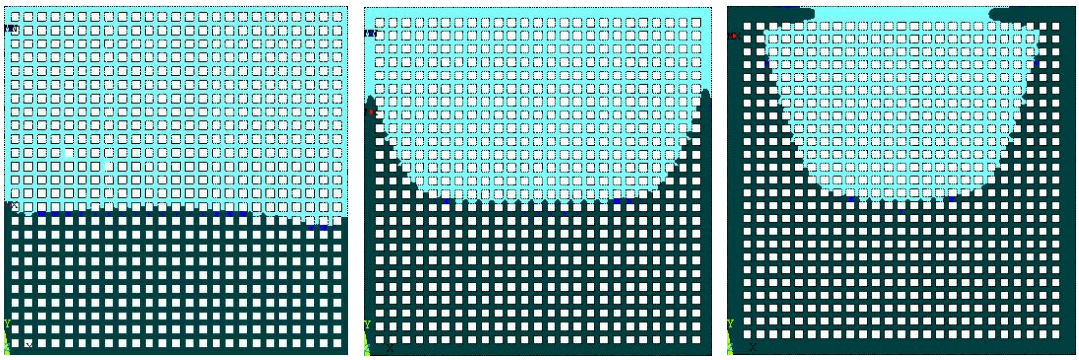

(a) (b) (c)

Figure 6.13 Simulated flow front at 23.9 s elapsed flow time. (a) edge size 75 μm; (b) edge size 175 μm; (c) edge size 275 μm.

To understand the possible reasons for the "racing effect", numerical simulation was employed to explore the influence of edge size on the flow front distribution, in which the pressure inlet boundary was used. Some simulation results are given in Figure 6.13. It can be seen from these results that the existing edge causes a "racing effect", which

causes the filling material to flow faster along the edges (Figure 6.13b, c). This "racing effect" is likely to form an air void in the center region and reduce the reliability of the flip-chip package. Through simulation of the underfill flow process for different edge sizes, it was found that the "racing effect" can be reduced by reducing the edge sizes.

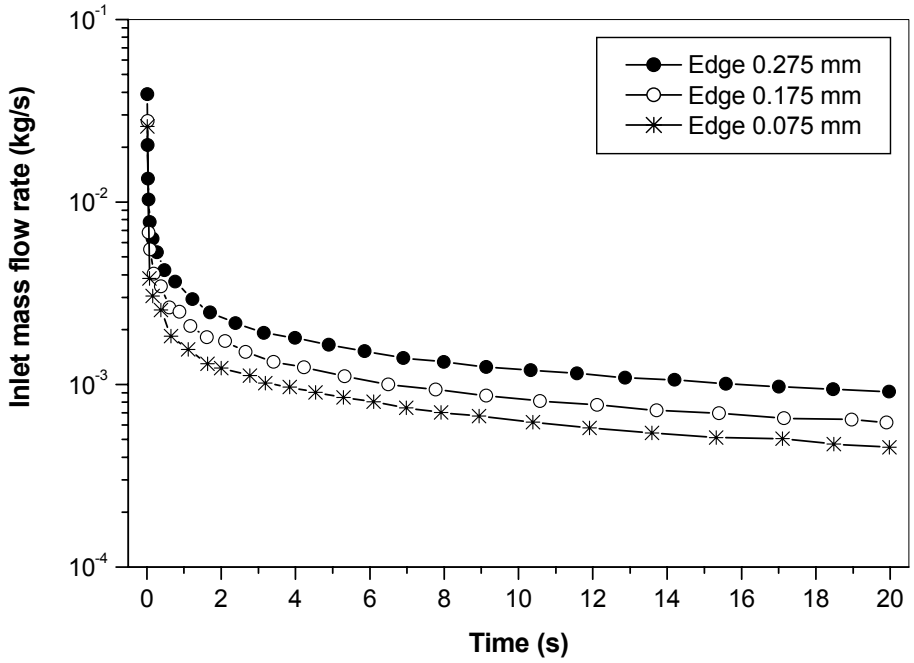

Figure 6.14 the influence of edge size on flow rate.

From the numerical study, it was also found that the inlet flow rate decreases as the filling time increases for different edge sizes as shown in Figure 6.14. This is because the capillary force driving the flow remains constant while the amount of encapsulant being pulled increases as the flow front progresses. Therefore, the energy dissipated through viscous shearing resistance increases. Another observation from Figure 6.14 is that the flow rate decreases with a decrease in the edge size. This phenomenon can be

explained by the fact that since the capillary force driving the flow remains constant, when the flow resistance increases due to a decrease in edge size, more energy is dissipated through viscous shearing. Therefore, to supply the same amount of underfill, a larger filling time is needed in the case of a small edge size. This suggests that in order to obtain a uniform flow front distribution and to avoid forming an air void in the center region, a small edge size is required.

6.5 Conclusion and Discussion

In this chapter, a numerical simulation model was developed for the investigation of a two-dimensional flow front distribution. The ANSYS (Version 7.0) software package was used to simulate the "racing effect" generated by the wicking effect on the shape of the flow front. In the numerical study presented in this chapter, a time-dependent velocity function boundary condition method was employed instead of the pressure boundary condition of the inlet to consider the flow resistance exerted by the parallel plates. The validity of the numerical simulation model was confirmed using experimental results. From these results, it can be seen that the developed numerical model gives a good prediction for the underfill flow between two parallel plates both in terms of the filling time and the flow front distribution. In the numerical simulation of flip-chip underfill flow, the calculated arithmetic mean of the filling time adequately matches the measured results. However, the flow front shape does not match the measured results well, which calls for further study.

Based on the numerical simulation, it was found that a "racing effect" is induced along the edge, which is in agreement with the observation made by Nguyen *et al*. (1999). The larger the edge size, the stronger the racing effect, and the less uniform the flow front. This "racing effect" can be reduced by decreasing the edge size.

It was also found that the inlet flow rate decreases with increasing filling time due to the constant capillary driving force, since with the flow front progressing, the amount of the encapsulant being transported increases and the energy dissipated through viscous shearing resistance increases. Therefore, to supply the same amount of encapsulant, more time is required in the case of a smaller edge size. This suggests that in order to obtain a uniform flow front shape, to avoid forming an air void in the center region of the die, and to improve the overall reliability of the flip-chip package, a small edge size and long filling time are required.

7 PARAMETER VARIATION STUDY

In Chapter 4, a lumped parameter analytical model, Model II, was developed for predicting the characteristics in the underfull flow process in flip-chip packaging. One of the advantages of the lumped parameter analytical model is that it can be readily used for analyzing the design and process parameters with the purpose of optimizing device performance. This chapter describes a study of how the design and process parameters affect the performance of the underfill process. The package design parameters are the bump pitch, solder bump diameter, and gap height. The packaging process parameters are pressure and temperature. The process performance indices are the flow front, fluid distribution, and filling time.

7.1 Design Parameter Analysis Using Model II

From Model II, i.e. equation (4-29) in Chapter 4, the fluid filling time in the flip-chip underfill process is given as a function of package design parameters, i.e.

$$t_f = \frac{2n+1}{n+1}\left(\frac{mhW(W+d)}{2\sigma\cos\theta(W^2+dW-dh)}\right)^{\frac{1}{n}}\left(\frac{2L}{h}\right)^{\frac{n+1}{n}} \tag{7-1}$$

where t_f is the filling time, W is the clearance between two adjacent solder bumps (clearance is the solder bump pitch minus the solder bump diameter), h is the gap height, d is the solder bump diameter, L is the length of the cavity, σ is the surface tension coefficient, θ is the contact angle, and m and n are the coefficient and index of the power-law viscosity equation, respectively. When the design parameters and/or the process parameters are changed, the performance indices may change. Optimization of package design and/or process design needs to understand how the design and process parameters affect the performance.

7.1.1 Effect of the Solder Bump Pitch on Filling Time with Different Gap Heights

The influence of the solder bump pitch on filling time with different gap heights is plotted in Figure 7.1. From this figure it can be observed that: (1) for a fixed solder bump pitch and solder bump diameter, the filling time decreases with an increase in gap height; and (2) for a fixed solder bump diameter (say 100 μm), when the bump pitch reduces to a certain value (say 300 μm), filling time begins to increase sharply; yet when the bump pitch is greater than this value, the influence of the bump pitch on filling time becomes very small. This phenomenon agrees with the experimental results reported by Fine et al. (2000), who experimentally investigated the influence of different bump pitches, 200 μm, 250 μm, and 400 μm, on filling time. Their results are shown in Table 7.1. The conditions in their experiment were as follows: the length of the chip was 12.7 mm, the thickness of the cavity was 75 μm, the solder bump pitches were 200 μm, 250

μm, and 400 μm, the contact angle on the FR4 substrate was 17.5°, and the surface tension was 0.0312 N/m at $80^{o}C$. The solder bump diameter was 100 μm for the 200 μm solder bump pitch, and 125 μm for the 250 μm and 400 μm solder bump pitches, respectively. Table 7.1 also shows a comparison of the predicted and the measured filling times with different bump pitches. The predicted filling time was calculated using Model II. It can be seen from Table 7.1 that the predicted results agree well with the measured results. Both the measured and predicted results indicate that the filling time decreases with an increase in the bump pitch. For all cases tested, it was found that the slowest flow occurred for the high solder bump density geometry (200 μm pitch), and that when the solder bump pitches were increased to 250 μm and 400 μm, respectively, faster flow was observed. These experimental results indicate that the small solder bump pitches increase the flow resistance and cause a longer filling time, which agrees with intuition.

A similar phenomenon was also found in the measurements conducted by Gordon et al. (1999). In their measurements using a 50 μm gap height, they found that for the full array bumps with the 250 μm and 500 μm pitches, the filling times were nearly same. This means that for the flip-chip geometry used in their test, the flow resistance caused by the clearance between the adjacent solder joints becomes insignificant when the bump pitch is larger than 250 μm.

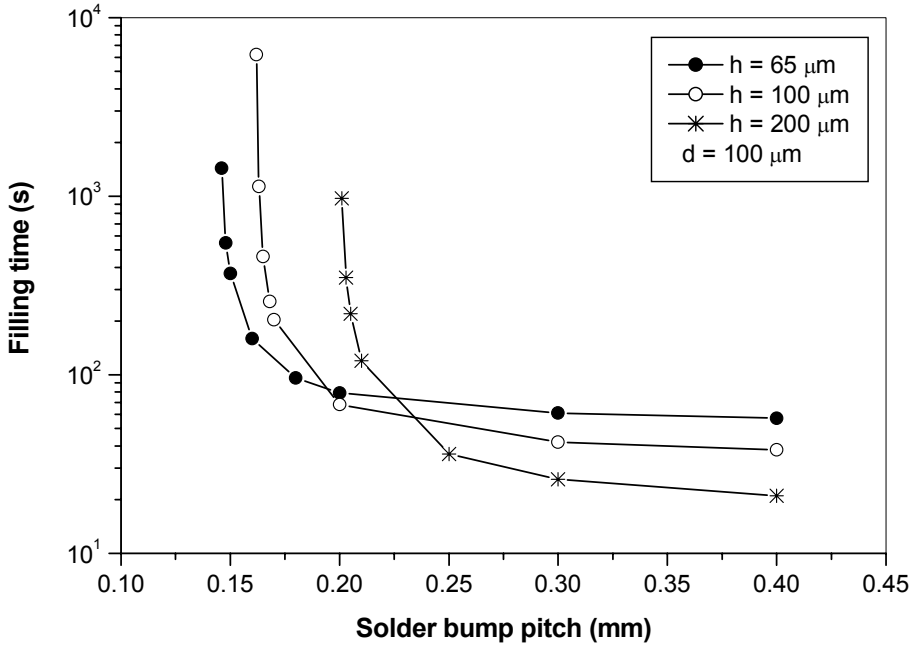

Figure 7.1 Effect of the solder bump pitch on filling time with different gap heights.

Table 7.1 The effect of bump pitch on filling time.

Bump pitch (μm)	Measured filling time (Fine et al., 2000) (s)	Calculated filling time (analytical Model II) (s)	Relative error (%)
200	75	73.2	2.4
250	70	65.7	6.1
400	52	51.0	1.9

7.1.2 Effect of the Solder Bump Pitch on the Filling Time with Different Solder Bump Diameters

Figure 7.2 shows the influence of the solder bump pitch on the filling time with different solder diameters and a fixed gap height. From these results it can be seen that for a fixed solder bump diameter, when the bump pitch reduces to a certain value, say 400 μm (solder bump diameter: 200 μm), the fluid filling time begins to increase sharply. However, when the solder bump pitch is greater than this value, the influence of the solder bump pitch on the filling time becomes small. This means that for a specific design of flip-chip packaging, the solder bump pitch should be larger than a certain value in order to reduce flow resistance and to make filling materials flow more quickly.

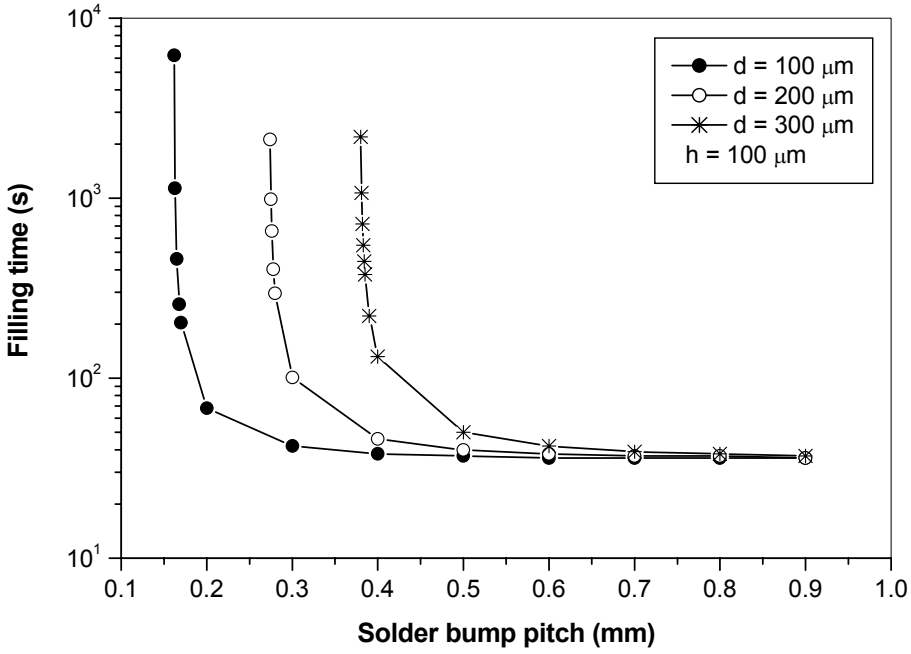

Figure 7.2 Effect of the solder bump pitch on the filling time with different solder bump diameters.

7.1.3 Effect of the Solder Bump Diameter on the Filling Time with Different Solder Bump Pitches

Figure 7.3 illustrates the effect of the solder bump diameter on the filling time for different solder bump pitches.

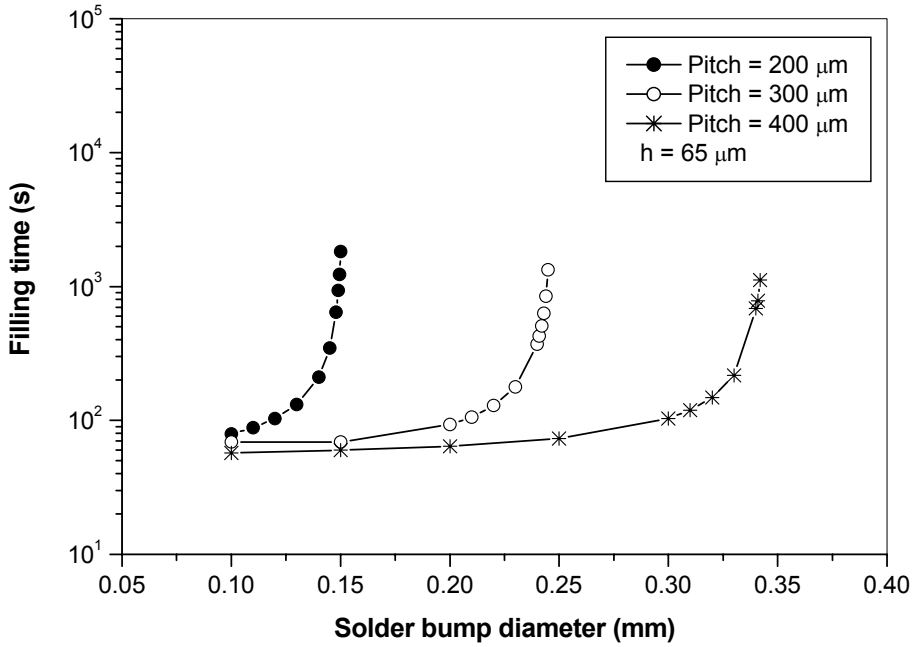

Figure 7.3 Effect of the solder bump diameter on the filling time with different solder bump pitches.

It can be seen from Figure 7.3 that for a fixed solder bump pitch, the filling time increases with an increase of the solder diameter. Before the solder bump diameter is increased to a certain value, the increase of the filling time is relatively small. After the solder diameter increases beyond this critical diameter, the filling time increases very quickly. For example, the critical solder bump diameter is about 300 μm for the 400 μm

solder bump pitch (Figure 7.3). These results indicate that the critical solder bump diameter increases with an increase of the solder bump pitch. These results suggest that in the design of the solder bump pattern in the flip-chip package, the solder diameter should be below its critical value in order to reduce the filling time.

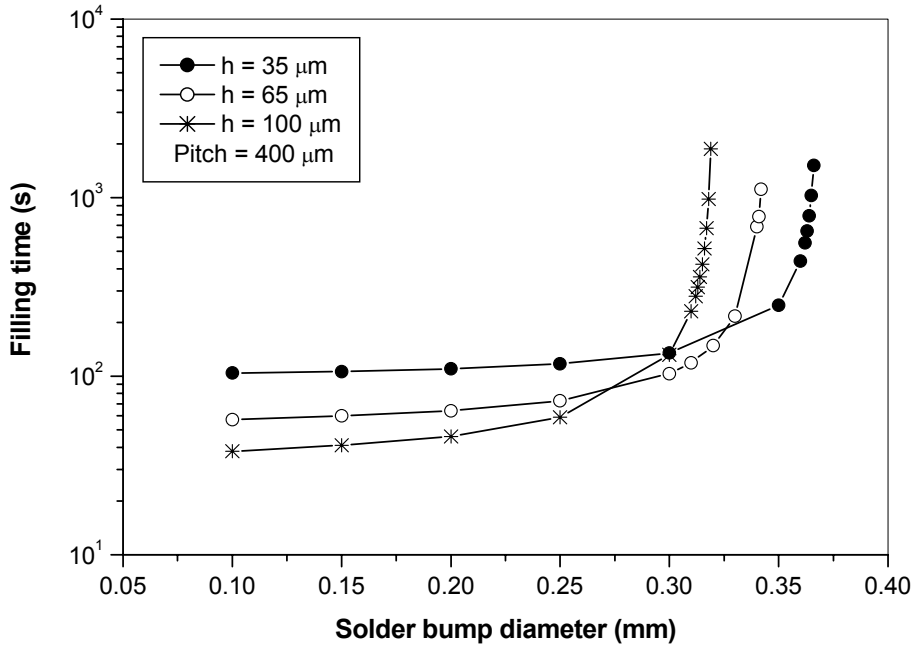

Figure 7.4 Effect of the solder bump diameter on filling time with different gap heights.

7.1.4 Effect of the Solder Bump Diameter on the Filling Time with Different Gap Heights

Figure 7.4 shows the influence of the solder bump diameter on the filling time for different gap heights. These results show that for a fixed solder bump diameter, the filling time decreases with an increase in gap height. Another phenomenon observed from these results is that the critical solder diameter mentioned before decreases with an

increase in gap height. This is because when the frictional resistance decreases due to an increase in the gap height, the flow resistance caused by the clearance between the adjacent solder joints eventually becomes the dominant factor affecting the filling process.

7.1.5 Effect of the Clearance on the Filling Time with Different Solder Bump Diameters

The critical pitch phenomenon discussed above seems to imply that the most influential factor is the clearance between two solder bumps, that is, there exists a notion called critical clearance. When the actual clearance is greater than the critical clearance, the filling time is relatively unaffected by the bump clearance. The critical clearance phenomenon agrees with the experimental results reported by Fine et al. (2000) and Gordon et al. (1999). The experiment by Fine et al. (2000) showed that the slowest flow occurred in the high solder bump density geometry, i.e., 200 μm pitch (with 100 μm clearance), and that when the solder bump pitch was increased to 250 μm and 400 μm (with 125 μm and 275 μm clearance, respectively), the flows became faster. In this case, the critical clearance is 125 μm. The experimental results, as shown in Figure 3.3, clearly indicate that the filling material in the perimeter array flows faster than in the full array package. They also found that the filling time for the 400 μm full array pattern was close to or faster than the perimeter array pattern. This is because the clearance in the 400 μm full array is 275 μm, larger than its critical clearance. These observations confirmed that when the clearance of the flip-chip packaging is greater than its critical clearance, the solder bump has very little effect on the filling time. A similar

phenomenon was also observed in the measurement of Gordon et al. (1999). In their experiment with a 50 μm gap height, they found that for full array bumps with a 250 μm and 500 μm pitch (174 μm and 348 μm clearance, respectively), the filling times were nearly the same. This observed phenomenon agrees with the predictions given by the analytical model developed in this thesis.

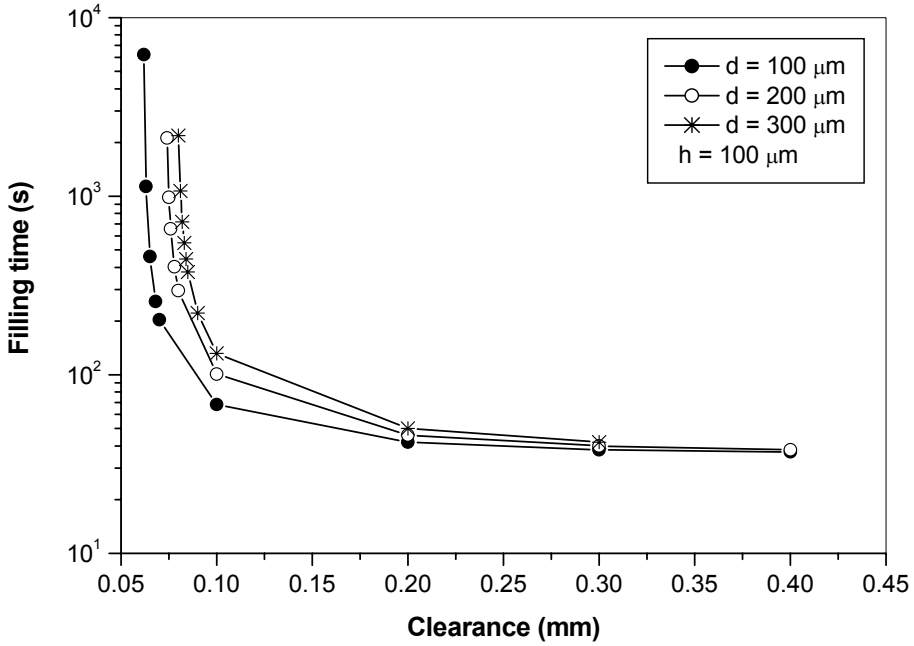

Figure 7.5 Effect of the clearance on filling time with different solder bump diameters.

Figure 7.5 further shows the influence of the clearance on the filling time with different solder bump diameters for a fixed gap height. From these results it can be seen that for a fixed solder bump diameter, when the clearance reduces to a certain value, say 200 μm, the filling time begins to increase sharply due to the increase of the flow resistance caused by the clearance resistance. However, when clearance is greater than this value, the influence of clearance on filling time becomes small. This phenomenon agrees with

a similar phenomenon observed for the bump pitch and implies the notion of the critical clearance. From Figure 7.5 it can be seen that the solder bump diameter has little influence on the critical clearance (Note that clearance is the solder bump pitch minus the solder bump diameter). Therefore, one can conclude that critical clearance is more profound than the solder bump diameter as an index in the flip-chip package design. Further, Figure 7.6 shows the effect of the clearance on filling time with different gap heights at fixed solder bump diameter (100 μm). The results show that when the gap height decreases, the critical clearance decreases.

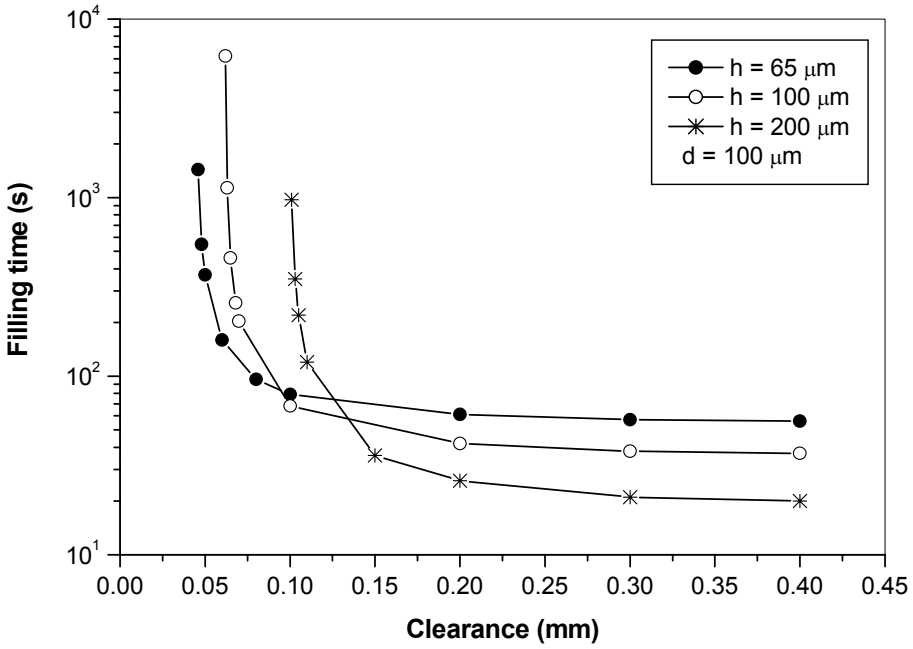

Figure 7.6 Effect of the clearance on the filling time with different gap height.

7.2 Design Parameter Analysis Using the Numerical Model

7.2.1 The Effect of Clearance on the Flow Distribution and the Filling Time

Using the numerical model developed in Chapter 6, simulations were carried out to investigate the effect of clearance on the flow distribution and filling time. The simulation was based on a 25 x 25 full array of a solder bump pattern. The dimension of the die was 6.7 mm x 6.7 mm, and the average gap height between the chip and the substrate was 56 μm. The bump width was 168 μm, and the bump pitch was 262 μm. The power-law coefficient and index *m* and *n* are 1.03 Pa · s^n and 1.09, respectively. The contact angle on the FR4 substrate with the solder mask substrate was 25.5° and the surface tension was 0.027 N/m at 80°C.

Figure 7.7 shows the effect of the clearance on the filling time for the flip-chip pattern presented above. From Figure 7.7 it can be seen that the critical clearance for this flip-chip pattern is around 60 μm. The numerical simulation results in Figure 7.8 show the effect of the clearance on the fluid distribution and fluid filling time (at 30 s). Specifically, the fluid distribution and the filling time are significantly different for the case below the critical clearance (50 μm); and that above the critical clearance (50 μm). The clearance of 70 μm has nearly a similar performance to the clearance of 60 μm. This result further verifies the existence of a critical clearance; in this case the fluid distribution is affected as well.

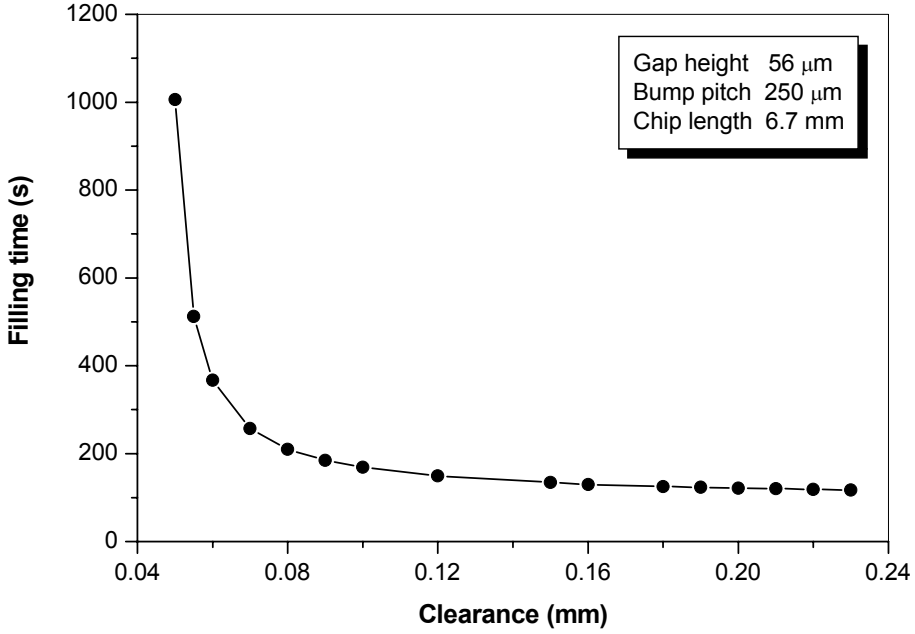

Figure 7.7 Filling time versus clearance of flip-chip package (gap height: 56 μm, bump pitch: 250 μm).

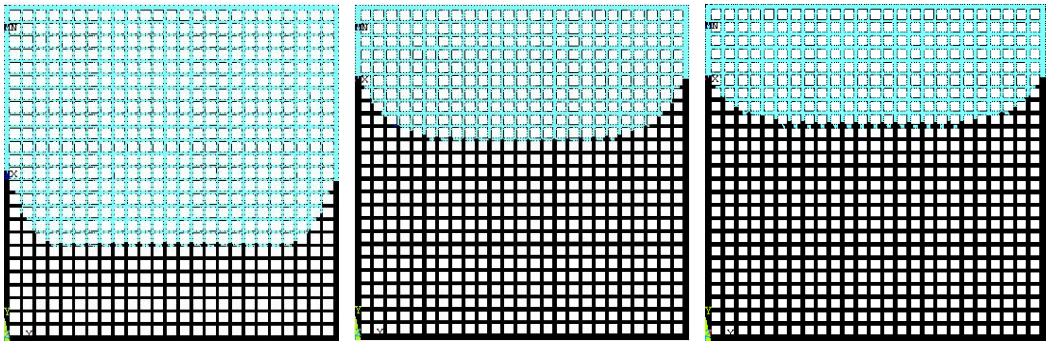

(a) (b) (c)

Figure 7.8 Simulated flow front at 30 s elapsed flow time for (a) clearance: 50 μm; (b) clearance: 60 μm; (c) clearance: 70 μm.

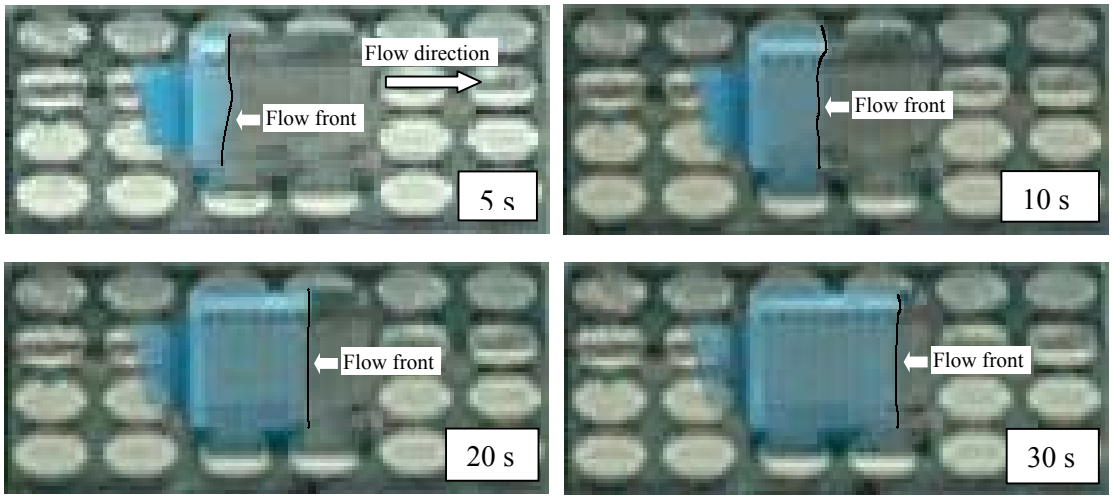

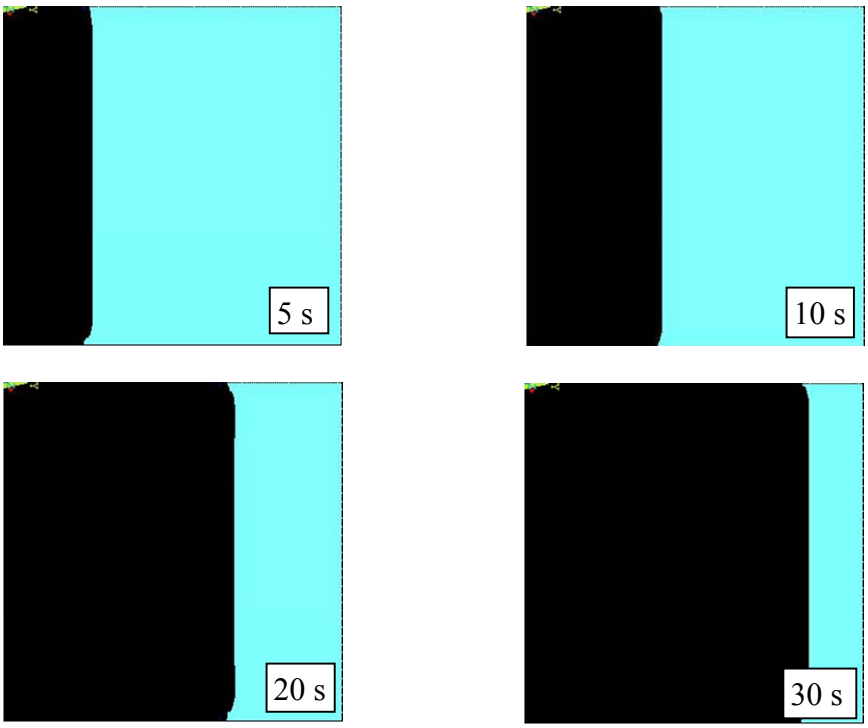

Figure 7.9 Simulated flow front between two parallel plates (bottom, gap height: 50 μm) compared to measured flow front of flip-chip (top) at filling time of 5, 10, 2s, and 30 s.

7.2.2 Comparison: The Simulation and the Experiment

To further examine the effect of the critical clearance on the filling time, a comparison between the simulation for the underfill flow between two parallel plates and the experiment for the underfill flow in the flip-chip package is given in Figure 7.9.

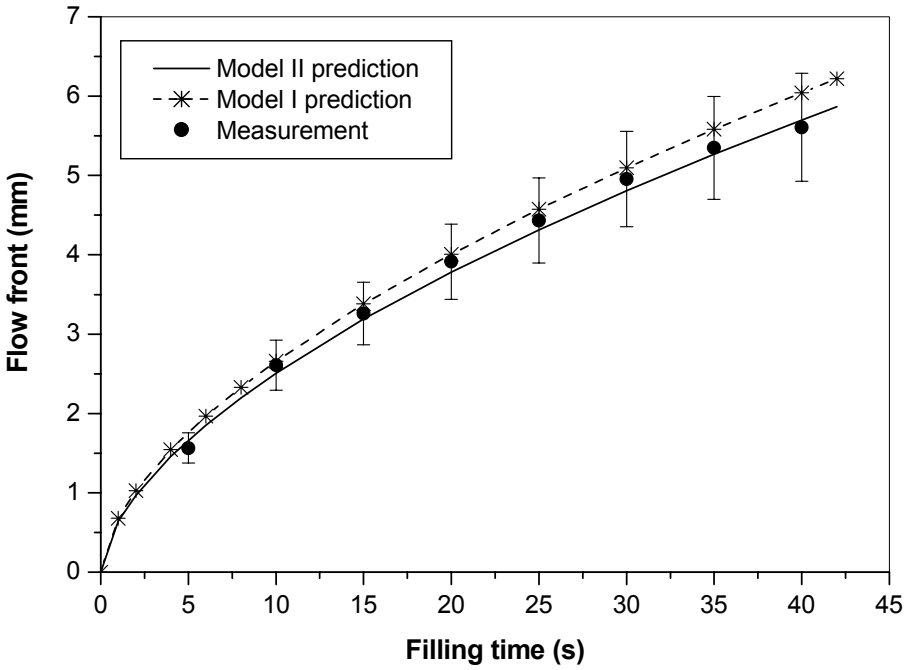

Figure 7.10 Comparison of the flow front predicted with Model II and Model I for flip-chip underfill process.

These results show that the measured flow front at different times in the flip-chip package is very close to the simulated flow front for the underfill flow between two parallel plates. This implies that for this flip-chip pattern, the solder bump has very little

influence on the underfill flow. To further confirm this observation, a comparison between the measured results for the theoretical predictions using Model I and Model II, are given in Figure 7.10 and Table 7.2. The last column is calculated by $\left|x_{f(I)} - x_{f(II)}\right| / x_{f(II)}$. Where $x_{f(I)}$ and $x_{f(II)}$ are the positions of the flow front calculated with Model I and Model II, respectively.

Table 7.2 Comparison of the flow front predicted with Model II and Model I for flip-chip underfill process.

Filling time (s)	Measured Results (flip-chip) (mm)	Analytical Model II (flip-chip) (mm)	Analytical Model I (parallel plates) (mm)	Relative difference by replacing Model II with Model I (%)
10	2.6	2.51	2.66	5.98
15	3.3	3.19	3.38	5.96
20	3.9	3.78	4.01	6.08
25	4.4	4.32	4.57	5.79
30	5.0	4.81	5.10	6.03
35	5.3	5.27	5.59	6.07
40	5.6	5.70	6.04	5.96

From the results shown in Figure 7.10 and Table 7.2, it can be seen that the flow front calculated with Model I is very close to the predictions with Model II. The relative difference caused by replacing Model II with Model I is about 6%. This phenomenon suggests that the flow resistance caused by the solder bump to the underfill flow in this flip-chip pattern is very small. This is because the critical clearance of the experimental flip-chip pattern is around 50 μm (see Figure 7.11), much less than the actual clearance of the flip-chip pattern for measurement (150 μm).

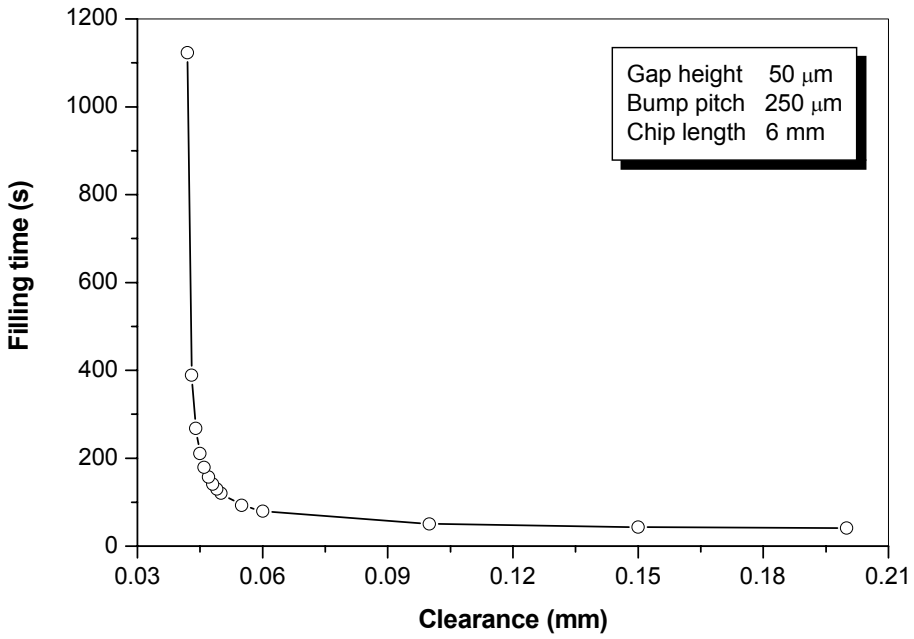

Figure 7.11 Filling time versus clearance of flip-chip package.

It is worth mentioning that an earlier discussion in Chapter 5 showed that the Washburn model and the Washburn model with consideration of the solder bump did not show significant difference in predicting the filling time for a particular flip-chip package. That result can now be explained by reference to the notion of critical clearance. The implication of this finding is that the model for the two-parallel-plate geometry can be used for the filling time simulation of the flip-chip underfill flow when the clearance of the flip-chip package is larger than its critical clearance.

7.3 Dimensionless Correlation

From the discussion in the preceding sections, it was found that the critical clearance is an important index for evaluating the flip-chip package design. From a design viewpoint, there is a need to estimate the critical clearance for a given package design and subsequently adjust the design and/or process parameters so that the actual clearance is larger than the critical clearance. In the following section, this aspect will be implemented using dimensional analysis (White, 1986).

7.3.1 Dimensionless Filling Time

The relationship among the bump pitch P_t, solder bump diameter *d*, and clearance *W* is given by equation (3-38), i.e.,

$$P_t = W + d \tag{7-2}$$

Substituting this equation into equation (7-1) gives

$$t_f = \frac{2n+1}{n+1}\left(\frac{mhWP_t}{2\sigma\cos\theta(WP_t - hP_t + hW)}\right)^{\frac{1}{n}}\left(\frac{2L}{h}\right)^{\frac{n+1}{n}} \tag{7-3}$$

Now, define a set of dimensionless parameters as follows:

$$t_f^* = \frac{t_f}{\left(\frac{mP_t}{2\sigma\cos\theta}\right)^{\frac{1}{n}}} \tag{7-4}$$

$$W^* = \frac{W}{P_t} \tag{7-5}$$

$$h^* = \frac{h}{P_t} \tag{7-6}$$

$$L^* = \frac{L}{P_t} \tag{7-7}$$

where the t_f^* is the dimensionless filling time, W^* is the dimensionless clearance, h^* is the dimensionless gap height, and L^* is the dimensionless chip length. Substituting equations (7-4) to (7-7) into equation (7-3) gives

$$t_f^* = \frac{2n+1}{n+1}\left(\frac{h^*W^*}{W^* - h^* + h^*W^*)}\right)^{\frac{1}{n}}\left(\frac{2L^*}{h^*}\right)^{\frac{n+1}{n}} \tag{7-8}$$

From equation (7-8) the dimensionless filling time t_f^* is a function of the dimensionless clearance W^* for a fixed gap height and chip length.

Figure 7.12 plots the influence of the dimensionless clearance on the dimensionless filling time for different dimensionless gap heights with n =1.4, L^* = 24. From these results it can be seen that when the dimensionless clearance reduces to a certain value, the dimensionless filling time begins to increase sharply. However, when the dimensionless clearance is greater than this value, the influence of the dimensionless clearance on the dimensionless filling time becomes small. This value increases with an increase of the dimensionless gap height and is only a function of the dimensionless gap height for a specified underfill material. For different underfill materials, this value is affected by power index n.

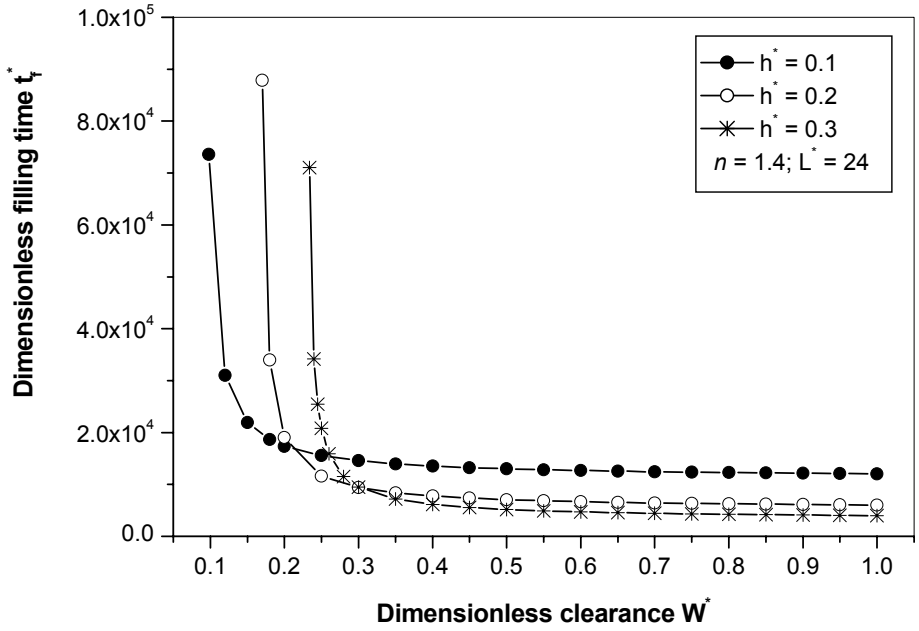

Figure 7.12 Effect of the dimensionless clearance on the dimensionless filling time with different dimensionless gap heights.

7.3.2 Dimensionless Critical Clearance

The dimensionless critical clearance is defined as:

$$W^*_{critical} = \frac{t^*_{f,W} - t^*_{f,W^*=1}}{t^*_{f,W^*=1}} = 50\% \tag{7-9}$$

where t^*_{f,W^*} is the dimensionless filling time for the dimensionless clearance within $0 < W^* < 1$, $t^*_{f,W^*=1}$ is the dimensionless filling time for the dimensionless clearance $W^* = 1$, which is the dimensionless filling time without the flow resistance of a solder bump.

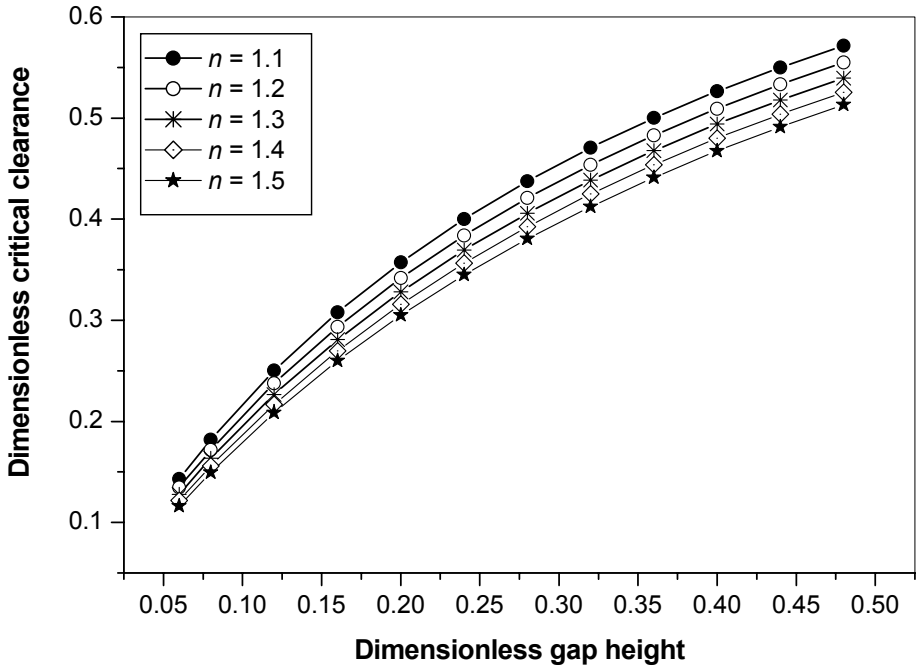

Figure 7.13 Dimensionless critical clearance versus dimensionless gap height.

Figure 7.13 shows the dimensionless critical clearance versus the dimensionless gap height, in which the influence of the power-law index *n* for different underfill materials is also illustrated. From these results it can be seen that the dimensionless critical clearance increases with an increase of the dimensionless gap height. For different underfill materials, the dimensionless critical clearance decreases with an increase of the power-law index *n*.

For flip-chip applications, the dimensionless critical clearance can be fitted as a correlation of the dimensionless gap height using a second-order polynomial, i.e.

$$W^*_{critical} = a + bh^* + c(h^*)^2 \tag{7-10}$$

where *a*, *b*, and *c* are fitting coefficients, the value of which are given in Table 7.3. Figure 7.14 shows that the second-order polynomial can give a very good fit for the dimensionless critical clearance.

Table 7.3 Coefficients of the correlation of dimensionless critical clearance.

n	*a*	*b*	*c*
1.1	0.044128	1.868427	-1.63119
1.2	0.038998	1.799307	-1.53522
1.3	0.034711	1.737582	-1.45205
1.4	0.031258	1.680676	-1.37689
1.5	0.028506	1.627549	-1.30727

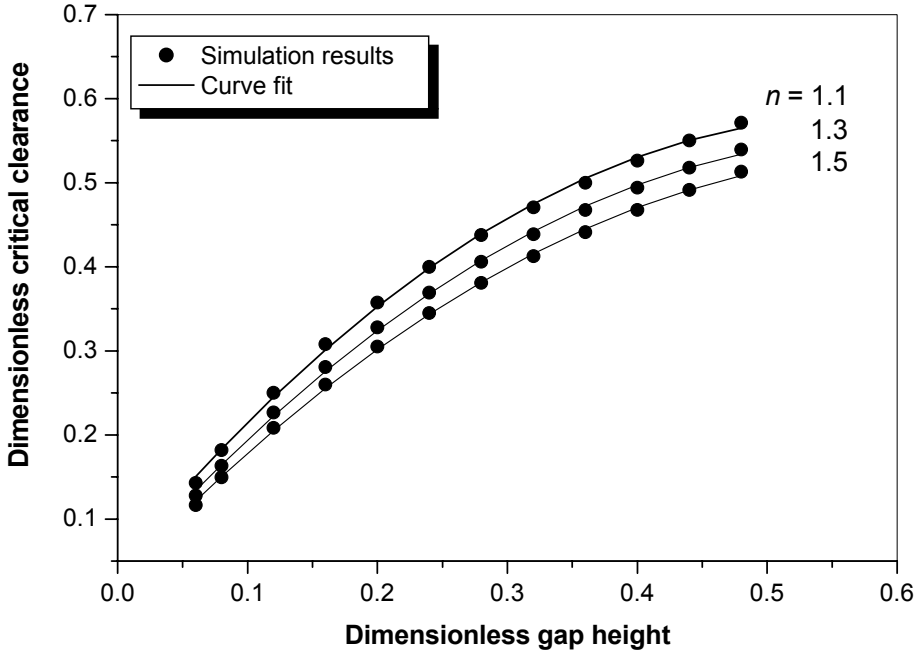

Figure 7.14 Dimensionless critical clearance versus dimensionless gap height.

If the dimensionless critical clearance $W^*_{critical}$ is divided by $(n+1)/n$, the dimensionless critical clearance can be further fitted by the following second-order polynomial, i.e.,

$$\frac{W^*_{critical}}{(n+1)/n} = 0.0201 + 0.9776h^* - 0.8157(h^*)^2 \tag{7-11}$$

A comparison between the simulation results and those calculated using the correlation above is plotted in Figure 7.15. From these results it can be seen that the second-order polynomial can give a very good fit for the simulated dimensionless critical clearance.

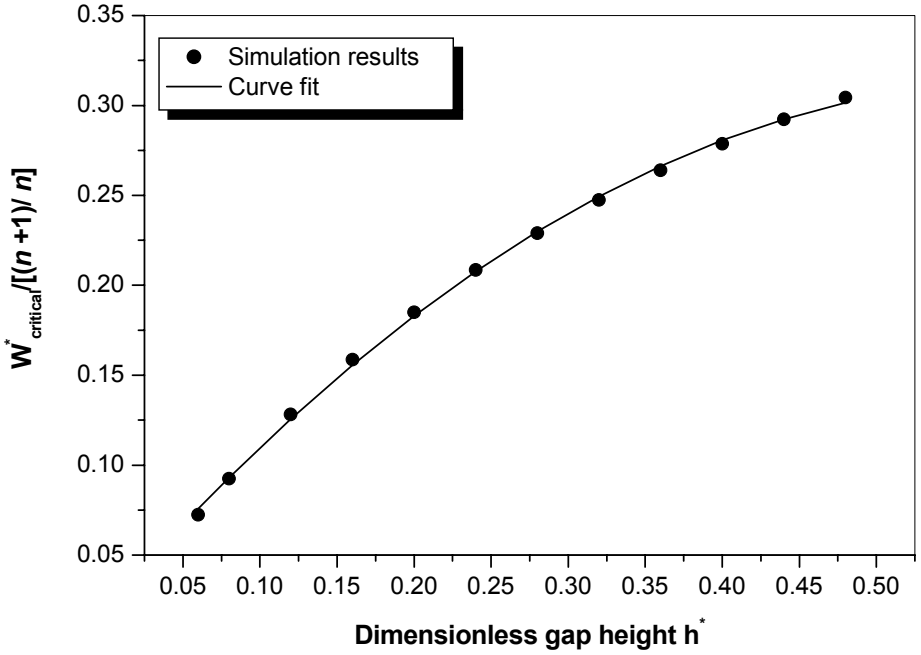

Figure 7.15 $W^*_{critical}/\left[(n+1)/n\right]$ versus dimensionless gap height.

The application of the dimensionless critical clearance $W^*_{critical}$ in the real package design can be explained as follows. Suppose that there is an initial design of the flip-chip package, denoted by DP0. From the DP0 pattern, one can obtain a dimensionless clearance W^*. Since the type of the underfill material is known, the n is also known. Therefore, the dimensionless critical clearance $W^*_{critical}$ can be found from equation (7-11). The package design (including the process design, temperature in this case) should be such as to ensure that $W^* > W^*_{critical}$. One can check whether this design criterion is satisfied. If not, then one needs to change either the design parameters or the temperature of the substrate.

7.4 Effect of Temperature on Underfill Flow

In the underfill flow driven by capillary action, the fluid dispensed is under the atmospheric pressure of the environment which is a constant. However, the temperature of the substrate or the underfill material can be changed. The effect of temperature on the underfill flow is illustrated in the Figures 7.16 to 7.19. Figure 7.16 and Figure 7.17 show the flow front versus filling time for the underfill flow between two parallel plates with gap heights of 45 μm and 85 μm, respectively. Figure 7.18 shows the flow front versus filling time for the underfill flow in a flip-chip package. Figure 7.19 shows the flow front distribution with a gap height of 85 μm. From these results it can be seen that temperature has a significant effect on the fluid filling time. When the temperature decreases, the time required filling the same chip length increases significantly. The temperature effect becomes more significant with an increase of the filling time.

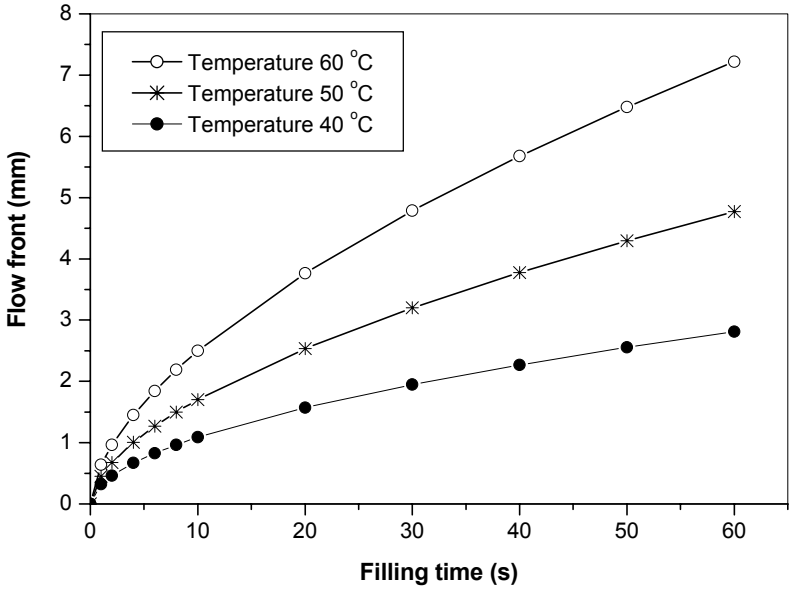

Figure 7.16 Flow front versus filling time with gap height 45 μm.

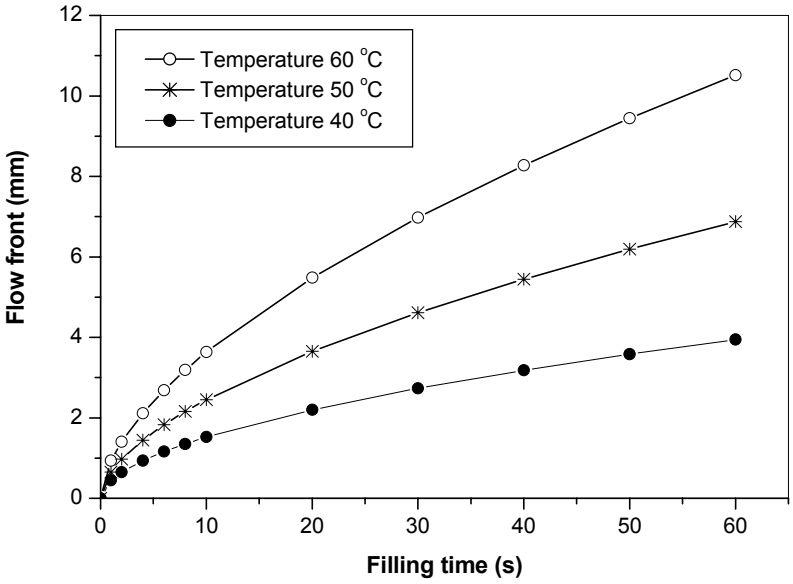

Figure 7.17 Flow front versus filling time with gap height 85 μm.

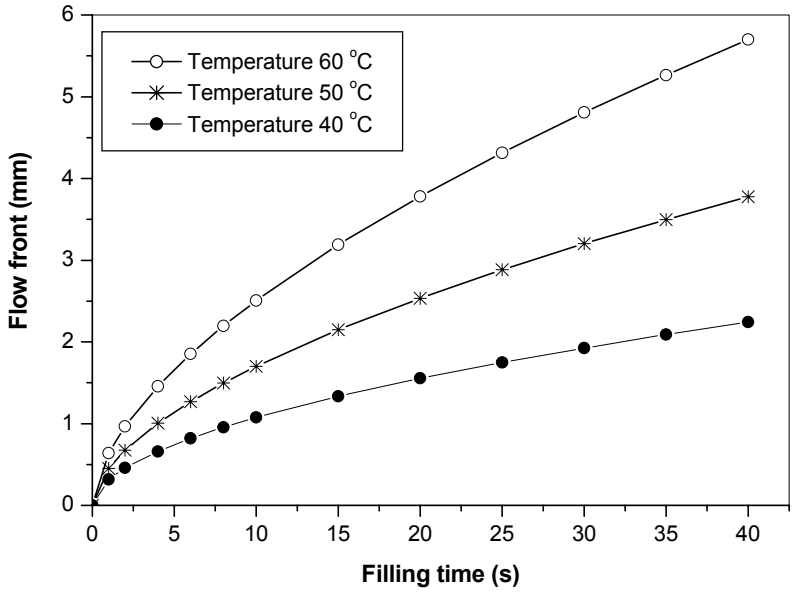

Figure 7.18 Flow front versus filling time for flip-chip underfill.

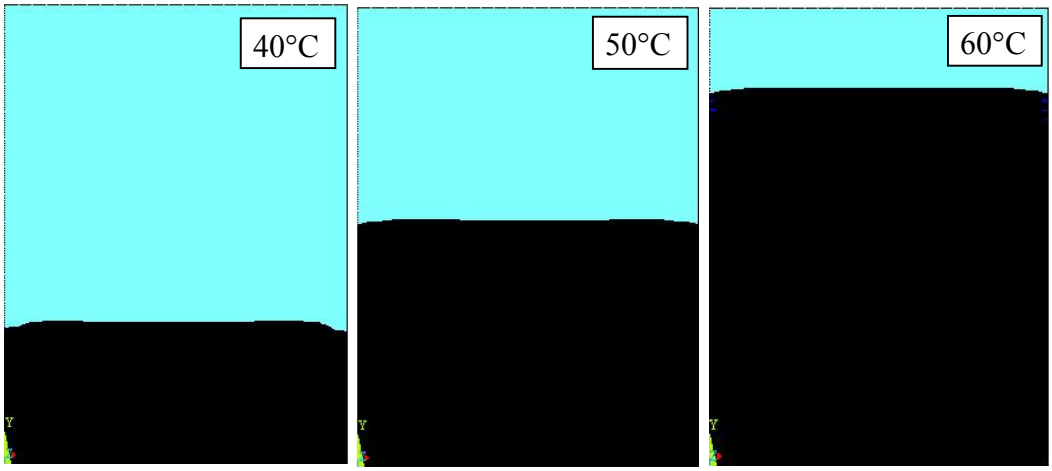

Figure 7.19 Flow front distribution for different temperatures (gap height: 85 μm, filling time: 60 s).

7.5 Conclusions

In this chapter, a parametric study was carried out to investigate the effect of the solder bump pattern (including bump pitch, solder bump diameter, and gap height) on the process variables (i.e., fluid flow front and fluid filling time). From this study, it was found that the design parameters can significantly affect filling time. The physics underlying these effects is the magnitude of the resistance to flow advancement. Among these design parameters, the most significant influence on the filling time is the critical clearance. When the clearance is below a critical value, the filling time begins to increase significantly due to the increase of the flow resistance. However, when clearance is above a critical value, the influence of clearance on the filling time becomes

small. The critical clearance can provide a bound below which the solder bump resistance should be considered. Furthermore, the temperature of the underfill material has a significant effect on the process performance.

By means of dimensional analysis, an equation to calculate the dimensionless critical clearance, which is a function of the underfill material property and gap height, was proposed. The design criterion for a solder bump in flip-chip package should be $W^* > W^*_{critical}$. Based on this criterion, a simple yet effective design procedure can be implemented.

8 CONCLUSIONS AND FUTURE WORK

8.1 Overview

The underfill process is a very important step in the manufacture of the flip-chip package because of its great impact on the eventual reliability of the flip-chip package. The motivation for this study was based on the fact that there currently is a lack of satisfactory analytical models for predicting the underfill flow behavior in the flip-chip package. The analytical model is useful for package and process design optimization and to real-time process control. At present, with the current power of computing, numerical simulation using the finite element method for complete filling of one chip could take from a few hours to a few days (Gordon et al., 1999). On the other hand, there are two problems that hinder the development of the analytical model. One is the complexity of the governing equations, due to the non-Newtonian behavior exhibited by the underfill material. The other is the presence of solder bumps in the micro-cavity, inclusion of which leads to some additional complexity in the governing equation.

Although numerical modeling appears to offer a better simulation strategy, none of the numerical models available are satisfactory for the prediction of flip-chip underfill flow. Numerical simulation based on powerful commercial software packages require

excessive computation time. Furthermore, the surface tension-driven flow problem is not explicitly modeled in the current commercial software package. As such, the commercial dedicated software package does not offer a reliable solution.

The goal of the study presented in this thesis was to advance the modeling and simulation techniques for the underfill flow process in the flip-chip package. Two streams of studies were conducted: one towards an analytical model, and the other towards a numerical model.

As a first step, a literature review on the Washburn model and the Han-Wang model was given in Chapter 1. Next, several viscosity constitutive equations describing non-Newtonian fluids in electronics packaging were presented in Chapter 2. Specifically, the rheological behavior of a typical underfill material FP4530 used in flip-chip packaging, including the dependency of its viscosity on shear rate and temperature, was investigated experimentally. The experimental results were compared with predictions using the power-law model, which indicated a good agreement between them.

The transient behavior of the underfill flow and the effect of the solder bump resistance on fluid flow were investigated in Chapter 3. The purpose of this investigation was to confirm whether the transient behavior could be neglected in the modeling of the underfill flow. Another purpose was to examine the adequacy of neglecting the solder bump resistance in the work done by Han and Wang (1997a). The Washburn model,

which takes the Newtonian fluid constitutive equation for the non-Newtonian fluid, was employed in all these studies without loss of generality.

A further study focused on the development of analytical models (Chapter 4). The power-law constitutive equation was used to describe the non-Newtonian viscous behavior of the underfill material because it is relatively simple yet very general, which could then lead to some closed-form solutions. This is an important departure point between the work of this thesis and the Han-Wang model (Han and Wang, 1997a). Subsequently, two models (Model I and Model II) were derived. Model I was for predicting the underfill flow behavior between two parallel plates driven by capillary action, and Model II was for predicting the flow behavior of underfill flow in the flip-chip package (i.e., two parallel plates with solder bumps) driven by capillary action.

The experimental study was described in Chapter 5. In this chapter, experimental methods were developed for the purpose of testing the Washburn model and verifying Model I and Model II. The purpose of the experiment was achieved.

However, because the analytical model cannot provide specific information regarding the underfill fluid distribution, it was necessary to develop the numerical modeling which was presented in Chapter 6. A numerical model was developed for investigation of the two-dimensional flow front distribution based on a commercial software package (ANSYS). With this model, simulation of the “racing effect” generated by the “wicking effect” on the shape of the flow front was demonstrated. The use of ANSYS for the

problem concerned was not straightforward. The principal difficulty was in representing the pressure boundary condition, which could not be implemented because of the resistance caused by the parallel plates in a two-dimensional model geometry. A time-dependent velocity boundary condition treatment was proposed at the inlet to deal with the effect of flow resistance caused by the parallel plates. The numerical simulation results were compared with both the analytical and experimental results. Based on the numerical results it was demonstrated that the "racing effect" was induced by the edge size. The larger the edge size, the stronger the racing effect and the less uniform the distribution of fluid at the flow front.

For the purpose of design optimization of the flip-chip package, a parameter analysis study was carried out in Chapter 7 to understand the effect of the solder bump pattern (including bump pitch, solder bump diameter, and gap height) on the performance variables (i.e., flow front, fluid distribution, and filling time). The parameter analysis introduced the notion of a critical clearance. An effort was made to develop a dimensionless critical clearance index $W^*_{critical}$, which is a function of the material property and the gap height.

The study presented in this thesis has resulted in the following conclusions:

(1) The power-law constitutive equation is adequate for describing the non-Newtonian property of the underfill material in flip-chip packaging.

(2) For the underfill flow driven by capillary action in a micro-cavity, the transient behavior can be safely neglected.

(3) The solder bump resistance has significant effect on the underfill flow, and it should not be neglected in the underfill flow analysis in flip-chip packaging.

(4) The Han-Wang model (their analytical model) is not adequate for describing the underfill flow of non-Newtonian fluids in flip-chip packaging.

(5) The Washburn model can give a good prediction for a Newtonian fluid in the parallel-plate underfill flow, but it is not applicable to a non-Newtonian fluid.

(6) Model I developed in this thesis is much better than the Washburn model for predicting the characteristics of the underfill flow between two parallel plates. The fluid filling time calculated using Model I agrees well with the measured result, and was shown to be excellent for describing the non-Newtonian underfill flow for the geometry of two parallel plates.

(7) Model II developed in this thesis is much better than both the Washburn model and the improved Washburn model for predicting the characteristics of the underfill flow in flip-chip packaging. The fluid filling time calculated using Model II agrees well with the measured result, and was shown to be excellent for describing the non-Newtonian underfill flow for the geometry of the flip-chip package.

(8) The numerical model formulated using the commercial package ANSYS can give a good prediction for the underfill flow between two parallel plates, and can predict the "racing effect" which is induced by the edge size.

(9) Among the design parameters, the most significant influence on the filling time is the critical clearance, which provides a bound below which the solder bump resistance should be seriously considered.

8.2 Contributions

The general contribution of the research described in this thesis is to suggest a paradigm shift from the Washburn model to the power-law constitutive equation for the non-Newtonian fluid in flip-chip packaging. Representative use of the Washburn model is the work done at Cornell University by Han and Wang (1997a), including the Washburn model with consideration of dynamic contact angle. The move for making this paradigm shift was driven by two observations. The first observation was that the introduction of dynamic contact angle in the context of the flip-chip underfill flow was not adequate. The second observation was that there is still some discrepancy between the simulation result using the Han and Wang model and the measured results. Although such discrepancy may be attributed to the neglect of the resistance of the solder bump (in their analytical model), some other more fundamental causes for the discrepancy are speculated. Specific contributions of the study presented in this thesis are given as follows:

(1) For the time-independent non-Newtonian fluid in the context of the flip-chip underfill process, the power-law constitutive equation is experimentally shown to be adequate.

(2) An experimental set-up for the underfill flow between two parallel plates was developed. A Newtonian fluid (Brookfield 5000) was used to examine the fluid characterization of the traditionally used Washburn model (Washburn, 1921) and to confirm the feasibility of the experimental set-up. The experimental results agree

well with the results predicted by the Washburn model.

(3) An unsteady model of underfill flow was developed to investigate transient effects on capillary underfill flow with respect to the constitutive equation of a Newtonian fluid. It was found that with a decrease in cavity thickness and an increase in viscosity, the transient influence on the flow process and the filling time becomes very small and can be safely neglected.

(4) A lumped parameter model was developed by considering the influence of the resistance caused by the solder bump and the dynamic contact angle. In this model, the dynamic contact angle was used to consider the non-Newtonian effect of polymer materials. The developed model was verified with the experimental data reported by Han and Wang (1997a) and can adequately predict the underfill flow in the flip-chip package.

(5) A lumped parameter analytical model, Model I, was developed for predicting the underfill flow behaviour between two parallel plates driven by capillary action. This model was verified by means of the measured results and was shown to be capable of describing the underfill flow of non-Newtonian fluids.

(6) A lumped parameter analytical model, Model II, was developed for predicting the flow behaviour of underfill flow in flip-chip packaging including the solder bump driven by the capillary action. This model was verified by the experiments.

(7) A numerical simulation model using the commercial software package ANSYS was developed to investigate the flow front distribution on a two-dimensional plane for the underfill flow process. In this model, a time-dependent velocity boundary condition treatment was proposed in place of the pressure boundary condition at the

inlet to deal with the effect of flow resistance exerted by the parallel plates. The simulation results were compared to both the experimental and analytical results. It was found that this numerical model can adequately predict the underfill flow between two parallel plates and the underfill flow in flip-chip packaging. It is noted that the numerical model developed here is superior to both the numerical model reported by Nguyen et al. (1999) and Han and Wang (1997a) for the prediction of flip-chip underfill flow.

(8) The notion of a critical clearance was proposed, and subsequently, the equation to calculate the critical clearance was developed. The usefulness of this notion in the flip-chip package design was demonstrated.

8.3 Future Work

There are a number of issues that arise from the present research work. The following are recommendations for future work:

(1) Development of a lumped parameter analytical model which adopts with a time-dependent viscosity constitutive equation to describe the underfill flow characteristics in flip-chip packaging.

In the study presented in this thesis, it was found that all currently available commercial underfill materials contain a curing catalyst. Although the material system starts to react at a flow temperature of 80°C and the viscosity begins to increase with flow time, the

viscosity nonetheless begins to change slowly at the ordinary temperature environment as soon as it is taken out from storage in the refrigerator (in which the temperature is below -40 °C). Therefore, it is necessary to investigate the influence of time on the characterization of viscosity variation in a normal temperature environment.

(2) Further numerical simulation for investigation of flow front distribution with an appropriate software package

In the study presented in this thesis, in order to use the ANSYS software package to investigate the flow front distribution in two-dimensional flows, a time-dependent velocity function boundary condition treatment was proposed. Although the developed numerical modeling method can give a good prediction for the underfill flow between two parallel plates, both for the filling time and for the flow front distribution, the predicted flow front shape did not agree well with the measured flow front shape in the flip-chip underfill flow process. This is because the actual capillary flow is driven by surface tension, which is related to the micro-cavity size between two parallel plates and the clearance between two solder bumps. The ANSYS software package does not provide the capability of modeling the capillary flow. Therefore, for a more realistic simulation, a software that can simulate the underfill flow driven by surface tension is required.

(3) Analysis of different viscosity constitutive equations for the underfill flow in flip-chip packaging.

In this study, the power-law viscosity constitutive equation was demonstrated to be an appropriate model for describing the rheological behaviour of encapsulant material FP4530. However, it should be noted that with the development of new fast-flow, fast-cure materials, especially the time-dependant and/or the viscoelastic underfill materials, the power-law model may not be capable of adequately describing the rheological behaviour of such underfill materials. New models would be required for describing the underfill flow characteristics for these new materials.

(4) Extension of the present study to include the injection filling method

The main concern regarding the dispensing filling method is that the filling process is slow, although with the development of fast-flow underfill materials, it is possible for the currently used encapsulant material to underfill a common-size chip (6 mm x 6 mm) in less than 40 seconds. The desire to pursue high throughput and low cost has provoked manufactures' interest in the development of methods that will further reduce filling time. This problem will become even more of a challenge for such future developments as increasing both chip size and solder bump density. To reduce filling time and increase throughput, injection filling is a possible direction. The two main problems existing in injection filling are the lack of reliability due to the air void that accompanies the injection process, and the complexity generated in the injection mould application.

REFERENCES

Adam, N. K., 1930, *Physics and Chemistry of Surfaces*, Oxford at the Claredon Press.

Adamson, A. W., 1990, *Physical Chemistry of Surfaces*, John Wiley & Sons, Inc., New York.

ANSI, 1998, American National Standards Institute/ American Society of Mechanical Engineers, *Test Uncertainty*, PTC 19.1-1998, ASME, New York.

Arpaci, Vedat S., 1966, *Conduction Heat Transfer*, Addison-Wesley Publishing Company, New York.

Astarita, G. and Marrucci, G., 1974, *Principles of Non-Newtonian Fluid Mechanics*, McGraw-Hill, New York.

ASM, 2000, ASM Assembly Automation Ltd., 2000, *DS500 Precision Dispensing System Operation Manual*, New York.

Barnes, H.A., Hutton, J.F., and Walters, K., 1989, *An Introduction to Rheology*, Elsevier Science Publisher B.V., New York.

Benezech, T. and Maingonnat, J.F., 1994, "Characterization of the Rheological Properties of Yougurt - A Review," *Journal of Food Engineering*, Vol. 21, pp. 447-472.

Bird, R. B., Stewart, W. E., and Lightfoot, E. N., 1960, *Transport Phenomena*, John Wiley & Sons, New York.

Brookfield Engineering Laboratories, INC. (USA), *Brookfield Cone/Plate Viscometer and Rheocalc for Windows: Operating Instructions*.

Chai, Kevin and Wu, Eddy, 2001, "The Underfill Processing Technologies for Flip Chip Packaging," *First International IEEE Conference on Polymers and Adhesives in*

*Microelectronics and Photonics: Incorporating POLY, PEP and Adhesives in Electronics***,** pp.119-123, Potsdam, Germany.

Chai, Kevin, Wu, Eddy, Hsieh, Roger, and Tong, J.Y., 2002,"Challenge of Flip Chip Encapsulation Technologies," *Proceedings of SPIE - The International Society for Optical Engineering***,** Vol. 4931, pp. 733-737, Denver, CO, USA.

Chen, X. B., 2002, "Modeling and Off-line Control of Fluid Dispensing for Electronics Packaging," Ph.D. dissertation, University of Saskatchewan, Saskatoon, SK, Canada.

Chhabra, R.P. and Richarson, J.F., 1999; *Non-Newtonian Flow in the Process Industries*, Butterworth-Heinemann.

Chiang, H. H., Hieber, C.A., and Wang, K. K., 1991, "A United Simulation of the Filling and Post-filling stages in Injection Modeling Part I: Formation," *Polymer Engineering and Science***,** Vol. 31, No.2 pp. 118-124.

Coleman, H.W. and Steele, W.G., 1999, *Experimentation and Uncertainty Analysis for Engineers*, John Wiley & Sons, Inc., New York.

Cross, M.M., *Journal of Colloid Science*, 1965, Vol. 20, pp.420.

Dullien, F.A.L., 1992, *Porous Media Fluid Transport and Pore Structure*, Second edition, ACADEMIC PRESS, INC., Harcourt Brace Jovanovich, Publishers, New York.

Erickson, D., Lu, F., Li, D., White, A., and Gao, J., 2002, "An Experimental Investigation into The Dimension Sensitive Viscosity of Polymer Containing Lubricant Oils in Micro-Channels," *Experimental Thermal and Fluid Science*, pp. 623-630.

Erickson, D., Li, D. and Park, C.B., 2002, "Numerical Simulations of Capillary-Driven Flows in Non-uniform Cross-Sectional Capillaries," *Journal of Colloid and Interface Science*, Vol. 250, pp. 422-430.

Eringen, A.C. and Okada, K., 1995, "A Lubrication Theory for Fluids with

Microstructure," *International Journal of Engineering Science*, Vol. 33, No. 15, pp. 2297-2308.

Faith A. Morrison, 2001, *Understanding Rheology*, Oxford University Press, New York.

Fine, P., Cobb, B., and Nguyen L., 2000, "Flip-Chip Underfill Flow Characteristics and Prediction," *IEEE Transactions on Components and Packaging Technology*, Vol. 23, No.3, pp. 420-427.

Frear, D.R., Jang, J.W., Lin, J.K., and Zhang, C., 2001, "Pb-free solders for flip-chip interconnects," *JOM*, v 53, n 6, June, 2001, p 28-32+38.

Gamota, D.R. and Melton, C.M., 1996, "Advanced Encapsulant Materials Systems for Flip Chip on Board Assemblies: I. Encapsulant Materials with Improved Manufacturing Properties; II. Materuials to Integrate the Reflow and Underfilling Processes," *IEEE/CPMT International Electronics Manufacturing Technology Symposium*, Austin, TX, pp. 1-9.

Gertach A., Lambach H., and Seidel D., 1999, "Propagation of Adhesives in Joints during Capillary Adhesive Bonding of Micro-components," *Microsystems Technologies,* Vol. 6, pp. 19-22.

Giesler, J., O'Malley, G., Williams, M., and Machuga, S., 1994, "Flip Chip on Board Connection Technology: Process Characterization and Reliability," *IEEE Transactions on Components, Packaging and Manufacturing Technology*, Vol. 17, No.3, pp. 256-263.

Gordon, M.H., Ni, G., Schmidt, W.F., and Selvam, R.P., 1999, "A Capillary-Driven Underfill Encapsulation Process," *Advanced Packaging,* Vol. 8, pp. 34-37.

Guo, Y., Lehmann, G.L., Driscoll, T., and Cotts, E.J., 1999, "A Model of the Underfill Flow Process: Particle Distribution Effects," *Proceedings of the 1999 49th Electronic Components and Technology Conference (ECTC)*, San Diego, CA, USA, pp. 71-76.

Han, S. and Wang, K. K., 1997a, "Analysis of the Flow of Encapsulant during Underfill

Encapsulation of Flip-Chips," *IEEE Transactions on Components, Packaging, and Manufacturing Technology*, Part B, Vol. 20, No.4 pp. 424-433.

Han, S. and Wang, K. K., 1997b, "Study on the Pressurized Underfill Encapsulation of Flip-Chips," *IEEE Transactions on Components, Packaging, and Manufacturing Technology*, Part B, Vol. 20, No.4 pp. 434-442.

Han, S. and Wang, K. K., 2000a, "Flow Analysis in a Chip Cavity during Semiconductor Encapsulation," *Journal of Electronic Packaging*, Vol. 122, pp. 160-167.

Han, S. and Wang, K. K., 2000b, "Integrated Flow Analysis during Filling and Post-Filling Stage of Semiconductor Encapsulation," *Journal of Electronic Packaging*, Vol. 122, pp. 20-27.

He, Yi, Moreira, B.E., Overson, A., Nakamura, S.H, Brider, C., and Briscoe, J.F., 2000, "Thermal Characterization of an Epoxy-Based Underfill Material for Flip Chip Packaging," *Thermochimica Acta*, Vol.357-358, pp. 1-8.

He, Yi, 2001, "DSC and DEA Studies of Underfill Curing Kinetics," *Thermochimica Acta*, Vol.367-368, pp. 101-106.

Herschel, W.H. and Bulkley, R., 1926, "Konsistenzmessungen von Gummi-Benzollosungen," *Kolloid Z.* Vol. 39, pp. 290-300.

Hieber, C. A. and Shen, S. F., 1980, "A Finite-Element/Finite-Difference Simulation of Injection-Molding Filling Process," *Journal of Non-Newtonian Fluid Mechanics*, Vol. 7, pp. 1-32.

Hirt, C.W. and Nichols, B.D., 1981, "Volume of Fluid (VOF) Method for the Dynamics of Free Boundary," *Journal of Computational Physics*, Vol. 39, pp. 201-225.

Hocking, L.M. and Rivers, A.D., 1982, "The Spreading of a Drop by Capillary Action," *Journal of Fluid Mechanics*, Vol. 121, pp. 425-442.

Holdsworth, S. D. 1993, "Rhelogical Models Used for the Prediction of the Flow Properties of Food Products: a Literature Review," *Trans. Institution of Chemical Engineering,* Vol. 71(C3), pp. 139-179.

Hosokawa, Kazuo, Fujii, Teruo, and Endo, Isao, 1999, "Droplet-Based Nano/Picoliter Mixer Using Hydrophobic Microcapillary Vent," *Proceedings of the IEEE Micro Electro Mechanical Systems (MEMS)*, pp. 388-393, Orlando, FL, USA.

Hsu, D.T., Kim, H.K., Shi, F.G., Tong, H.Y., Chungpaibonpatana, S., Davidson, C., and Adams, J.M., 2000, "Curing Kinetics and Optimal Cure Schedules for Underfill Materials," *Microelectronics Journal*, Vol. 31, pp. 271-275.

Hsu, Tai-Ran, 2002**,** *MEMS and Microsystems: Design and* M*anufacture,* McGraw-Hill, Boston.

Huang, C.Y., 2002, "The Investigation of the Capillary Flow of Underfill Materials," *Microelectronics International*, v 19, n 1, pp. 23-29.

Isayev, A.I., and Hieber, C. A., 1980, "Toward a Viscoelastic Modeling of the Injection Molding of Polymers," *Rheologica Acta*, Vol. 19, No. 2, pp. 168-182.

Karkanas, P.I and Partridge, I.K., 1996, "Modeling the Cure of a Commercial Epoxy Resin for Applications in Resin Transfer Moulding," *Polymer International*, Vol. 41, pp. 183-196.

Kim, D.S., Lee, K.C., and Kwon, T.H., 2002, "Micro-Channel Filling Flow Considering Surface tension Effect," *Journal of Micromechanics and Microengineering*, Vol. 12, pp. 236-246.

Larson, R. G., 1999, *The Structure and Rheology of Complex Fluids*, Oxford University Press, New York.

Lau, (Ed.), J.H., 1995, *Flip Chip Technologies*, McGraw-Hill, New York.

Lau, John H., and Chang, Chris, 1999, "Characterization of Underfill Materials for Functional Solder Bumped Flip Chips on Board Applications," *IEEE Transactions on Components and Packaging Technology*, Vol. 22, No.1, pp. 111-119.

Lau, John H., and Chang, Chris, 2002, "Characteristics and Reliability of Fast-Flow, Snap-Cure, and Reworkable Underfills for Solder Bumped Flip Chip on Low-Cost Substrates," *IEEE Transactions on Electronics Packaging Manufacturing*, Vol. 25, No.3, pp. 231-239.

Lehmann, G., Maria, A., Lee, Pin-Chou, and Cotts, E.J., 1997, "Modeling the Underfill Flow Process," *Proceedings of the Technical Program, Conference on Surface Mount Technology, San Jose, CA*, pp. 340-350.

Levenspiel, O., 1998, *Engineering Flow and Heat Exchange*, Plenum, New York.

Luo, Sshijian, Vidal, Michael, and Wong, C.P., 2000, "Study on Surface Tension and Adhesion in Electronic Packaging," *IEEE Electronic Components and Technology Conference*, pp. 586-591.

Machuga, S.C., Lindsey, S.E., Moore, K.D., and Skipor, A.F., 1992, "Encapsulation of Flip Chip Structures," *IEEE Compon. Hybrids Mfg. Tech. Int. Mfg. Tech. Symp.,* Baltimore, MD, pp. 53-58.

Macosko, C. W., 1994, *Rheology: Principles, Measurements, and Applications*, VCH Publishers, Inc., New York.

Madou, M.J., 2002, *Fundamentals of Microfabrication- The Science of Miniaturization*, CRC Press, New York.

Morrison, Faith A., 2001, *Understanding Rheology*, Oxford University Press, Oxford.

Newman, S., 1968, "Kinetics of Wetting of Surfaces by Polymer: Capillary Flow," *Journal of Colloid and Interface Science*, Vol. 26, pp. 209-213.

Nguyen L., Quentin C., Fine, P., Cobb, B., Bayyuk, S., Yang, H., and Bidstrup-Allen, S.A., 1999, "Underfill of Flip-Chip on Laminate: Simulation and Validation," *IEEE Transactions on Components and Packaging Technology*, Vol. 22, No.2, pp. 168-176.

O'Malley, G., Giesler, J., and Machuga, S., 1994, "The Importance of Material Selection for Flip Chip Assemblies," *IEEE Transactions on Components, Packaging, and Manufacturing Technology*, Part B., Vol. 17, No.3, pp. 248-255.

Pantuso, Daniel, Jiang Lei, Shankar, Sadasivan, and Skokov, Sergei, 2003, "A FEM/VOF Hybrid Formation for Underfill Encapsulation Modeling," *Computers & Structures*, Vol. 81, pp. 879-885.

Pascarella N.W., and Baldin, D.F., 1998, "Compression Flow Modeling of Undrefill Encapsulation for Low Cost Flip-Chip Assembly," *IEEE Transactions on Components, Packaging, and Manufacturing Technology*, Part C., Vol. 21, No.4, pp. 325-335.

Pepper, Darrell W. and Heinrich, Juan C., 1992, *The Finite Element Method: Basic Concepts and Applications*, Hemisphere Publishing Corporation, Washington.

Razban, A. and Davies, B.L., 1995, "Analytical Modeling of the Automated Dispensing of Adhesive Material," *Journal of Adhesion Science Technology*, Vol. 9, pp. 1435-1450.

Reddy, J.N., 1993, *An Introduction to the Finite Element Method*, McGraw-Hill, Inc., New York.

Reddy, J.N. and Gartling, D.K., 2001, *The Finite Element Method in Heat Transfer and Fluid Dynamics*, CRC Press, New York.

Roberson, J. A. and Crowe, C. T., 1997, *Engineering Fluid Mechanics*, John Wiley & Sons Inc., New York.

Sabry, Mohamad-Nabil, 2000, "Scale Effects on Fluid Flow and Heat Transfer in Microchannels," *IEEE Transactions on Components and Packaging Technologies*, Vol. 23 No.3, pp. 562-567.

Schlichting, Hermann, 1979, *Boundary-layer theory*, McGraw-Hill, Toronto.

Schonhorn, H., Frisch, H., and Kwei, T. K., 1966, "Kinetics of Wetting of Surfaces by Polymer Melts," *Journal of Applied Physics*, Vol. 37, pp. 4967-4973.

Schwiebert, M. K. and Leong, W. H., 1996, "Undrefill Flow as Viscous Flow Between Parallel Plates Drvien by Capillary Action," *IEEE Transactions on Components, Packaging*, and *Manufacturing Technology*, Part C., Vol. 19, No.12 pp. 133-137.

Shen, Y.K., Ye, T.W., Chen, S.L., Yin, C.H., and Song, W.D., 2001, "Study on Mould Flow Analysis of Flip Chip Package," *International Communications in Heat and Mass Transfer*, Vol. 28, pp. 943-952.

Shi, Daqing Max and Carbin, James W., 1996, "Advances in Flip-chip Underfill Flow and Cure Rates and Their Enhancement of Manufacturing Processes and Component Reliability," *Proceedings - Electronic Components and Technology Conference*, pp. 1025-1031.

Skelland, A.H.P., 1967, *Non-Newtonian Flow and Heat transfer*, John Wiley & Sons, Inc., New York.

Suryanarayana, Darbha., Hsiao, Richard, Gall, Tomas P., and McCreary, Jack M., 1991, "Enhancement of Flip Chip Fatigue Life by Encapsulation," *IEEE Transactions on Component, Hybrids and Manufacturing Manufacture Technology*, Vol. 14, No.1, pp. 218-223.

Suryanarayana, D., Wu, T.Y., and Varcoe, J.A., 1993, "Encapsulants Used in Flip Chip Packages," *IEEE Transactions on Components and Hybrids Manufacture Technology*, Vol. 16, No.8, pp. 858-862.

Tate, T., 1864, *Phil .Mag.*, 27, 176.

Wang, Jinlin, 2002, "Underfill of Flip-Chip on Organic Substrate: Viscosity, Surface tension, and Contact Angle," *Microelectronics Reliability*, Vol. 42, pp. 293-299.

Washburn, E. W., 1921, "The Dynamics of Capillary Flow," *Physical Review*, Vol. 17, pp. 273-283.

Weatherburn, C. E., 1947, *Differential Geometry*, Vol. 1, Cambridge University Press, London.

White, Frank M., 1986, *Fluid Mechanics*, McGraw-Hill Book Company, New York.

Wong, C.P. and Wong, M.M., 1999, "Recent Advances in Plastic Packaging of Flip-Chip and Multichip Modules (MCM) of Microelectronics," *IEEE Transactions on Components and Packaging Technology*, Vol. 22, No.1, pp. 21-25.

Wong, C.P., Vincent, M. B., and Shi, S., 1998a, "Fast-Flow Underfill Encapsulant: Flow Rate and Coefficient of Thermal Expansion," *IEEE Transactions on Components, Packaging, and Manufacturing Technology*, Part A, Vol. 21, No.12 pp. 360-363.

Wong, C. P., Shi, S. H., and Jefferson, G., 1998b, "High Performance No-flow Underfills for Flip-chip Applications: Material Characterization," *IEEE Trans. Comp., Packag., Manufact. Technol. A*, vol. 21, p. 450, Sept. 1998.

Wong, C.P., Shi, S. H., and Jefferson, G., 1997, "High performance no flow underfills for low-cost flip-chip applications," in *Proc. 47th Electronic Components Technology Conf.*, San Jose, CA, 1997, p. 850.

Yao, D. and Kim, B., 2002, "Simulation of the Filling Process in Micro-Channels for Polymeric Materials," *Journal of Micromechanics and Microengineering*, Vol. 12, pp. 604-610.

Young, Wen-Bin and Yang, Wen-Lin, 2002, "Underfill Viscous Flow between Parallel Plates and Solder Bumps," *IEEE Transactions on Components and Packaging, and Technology*, Vol. 25, No.4, pp. 695-700.

Zhang, Zhuqing and Wong, C.P., 2002, "Assembly of Lead-free Bumped Flip Chip with

No-flow Underfills," *IEEE Transactions on Electronics Packaging Manufacturing*, Vol. 25, No.2, pp. 113-119.

Zhang, Zhuqing and Wong, C.P., 2004, "Recent Advances in Flip-Chip Underfill: Materials, Process, and Reliability," *IEEE Transactions on Advanced Packaging*, Vol. 27, No.3, pp. 515-524.

APPENDIX A: THE GOVERNING EQUATIONS (Bird et al. 1960)

A.1 Continuity equation

Rectangular coordinate:

$$\frac{\partial \rho}{\partial t} + \frac{\partial}{\partial x}(\rho v_x) + \frac{\partial}{\partial y}(\rho v_y) + \frac{\partial}{\partial z}(\rho v_z) = 0 \tag{A-1}$$

Cylindrical coordinate:

$$\frac{\partial \rho}{\partial t} + \frac{1}{r}\frac{\partial}{\partial r}(\rho r v_r) + \frac{1}{r}\frac{\partial}{\partial \theta}(\rho v_\theta) + \frac{\partial}{\partial z}(\rho v_z) = 0 \tag{A-2}$$

A.2 Momentum equation

Rectangular coordinates:

X-component:

$$\rho\left(\frac{\partial v_x}{\partial t} + v_x\frac{\partial v_x}{\partial x} + v_y\frac{\partial v_x}{\partial y} + v_z\frac{\partial v_x}{\partial z}\right) = -\frac{\partial p}{\partial x} - \left(\frac{\partial \tau_{xx}}{\partial x} + \frac{\partial \tau_{yx}}{\partial y} + \frac{\partial \tau_{zx}}{\partial z}\right) + \rho g_x \tag{A-3}$$

Y-component:

$$\rho\left(\frac{\partial v_y}{\partial t} + v_x\frac{\partial v_y}{\partial x} + v_y\frac{\partial v_y}{\partial y} + v_z\frac{\partial v_y}{\partial z}\right) = -\frac{\partial p}{\partial y} - \left(\frac{\partial \tau_{xy}}{\partial x} + \frac{\partial \tau_{yy}}{\partial y} + \frac{\partial \tau_{zy}}{\partial z}\right) + \rho g_y \tag{A-4}$$

Z-component:

$$\rho\left(\frac{\partial v_z}{\partial t}+v_x\frac{\partial v_z}{\partial x}+v_y\frac{\partial v_z}{\partial y}+v_z\frac{\partial v_z}{\partial z}\right)=-\frac{\partial p}{\partial z}-\left(\frac{\partial \tau_{xz}}{\partial x}+\frac{\partial \tau_{yz}}{\partial y}+\frac{\partial \tau_{zz}}{\partial z}\right)+\rho g_z \tag{A-5}$$

In terms of velocity gradients for a Newtonian fluid with constant ρ and μ:

X-component:

$$\rho\left(\frac{\partial v_x}{\partial t}+v_x\frac{\partial v_x}{\partial x}+v_y\frac{\partial v_x}{\partial y}+v_z\frac{\partial v_x}{\partial z}\right)=-\frac{\partial p}{\partial x}+\mu\left(\frac{\partial^2 v_x}{\partial x^2}+\frac{\partial^2 v_x}{\partial y^2}+\frac{\partial^2 v_x}{\partial z^2}\right)+\rho g_x \tag{A-6}$$

Y-component:

$$\rho\left(\frac{\partial v_y}{\partial t}+v_x\frac{\partial v_y}{\partial x}+v_y\frac{\partial v_y}{\partial y}+v_z\frac{\partial v_y}{\partial z}\right)=-\frac{\partial p}{\partial y}+\mu\left(\frac{\partial^2 v_y}{\partial x^2}+\frac{\partial^2 v_y}{\partial y^2}+\frac{\partial^2 v_y}{\partial z^2}\right)+\rho g_y \tag{A-7}$$

Z-component:

$$\rho\left(\frac{\partial v_z}{\partial t}+v_x\frac{\partial v_z}{\partial x}+v_y\frac{\partial v_z}{\partial y}+v_z\frac{\partial v_z}{\partial z}\right)=-\frac{\partial p}{\partial z}+\mu\left(\frac{\partial^2 v_z}{\partial x^2}+\frac{\partial^2 v_z}{\partial y^2}+\frac{\partial^2 v_z}{\partial z^2}\right)+\rho g_z \tag{A-8}$$

Cylindrical coordinates

R-component:

$$\begin{aligned}&\rho\left(\frac{\partial v_r}{\partial t}+v_r\frac{\partial v_r}{\partial r}+\frac{v_\theta}{r}\frac{\partial v_r}{\partial \theta}-\frac{v_\theta^2}{r}+v_z\frac{\partial v_r}{\partial z}\right)\\&=-\frac{\partial p}{\partial r}-\left(\frac{1}{r}\frac{\partial}{\partial r}(r\tau_{rr})+\frac{1}{r}\frac{\partial \tau_{r\theta}}{\partial \theta}-\frac{\tau_{\theta\theta}}{r}+\frac{\partial \tau_{zr}}{\partial z}\right)+\rho g_r\end{aligned} \tag{A-9}$$

θ-component:

$$\rho\left(\frac{\partial v_\theta}{\partial t}+v_r\frac{\partial v_\theta}{\partial r}+\frac{v_\theta}{r}\frac{\partial v_\theta}{\partial \theta}+\frac{v_r v_\theta}{r}+v_z\frac{\partial v_\theta}{\partial z}\right)$$
$$=-\frac{1}{r}\frac{\partial p}{\partial \theta}-\left(\frac{1}{r^2}\frac{\partial}{\partial r}(r^2\tau_{r\theta})+\frac{1}{r}\frac{\partial \tau_{\theta\theta}}{\partial \theta}+\frac{\partial \tau_{\theta z}}{\partial z}\right)+\rho g_\theta \quad \text{(A-10)}$$

Z-component:

$$\rho\left(\frac{\partial v_z}{\partial t}+v_r\frac{\partial v_z}{\partial r}+\frac{v_\theta}{r}\frac{\partial v_z}{\partial \theta}+v_z\frac{\partial v_z}{\partial z}\right)$$
$$=-\frac{\partial p}{\partial z}-\left(\frac{1}{r}\frac{\partial}{\partial r}(r\tau_{rz})+\frac{1}{r}\frac{\partial \tau_{\theta z}}{\partial \theta}+\frac{\partial \tau_{zz}}{\partial z}\right)+\rho g_z \quad \text{(A-11)}$$

In terms of velocity gradients for a Newtonian fluid with constant ρ and μ:

R-component:

$$\rho\left(\frac{\partial v_r}{\partial t}+v_r\frac{\partial v_r}{\partial r}+\frac{v_\theta}{r}\frac{\partial v_r}{\partial \theta}-\frac{v_\theta^2}{r}+v_z\frac{\partial v_r}{\partial z}\right)$$
$$=-\frac{\partial p}{\partial r}+\mu\left[\frac{\partial}{\partial r}\left(\frac{1}{r}\frac{\partial}{\partial r}(rv_r)\right)+\frac{1}{r^2}\frac{\partial^2 v_r}{\partial \theta^2}-\frac{2}{r^2}\frac{\partial v_\theta}{\partial \theta}+\frac{\partial^2 v_r}{\partial z^2}\right]+\rho g_r \quad \text{(A-12)}$$

θ-component:

$$\rho\left(\frac{\partial v_\theta}{\partial t}+v_r\frac{\partial v_\theta}{\partial r}+\frac{v_\theta}{r}\frac{\partial v_\theta}{\partial \theta}+\frac{v_r v_\theta}{r}+v_z\frac{\partial v_\theta}{\partial z}\right)$$
$$=-\frac{1}{r}\frac{\partial p}{\partial \theta}+\mu\left[\frac{\partial}{\partial r}\left(\frac{1}{r}\frac{\partial}{\partial r}(rv_\theta)\right)+\frac{1}{r^2}\frac{\partial^2 v_\theta}{\partial \theta^2}+\frac{2}{r^2}\frac{\partial v_r}{\partial \theta}+\frac{\partial^2 v_\theta}{\partial z^2}\right]+\rho g_\theta \quad \text{(A-13)}$$

Z-component:

$$\rho\left(\frac{\partial v_z}{\partial t}+v_r\frac{\partial v_z}{\partial r}+\frac{v_\theta}{r}\frac{\partial v_z}{\partial \theta}+v_z\frac{\partial v_z}{\partial z}\right)$$
$$=-\frac{\partial p}{\partial z}+\mu\left[\frac{1}{r}\frac{\partial}{\partial r}\left(r\frac{\partial v_z}{\partial r}\right)+\frac{1}{r^2}\frac{\partial^2 v_z}{\partial \theta^2}+\frac{\partial^2 v_z}{\partial z^2}\right]+\rho g_z \tag{A-14}$$

A.3 Energy equation

Rectangular coordinate:

$$\rho c_V\left(\frac{\partial T}{\partial t}+v_x\frac{\partial T}{\partial x}+v_y\frac{\partial T}{\partial y}+v_z\frac{\partial T}{\partial z}\right)$$
$$=-\left(\frac{\partial q_x}{\partial x}+\frac{\partial q_y}{\partial y}+\frac{\partial q_z}{\partial z}\right)-T\left(\frac{\partial p}{\partial T}\right)_\rho\left(\frac{\partial v_x}{\partial x}+\frac{\partial v_y}{\partial y}+\frac{\partial v_z}{\partial z}\right)-\left[\tau_{xx}\frac{\partial v_x}{\partial x}+\tau_{yy}\frac{\partial v_y}{\partial y}+\tau_{zz}\frac{\partial v_z}{\partial z}\right]$$
$$-\left[\tau_{xy}\left(\frac{\partial v_x}{\partial y}+\frac{\partial v_y}{\partial x}\right)+\tau_{xz}\left(\frac{\partial v_x}{\partial z}+\frac{\partial v_z}{\partial x}\right)+\tau_{yz}\left(\frac{\partial v_y}{\partial z}+\frac{\partial v_z}{\partial y}\right)\right] \tag{A-15}$$

Cylindrical coordinate:

$$\rho c_V\left(\frac{\partial T}{\partial t}+v_r\frac{\partial T}{\partial r}+\frac{v_\theta}{r}\frac{\partial T}{\partial \theta}+v_z\frac{\partial T}{\partial z}\right)$$
$$=-\left(\frac{1}{r}\frac{\partial}{\partial r}(rq_r)+\frac{1}{r}\frac{\partial q_\theta}{\partial \theta}+\frac{\partial q_z}{\partial z}\right)-T\left(\frac{\partial p}{\partial T}\right)_\rho\left(\frac{1}{r}\frac{\partial}{\partial r}(rv_r)+\frac{1}{r}\frac{\partial v_\theta}{\partial \theta}+\frac{\partial v_z}{\partial z}\right)$$
$$-\left[\tau_{rr}\frac{\partial v_r}{\partial r}+\tau_{\theta\theta}\frac{1}{r}\left(\frac{\partial v_\theta}{\partial \theta}+v_r\right)+\tau_{zz}\frac{\partial v_z}{\partial z}\right] \tag{A-16}$$
$$-\left[\tau_{r\theta}\left(r\frac{\partial}{\partial r}\left(\frac{v_\theta}{r}\right)+\frac{1}{r}\frac{\partial v_r}{\partial \theta}\right)+\tau_{rz}\left(\frac{\partial v_z}{\partial r}+\frac{\partial v_r}{\partial z}\right)+\tau_{\theta z}\left(\frac{1}{r}\frac{\partial v_z}{\partial \theta}+\frac{\partial v_\theta}{\partial z}\right)\right]$$

In terms of velocity gradients for a Newtonian fluid with constant ρ, μ and k:

Rectangular coordinate:

$$\begin{aligned}
&\rho c_V\left(\frac{\partial T}{\partial t}+v_x\frac{\partial T}{\partial x}+v_y\frac{\partial T}{\partial y}+v_z\frac{\partial T}{\partial z}\right)\\
&=k\left(\frac{\partial^2 T}{\partial x^2}+\frac{\partial^2 T}{\partial y^2}+\frac{\partial^2 T}{\partial z^2}\right)+2\mu\left[\left(\frac{\partial v_x}{\partial x}\right)^2+\left(\frac{\partial v_y}{\partial y}\right)^2+\left(\frac{\partial v_z}{\partial z}\right)^2\right]\\
&+\mu\left[\left(\frac{\partial v_x}{\partial y}+\frac{\partial v_y}{\partial x}\right)^2+\left(\frac{\partial v_x}{\partial z}+\frac{\partial v_z}{\partial x}\right)^2+\left(\frac{\partial v_y}{\partial z}+\frac{\partial v_z}{\partial y}\right)^2\right]
\end{aligned} \tag{A-17}$$

Cylindrical coordinate:

$$\begin{aligned}
&\rho c_V\left(\frac{\partial T}{\partial t}+v_r\frac{\partial T}{\partial r}+\frac{v_\theta}{r}\frac{\partial T}{\partial \theta}+v_z\frac{\partial T}{\partial z}\right)\\
&=k\left[\frac{1}{r}\frac{\partial}{\partial r}\left(r\frac{\partial T}{\partial r}\right)+\frac{1}{r^2}\frac{\partial^2 T}{\partial \theta^2}+\frac{\partial^2 T}{\partial z^2}\right]+2\mu\left\{\left(\frac{\partial v_r}{\partial r}\right)^2+\left[\frac{1}{r}\left(\frac{\partial v_\theta}{\partial \theta}+v_r\right)\right]^2+\left(\frac{\partial v_z}{\partial z}\right)^2\right\}\\
&+\mu\left\{\left(\frac{\partial v_\theta}{\partial z}+\frac{1}{r}\frac{\partial v_z}{\partial \theta}\right)^2+\left(\frac{\partial v_z}{\partial r}+\frac{\partial v_r}{\partial z}\right)^2+\left[\frac{1}{r}\frac{\partial v_r}{\partial \theta}+r\frac{\partial}{\partial r}\left(\frac{v_\theta}{r}\right)\right]^2\right\}
\end{aligned} \tag{A-18}$$

APPENDIX B: UNCERTAINTY ANALYSIS

B.1 General equations

The general equations for the uncertainty (U) and the result (y) are given by (Coleman et al. 1999; ANSI, 1998)

$$U(y) = t \cdot \sqrt{\left(\frac{B_y}{2}\right)^2 + (S_{\bar{X}})^2} \tag{B-1}$$

where t is the student's value at a specified confidence level with ν degrees of freedom. B_y is the bias error, occurred due to the systematic errors that remain constant throughout a test, and is given by

$$B_y^2 = \sum_{i=1}^{n} \left(\frac{\partial y}{\partial x_i} \cdot B_i\right)^2 \tag{B-2}$$

where $\partial y / \partial x_i$ is sensitivity coefficient, B_i is the bias error of parameter i. n is the number of individual readings, and $S_{\bar{X}}$ is the estimate of the standard deviation of the sample mean and is given by

$$S_{\bar{X}} = \frac{S_X}{\sqrt{N}} \tag{B-3}$$

S_X is the standard deviation of a sample of measurements and is calculated by the following equation

$$S_X = \left[\frac{1}{N-1} \sum_{i=1}^{n} \left(X_i - \overline{X} \right)^2 \right]^{1/2} \tag{B-4}$$

where X_i is the individual reading. $\overline{X}$ is the average value of the readings and calculated by

$$\overline{X} = \frac{1}{N} \sum_{K=1}^{N} X_i \tag{B-5}$$

With 95% confidence and 2 degrees of freedom (N-1=2), *t* is equal to 4.303. The bias was estimated by the system uncertainty of all the equipment used.

B.2 Uncertainty of the flow front for the underfill flow between two parallel plates

In the underfill flow between two parallel plates, the flow front is calculated with analytical Model I, i.e.

$$x_f = \left(\frac{\sigma \cos\theta}{m} \right)^{\frac{1}{n+1}} \left(\frac{(n+1)h}{2(2n+1)} t \right)^{\frac{n}{n+1}} \tag{B-6}$$

The bias caused by the system uncertainty is

$$B(x_f) = \left[\left(\frac{\partial x_f}{\partial \sigma} \delta\sigma \right)^2 + \left(\frac{\partial x_f}{\partial \theta} \delta\theta \right)^2 + \left(\frac{\partial x_f}{\partial h} \delta h \right)^2 \right]^{1/2} \tag{B-7}$$

or

$$\frac{B(x_f)}{x_f} = \frac{1}{x_f} \left[\left(\frac{\partial x_f}{\partial \sigma} \delta\sigma \right)^2 + \left(\frac{\partial x_f}{\partial \theta} \delta\theta \right)^2 + \left(\frac{\partial x_f}{\partial h} \delta h \right)^2 \right]^{1/2} \tag{B-8}$$

where

$$\frac{\partial x_f}{\partial \sigma} = \frac{1}{n+1}\sigma^{\frac{1}{n+1}-1}\left(\frac{\cos\theta}{m}\right)^{\frac{1}{n+1}}\left(\frac{(n+1)h}{2(2n+1)}t\right)^{\frac{n}{n+1}} \tag{B-9}$$

$$\frac{\partial x_f}{\partial \theta} = \frac{-\sin\theta}{n+1}(\cos\theta)^{\frac{1}{n+1}-1}\left(\frac{\sigma}{m}\right)^{\frac{1}{n+1}}\left(\frac{(n+1)h}{2(2n+1)}t\right)^{\frac{n}{n+1}} \tag{B-10}$$

$$\frac{\partial x_f}{\partial h} = \frac{n}{n+1}h^{\frac{n}{n+1}-1}\left(\frac{\sigma\cos\theta}{m}\right)^{\frac{1}{n+1}}\left(\frac{(n+1)}{2(2n+1)}t\right)^{\frac{n}{n+1}} \tag{B-11}$$

Dividing the equations (B-9) to (B-11) by x_f, respectively, leads to

$$\frac{1}{x_f}\frac{\partial x_f}{\partial \sigma} = \frac{1}{n+1}\frac{1}{\sigma} \tag{B-13}$$

$$\frac{1}{x_f}\frac{\partial x_f}{\partial \theta} = -\frac{\tan\theta}{n+1} \tag{B-14}$$

$$\frac{1}{x_f}\frac{\partial x_f}{\partial h} = \frac{n}{n+1}\frac{1}{h} \tag{B-15}$$

Substituting equation (B-13) to (B-15) in to equation (B-8) gives

$$\frac{B(x_f)}{x_f} = \left[\left(\frac{1}{n+1}\frac{\delta\sigma}{\sigma}\right)^2 + \left(\frac{-\tan\theta}{n+1}\delta\theta\right)^2 + \left(\frac{n}{n+1}\frac{\delta h}{h}\right)^2\right]^{1/2} \tag{B-16}$$

Substituting equation (B-16) into (B-1) gives

$$\frac{U(x_f)}{x_f} = t \cdot \left[\left(\frac{B(x_f)}{2x_f} \right)^2 + \left(\frac{S_{\bar{X}}}{x_f} \right)^2 \right]^{1/2} \tag{B-17}$$

where $U(x_f)/x_f$ is a relative uncertainty of flow front.

In the uncertainty estimation, the bias errors were chosen 5 present of the calculation values for the surface tension, contact angle and gap height. The calculated results were listed in the Table B.1 to Table B.3. From these calculations, the average relative uncertainty is 9.21%.

Table B.1 Bias error of the measurement system

$\delta\sigma$ (N/m)	$\delta\theta$ (degree)	δh (mm)	$\left(\frac{B_\sigma}{x_f}\right)^2$	$\left(\frac{B_\theta}{x_f}\right)^2$	$\left(\frac{B_h}{x_f}\right)^2$	$\left(\frac{B(x_f)}{x_f}\right)^2$
5.5E-4	1.425	4.25E-3	4.16E-4	3.03E-5	8.76E-4	1.32E-3

Table B.2 Precision errors of experimental data

Time (s)	x_1 (mm)	x_2 (mm)	x_3 (mm)	$(S_X)^2$	$(S_{\bar{X}})^2$	$(S_{\bar{X}}/x_f)^2$
10	3.5	3.6	3.6	2.3E-4	7.8E-5	6.16E-6
20	5.5	5.6	5.4	1.4E-2	4.5E-3	1.51E-4
30	7.1	7.1	7.0	1.9E-3	6.3E-4	1.27E-5
40	8.5	8.6	8.2	5.3E-2	1.8E-2	2.49E-4
50	9.5	9.8	9.3	7.3E-2	2.4E-2	2.68E-4
60.	10.5	10.8	10.3	5.0E-2	1.7E-2	1.49E-4

Table B.3 Relative uncertainty $U(x_f)/x_f$

Time (s)	$\left(\frac{B(x_f)}{x_f}\right)^2$	$\left(\frac{S_{\bar{X}}}{x_f}\right)^2$	$\left(\frac{U(x_f)}{x_f}\right)^2$
10	1.32E-3	6.16E-6	7.83
20	1.32E-3	1.51E-4	9.39
30	1.32E-3	1.27E-5	7.91
40	1.32E-3	2.49E-4	10.3
50	1.32E-3	2.68E-4	10.5
60	1.32E-3	1.49E-4	9.37
Average relative uncertainty: 9.21%			

B.3 Uncertainty of the flow front for the underfill flow in flip-chip packaging

In the underfill flow in flip-chip packaging, the flow front is calculated with Model II, i.e.

$$x_f = \frac{h}{2}\left(\frac{2\sigma\cos\theta(W^2+dW-dh)}{mhW(W+d)}\right)^{\frac{1}{n+1}}\left(\frac{n+1}{2n+1}t\right)^{\frac{n}{n+1}} \tag{B-18}$$

The bias caused by the system uncertainty is

$$B(x_f)=\left[\left(\frac{\partial x_f}{\partial\sigma}\delta\sigma\right)^2+\left(\frac{\partial x_f}{\partial\theta}\delta\theta\right)^2+\left(\frac{\partial x_f}{\partial h}\delta h\right)^2+\left(\frac{\partial x_f}{\partial d}\delta d\right)^2+\left(\frac{\partial x_f}{\partial W}\delta W\right)^2\right]^{1/2} \tag{B-19}$$

or

$$\frac{B(x_f)}{x_f} = \frac{1}{x_f}\left[\left(\frac{\partial x_f}{\partial \sigma}\delta\sigma\right)^2 + \left(\frac{\partial x_f}{\partial \theta}\delta\theta\right)^2 + \left(\frac{\partial x_f}{\partial h}\delta h\right)^2 + \left(\frac{\partial x_f}{\partial d}\delta d\right)^2 + \left(\frac{\partial x_f}{\partial W}\delta W\right)^2\right]^{1/2}$$

(B-20)

where

$$\frac{\partial x_f}{\partial \sigma} = \frac{h}{2}\frac{1}{n+1}\sigma^{\frac{1}{n+1}-1}\left(\frac{2\cos\theta(W^2+dW-dh)}{mh(W^2+dW)}\right)^{\frac{1}{n+1}}\left(\frac{n+1}{2n+1}t\right)^{\frac{n}{n+1}}$$

(B-21)

$$\frac{\partial x_f}{\partial \theta} = \frac{h}{2}\frac{1}{n+1}(\cos\theta)^{\frac{1}{n+1}-1}(-\sin\theta)\left(\frac{2\sigma(W^2+dW-dh)}{mh(W^2+dW)}\right)^{\frac{1}{n+1}}\left(\frac{n+1}{2n+1}t\right)^{\frac{n}{n+1}}$$

(B-22)

$$\frac{\partial x_f}{\partial h} = \frac{1}{2}\left(\frac{2\sigma\cos\theta(W^2+dW-dh)}{mh(W^2+dW)}\right)^{\frac{1}{n+1}}\left(\frac{n+1}{2n+1}t\right)^{\frac{n}{n+1}} +$$
$$\frac{h}{2}\left(\frac{n+1}{2n+1}t\right)^{\frac{n}{n+1}}\frac{1}{n+1}\left(\frac{2\sigma\cos\theta(W^2+dW-dh)}{mh(W^2+dW)}\right)^{\frac{1}{n+1}-1}\times$$
$$\left[\frac{2\sigma\cos\theta(-d)mh(W^2+dW)-2\sigma\cos\theta(W^2+dW-dh)m(W^2+dW)}{m^2h^2(W^2+dW)^2}\right]$$

(B-23)

$$\frac{\partial x_f}{\partial d} = \frac{h}{2}\left(\frac{n+1}{2n+1}t\right)^{\frac{n}{n+1}}\frac{1}{n+1}\left(\frac{2\sigma\cos\theta(W^2+dW-dh)}{mh(W^2+dW)}\right)^{\frac{1}{n+1}-1}\times$$
$$\left[\frac{2\sigma\cos\theta(W-h)mh(W^2+dW)-2\sigma\cos\theta(W^2+dW-dh)mhW}{m^2h^2(W^2+dW)^2}\right]$$

(B-24)

$$\frac{\partial x_f}{\partial W} = \frac{h}{2}\left(\frac{n+1}{2n+1}t\right)^{\frac{n}{n+1}} \frac{1}{n+1}\left(\frac{2\sigma\cos\theta(W^2+dW-dh)}{mh(W^2+dW)}\right)^{\frac{1}{n+1}-1} \times \left[\frac{2\sigma\cos\theta(2W+d)mh(W^2+dW)-2\sigma\cos\theta(W^2+dW-dh)mh(2W+d)}{m^2h^2(W^2+dW)^2}\right] \tag{B-25}$$

Dividing the equations (B-21) to (B-25) by x_f, respectively, leads to

$$\frac{1}{x_f}\frac{\partial x_f}{\partial \sigma} = \frac{1}{n+1}\frac{1}{\sigma} \tag{B-26}$$

$$\frac{1}{x_f}\frac{\partial x_f}{\partial \theta} = \frac{1}{n+1}\frac{-\sin\theta}{\cos\theta} = -\frac{\tan\theta}{n+1} \tag{B-27}$$

$$\frac{1}{x_f}\frac{\partial x_f}{\partial h} = \frac{1}{h} - \frac{1}{n+1}\left(\frac{W^2+dW}{h(W^2+dW-dh)}\right) \tag{B-28}$$

$$\frac{1}{x_f}\frac{\partial x_f}{\partial d} = \frac{1}{n+1}\left(\frac{W-h}{W^2+dW-dh} - \frac{1}{W+d}\right) = \frac{-hW}{(n+1)(W^2+dW-dh)(W+d)} \tag{B-29}$$

$$\frac{1}{x_f}\frac{\partial x_f}{\partial W} = \frac{2W+d}{n+1}\left(\frac{1}{W^2+dW-dh} - \frac{1}{W(W+d)}\right) = \frac{dh(2W+d)}{(n+1)(W^2+dW-dh)(W^2+dW)} \tag{B-30}$$

Substituting equation (B-26) to (B-30) in to equation (B-8) gives

$$\frac{B(x_f)}{x_f}=\left[\begin{array}{l}\left(\frac{1}{n+1}\frac{\delta\sigma}{\sigma}\right)^2+\left(\frac{-\tan\theta}{n+1}\delta\theta\right)^2+\left(\frac{\delta h}{h}-\frac{(W^2+dW)\delta h}{h(n+1)(W^2+dW-dh)}\right)^2+\\ \left(\frac{-hW\delta d}{(n+1)(W^2+dW-dh)(W+d)}\right)^2+\left(\frac{dh(2W+d)\delta W}{(n+1)(W^2+dW-dh)(W^2+dW)}\right)^2\end{array}\right]^{1/2} \tag{B-31}$$

Dividing equations (B-1) by the flow front x_f gives

$$\frac{U(x_f)}{x_f}=t\cdot\left[\left(\frac{B(x_f)}{2x_f}\right)^2+\left(\frac{S_{\bar{X}}}{x_f}\right)^2\right]^{1/2} \tag{B-32}$$

In the uncertainty estimation, the bias errors were chosen 5 present of the calculation values for the surface tension, contact angle, gap height, solder diameter, and clearance between two solder bumps. The calculated results were listed in the Table B.4 to Table B.6. From these calculations, the average relative uncertainty is 12.1%.

Table B.4 Bias error of the measurement system

$\delta\sigma$ (N/m)	$\delta\theta$ (degree)	δh (mm)	δd (mm)	δW (mm)	
5.5E-4	1.425	2.5E-3	0.005	0.0075	
$\left(\frac{B_\sigma}{x_f}\right)^2$	$\left(\frac{B_\theta}{x_f}\right)^2$	$\left(\frac{B_h}{x_f}\right)^2$	$\left(\frac{B_d}{x_f}\right)^2$	$\left(\frac{B_W}{x_f}\right)^2$	$\left(\frac{B(x_f)}{x_f}\right)^2$
4.16E-4	3.03E-5	7.0E-4	3.54E-6	2.52E-5	0.001175

Table B.5 Precision errors of experimental data

Time (s)	x_1 (mm)	x_2 (mm)	x_3 (mm)	$(S_X)^2$	$(S_{\bar{X}})^2$	$(S_{\bar{X}}/x_f)^2$
5	1.6	1.6	1.4	0.0133	0.0044	0.00189
10	2.6	2.5	2.5	0.0033	0.0011	0.000173
15	3.3	3.3	3.5	0.0133	0.0044	0.000392
20	3.9	4.0	4.2	0.0233	0.0078	0.000478
25	4.4	4.4	4.6	0.0133	0.0044	0.000223
30	5.0	5.0	5.2	0.0133	0.0044	0.000173
35	5.3	5.3	5.7	0.0533	0.0178	0.000602

Table B.6 Relative uncertainty

Time (s)	$\left(\frac{B(x_f)}{x_f}\right)^2$	$\left(\frac{S_{\bar{X}}}{x_f}\right)^2$	$\left(\frac{U(x_f)}{x_f}\right)^2$
5	0.001175	0.00189	20.1
10	0.001175	0.000173	9.3
15	0.001175	0.000392	11.3
20	0.001175	0.000478	12.0
25	0.001175	0.000223	9.8
30	0.001175	0.000173	9.3
35	0.001175	0.000602	12.9
Average relative uncertainty: 12.1%			

B.4 Uncertainty of the flow front for the underfill flow between two parallel plates (Washburn model)

The flow front of Washburn model is given by the following equation

$$x_f = \left(\frac{h\sigma \cos\theta}{3\mu} t \right)^{\frac{1}{2}} \tag{B-33}$$

The bias caused by the system uncertainty is

$$\frac{B(x_f)}{x_f} = \frac{1}{x_f} \left[\left(\frac{\partial x_f}{\partial \sigma} \delta\sigma \right)^2 + \left(\frac{\partial x_f}{\partial \theta} \delta\theta \right)^2 + \left(\frac{\partial x_f}{\partial h} \delta h \right)^2 \right]^{1/2} \tag{B-34}$$

Taking n = 1 from equations (B-13) to (B-15) leads to

$$\frac{1}{x_f} \frac{\partial x_f}{\partial \sigma} = \frac{1}{2\sigma} \tag{B-35}$$

$$\frac{1}{x_f} \frac{\partial x_f}{\partial \theta} = -\frac{\tan\theta}{2} \tag{B-36}$$

$$\frac{1}{x_f} \frac{\partial x_f}{\partial h} = \frac{1}{2h} \tag{B-37}$$

Substituting equation (B-35) to (B-37) in to equation (B-34) gives

$$\frac{B(x_f)}{x_f} = \left[\left(\frac{1}{n+1} \frac{\delta\sigma}{\sigma} \right)^2 + \left(\frac{-\tan\theta}{n+1} \delta\theta \right)^2 + \left(\frac{n}{n+1} \frac{\delta h}{h} \right)^2 \right]^{1/2} \tag{B-38}$$

Substituting equation (B-38) into (B-1) leads to

$$\frac{U(x_f)}{x_f} = t \cdot \left[\left(\frac{B(x_f)}{2x_f} \right)^2 + \left(\frac{S_X}{x_f} \right)^2 \right]^{1/2} \tag{B-17}$$

where $U(x_f)/x_f$ is a relative uncertainty.

Following the same procedures as described in Section B.1, the relative uncertainty $U(x_f)/x_f$ can be estimated. The results are listed in Table B.7.

Table B.7 Relative uncertainty $U(x_f)/x_f$

$\left(B(x_f/x_f\right)^2$	$\left(S_X/x_f\right)^2$	$\left(U(x_f)/x_f\right)^2$
0.00125	0.00042	11.6 %

APPENDIX C: ESTIMATION OF RELATIVE ERROR

From equation (3-21)

$$x_f^2 = \frac{2\Delta p b^2}{3\mu} t - \frac{4\Delta p b^2}{\mu} \sum_{n=0}^{\infty} \frac{1}{(\lambda_n b)^4 \lambda_n^2 \nu} \tag{C-1}$$

Substituting $\lambda_n b = \frac{(2n+1)\pi}{2}$ into equation (C-1) gives

$$x_f^2 = \frac{2\Delta p b^2}{3\mu} t - \frac{4\Delta p b^2}{\mu} \sum_{n=0}^{\infty} \frac{1}{\left((2n+1)\frac{\pi}{2}\right)^4 \left((2n+1)\frac{\pi}{2b}\right)^2 \nu} \tag{C-2}$$

Rearranging equation (C-3) leads to

$$x_f^2 = \frac{2\Delta p b^2}{3\mu} t - \frac{4\Delta p b^4}{\mu \nu \pi^6} \sum_{n=0}^{\infty} \frac{1}{\left(n+\frac{1}{2}\right)^6}$$

Or

$$x_f^2 = \frac{2\Delta p b^2}{3\mu} t - \frac{4\Delta p b^4}{\mu \nu \pi^6} \left[64 + \sum_{n=1}^{\infty} \frac{1}{\left(n+\frac{1}{2}\right)^6} \right] \tag{C-3}$$

Since a *p*-series $\sum_{n=1}^{\infty} \frac{1}{n^p}$ is convergent if $p > 1$ and note that the series in equation (C-3) is less than the *p*-series with $p = 6$, i.e.,

$$\sum_{n=1}^{\infty}\frac{1}{\left(n+\frac{1}{2}\right)^6}<\sum_{\mathrm{n}=1}^{\infty}\frac{1}{n^6} \tag{C-4}$$

Therefore the series $\sum_{n=1}^{\infty}\frac{1}{(n+1/2)^6}$ is convergent. Its sum can be estimated from the *p*-series $\sum_{n=1}^{\infty}\frac{1}{n^6}$ by writing as following form

$$\begin{aligned}\sum_{n=1}^{\infty}\frac{1}{n^6}=1+\left(\frac{1}{2^6}+\frac{1}{3^6}\right)+\left(\frac{1}{4^6}+\cdots+\frac{1}{7^6}\right)+\left(\frac{1}{8^6}+\cdots+\frac{1}{15^6}\right)+\cdots\\ +\left(\frac{1}{16^6}+\cdots+\frac{1}{31^6}\right)+\cdots\end{aligned} \tag{C-5}$$

And each term in the series is less than that in the following series

$$\begin{aligned}\sum_{n=1}^{\infty}\left(\frac{1}{2^5}\right)^{n-1}&=1+\left(\frac{1}{2^6}+\frac{1}{2^6}\right)+\left(\frac{1}{4^6}+\cdots+\frac{1}{4^6}\right)+\left(\frac{1}{8^6}+\cdots+\frac{1}{8^6}\right)+\cdots\\ &\quad+\left(\frac{1}{16^6}+\cdots+\frac{1}{16^6}\right)+\cdots\\ &=1+\frac{1}{2^5}+\left(\frac{1}{2^5}\right)^2+\left(\frac{1}{2^5}\right)^3+\left(\frac{1}{2^5}\right)^4+\cdots\end{aligned} \tag{C-6}$$

Since series (C-6) is a geometric series with the common ratio $r=\frac{1}{2^5}<1$, it is convergent and the sum of the geometric series is given by

$$\sum_{n=1}^{\infty}\left(\frac{1}{2^5}\right)^{n-1}=\frac{1}{1-r}=\frac{1}{1-1/32}=\frac{32}{31}$$

Therefore the sum of the series in equation (C-3) is

$$\sum_{n=1}^{\infty}\frac{1}{\left(n+\frac{1}{2}\right)^6}<\frac{32}{31}$$

The second term in equation (C-1) becomes

$$\frac{4\Delta pb^4}{\mu v\pi^6}\left[64+\sum_{n=1}^{\infty}\frac{1}{\left(n+\frac{1}{2}\right)^6}\right]\approx\frac{4\Delta pb^4}{\mu v\pi^6}\left(64+\frac{32}{31}\right) \tag{C-7}$$

Note that when taking one term of the series of equation (C-1) it gives the second term of equation (C-1) as $\frac{4\Delta pb^4}{\mu v\pi^6}64$, the relative error caused by this is

$$R<\frac{\frac{4\Delta pb^4}{\mu v\pi^6}\left(64+\frac{32}{31}\right)-\frac{4\Delta pb^4}{\mu v\pi^6}64}{\frac{4\Delta pb^4}{\mu v\pi^6}\left(64+\frac{32}{31}\right)}=0.016=1.6\%$$

APPENDIX D: ANSYS CODE FOR UNDERFILL FLOW SIMULATION IN FLIP-CHIP PACKAGING

```
!/title,underfill flow in flip chip package
/prep7
et,1,fluid141

LX = 6.7/1000              ! X length
LY = 6.7/1000              ! Y length
DX=0.262/1000
DX1=0.094/1000
DX2=0.168/1000
DAGE=(LX-DX*25-DX1)/2
DAGE2=DAGE+0.00/1000

!  Meshing
*DIM,XC,,52
*DIM,YC,,52
SUM=0
*do,I,1,51,2
XC(I)=SUM*DX+DAGE2
YC(I)=SUM*DX+DAGE2
SUM=SUM+1
*enddo

*do,I,2,52,2
XC(I)=XC(I-1)+DX1
YC(I)=YC(I-1)+DX1
*enddo
```

```
! CHANGE BOUNDARY COODINATES
XC(1)=0
YC(1)=0
XC(52)=XC(52)+DAGE2
YC(52)=YC(52)+DAGE2

*DIM,AK,,52,52
SUM=0
*do,J,1,52
*do,I,1,52
SUM=SUM+1
AK(I,J)=SUM
K,SUM,XC(I),YC(J)
*enddo
*enddo

*do,J,1,51,2
A,AK(1,J),AK(52,J),AK(52,J+1),AK(1,J+1)
*enddo

*do,I,1,51,2
A,AK(I,1),AK(I+1,1),AK(I+1,52),AK(I,52)
*enddo

ASEL,S,AREA,,1,52
AADD,ALL
AESIZE,53,DX1/2
AMESH,ALL

p1=101325
p2=0
```

```
LSEL,S,,,121,189,4   ! Wall boundary conditions
LSEL,A,,,213,229
NSLL,,1
D,ALL,VY,%vbc01%

LSEL,S,,,105,117,4   ! Wall boundary conditions
LSEL,A,,,209,212
LSEL,A,,,193,205,4
LSEL,A,,,230,233
NSLL,,1
D,ALL,VX,0.0
D,ALL,VY,0.0

NSEL,S,LOC,X,0.0     ! Wall boundary conditions
NSEL,A,LOC,X,XC(52)
D,ALL,VX,0
D,ALL,VY,0

NSEL,S,LOC,Y,YC(52)     ! Wall boundary conditions
D,ALL,VX,0
D,ALL,VY,0

LSEL,S,,,309,2808   ! Wall boundary conditions
NSLL,,1
D,ALL,VX,0.0
D,ALL,VY,0.0

NSEL,ALL,NODE
IC,ALL,VX,0
IC,ALL,VY,0
```

```
LSEL,S,,,121,189,4
LSEL,A,,,213,229
SFL,ALL,VFRC,1,,1
FINISH

/PREP7
FLDATA1,SOLU,TRAN,1
FLDATA1,SOLU,FLOW,1
FLDATA1,SOLU,TEMP,0
FLDATA1,SOLU,TURB,0
FLDATA1,SOLU,COMP,0
FLDATA1,SOLU,VOF,1
FLDATA1,SOLU,SFTS,0
FLDATA1,SOLU,IVSH,0
FLDATA1,SOLU,SWRL,0
FLDATA1,SOLU,SPEC,0
FLDATA1,SOLU,ALE,0
!*
/COM,,Transient Analysis,1
*SET,_z4,-1
*SET,_z14,1
!*
FLDATA4,TIME,STEP,-1
FLDATA4,TIME,ISTEP,0.01,
FLDATA4,TIME,NUMB,5000,

FLDATA4,TIME,TEND,1.0e06
FLDATA4,TIME,GLOB,10,
FLDATA4,TIME,VX,1e-6,
FLDATA4,TIME,VY,1e-6,
```

```
FLDATA4,TIME,VZ,0,
FLDATA4,TIME,PRES,1e-006,
FLDATA4,TIME,TEMP,1e-006,
FLDATA4,TIME,ENKE,0.01,
FLDATA4,TIME,ENDS,0.01,
FLDATA4A,STEP,OVER,0,
FLDATA4,TIME,OVER,0
FLDATA4A,STEP,APPE,0,
FLDATA4,TIME,APPE,1

FLDATA4A,STEP,SUMF,10,
FLDATA4,TIME,SUMF,1.0e6
FLDATA4,TIME,BC,0
FLDATA4,TIME,TEND,19.6,
!*
FLDATA12,PROP,DENS,0
FLDATA13,VARY,DENS,0
FLDATA12,PROP,VISC,21
FLDATA13,VARY,VISC,1
FLDATA12,PROP,COND,0
FLDATA13,VARY,COND,0
FLDATA12,PROP,SPHT,0
FLDATA13,VARY,SPHT,0
!*
FLDATA7,PROT,DENS,CONSTANT
FLDATA8,NOMI,DENS,1600,
FLDATA9,COF1,DENS,0
FLDATA10,COF2,DENS,0
FLDATA11,COF3,DENS,0

!! material A
```

FLDATA7,PROT,VISC,POWL
FLDATA8,NOMI,VISC,1.03
FLDATA9,COF1,VISC,1e-6,
FLDATA10,COF2,VISC,1,
FLDATA11,COF3,VISC,1.09,
FLDATA12,PROP,IVIS,0.7,

FLDATA7,PROT,COND,CONSTANT
FLDATA8,NOMI,COND,-1,
FLDATA9,COF1,COND,0
FLDATA10,COF2,COND,0
FLDATA11,COF3,COND,0

FLDATA7,PROT,SPHT,CONSTANT
FLDATA8,NOMI,SPHT,-1,
FLDATA9,COF1,SPHT,0
FLDATA10,COF2,SPHT,0
FLDATA11,COF3,SPHT,0
!*
FLDATA36,AMBV,VX,0,
FLDATA36,AMBV,VY,0,
FLDATA36,AMBV,VZ,0,
FLDATA36,AMBV,PRES,p2,

FLDATA36,AMBV,ENKE,1.0000000133514e-010,
FLDATA36,AMBV,ENDS,1.0000000133514e-010,
FLDATA36,AMBV,TEMP,293,
!*
FLDATA4,TIME,NTVF,1,
FLDATA25,RELX,VX,0.5,
FLDATA25,RELX,VY,0.5,

```
FLDATA25,RELX,VZ,0.5,
FLDATA25,RELX,PRES,0.5,
FLDATA25,RELX,TEMP,0.8,
FLDATA25,RELX,ENKE,0.5,
FLDATA25,RELX,ENDS,0.5,
!*
FLDATA25,RELX,DENS,0.5,
FLDATA25,RELX,SPHT,1,
FLDATA25,RELX,VISC,0.5,
FLDATA25,RELX,COND,0.5,
FLDATA25,RELX,EVIS,0.5,
FLDATA25,RELX,ECON,0.5,
!*
SAVE
FINISH
/SOLU
SOLVE

FINISH
/POST1
SET,LAST
/EFACE,1
!*
PLNSOL,PRES, ,0,
PLVFRC,0
!*
PLESOL,VFRC,NMISC,1,1
FINISH
```